DEVELOPMENT OF HIGH PERFORMANCE ACTIVE MATERIALS FOR MICROBOLOMETERS

A THESIS SUBMITTED TO
THE GRADUATE SCHOOL OF NATURAL AND APPLIED SCIENCES
OF
MIDDLE EAST TECHNICAL UNIVERSITY

BY

NUMAN EROĞLU

IN PARTIAL FULFILLMENT OF THE REQUIREMENTS
FOR
THE DEGREE OF MASTER OF SCIENCE
IN
MICRO AND NANOTECHNOLOGY DEPARTMENT

AUGUST 2011

Approval of the thesis:

DEVELOPMENT OF HIGH PERFORMANCE ACTIVE MATERIALS FOR MICROBOLOMETERS

submitted by **NUMAN EROĞLU** in partial fulfillment of the requirements for the degree of **Master of Science in Micro and Nanotechnology Department, Middle East Technical University** by,

Prof. Dr. Canan ÖZGEN _________
Dean, Graduate School of **Natural and Applied Sciences**

Prof. Dr. Mürvet VOLKAN _________
Head of Department, **Micro and Nanotechnology**

Prof. Dr. Tayfun AKIN _________
Supervisor, **Electrical and Electronics Eng. Dept., METU**

Prof. Dr. Raşit TURAN _________
Co-Supervisor, **Physics Department, METU**

Examining Committee Members

Doç. Dr. Haluk KÜLAH _________
Electrical and Electronics Eng. Dept., METU

Prof. Dr. Tayfun AKIN _________
Electrical and Electronics Eng. Dept., METU

Prof. Dr. Raşit TURAN _________
Physics Department, METU

Doç. Dr. Ramis Mustafa ÖKSÜZOĞLU _________
Materials Science and Engineering, Anadolu University

Dr. Selçuk ÖZER _________
ASELSAN

Date: 22.08.2011

I hereby declare that all information in this document has been obtained and presented in accordance with academic rules and ethical conduct. I also declare that, as required by these rules and conduct, I have fully cited and referenced all material and results that are not original to this work.

Name, Last name : Numan EROĞLU

Signature :

ABSTRACT

DEVELOPMENT OF HIGH PERFORMANCE ACTIVE MATERIALS FOR MICROBOLOMETERS

EROĞLU, Numan

M.Sc., Department of Micro and Nanotechnology

Supervisor : Prof. Dr. Tayfun AKIN

Co-Supervisor: Prof. Dr. Raşit TURAN

August 2011, 112 Pages

This thesis reports the development of Vanadium Tungsten Oxide (VWO) film as an active detector material for uncooled infrared detectors by using the reactive DC magnetron co-sputtering method. VWO is a doped form of the Vanadium Oxide (VO_x) which is known as a prominent material for uncooled infrared detectors with its high TCR, low resistivity, and low noise properties.

VO_x is a widely preferred material for commercialized uncooled infrared detectors along with its drawbacks. Fabrication is fairly difficult due to its unstable material properties and the need for low process temperatures for a monolithic, CMOS compatible surface micromachining process. Hence, a new material with high performance and easier fabrication is needed. This thesis is the first study at METU on

the development of high-performance VWO as an active detector material for uncooled infrared detectors.

Deposition studies of VWO primarily started by measuring the effects of deposition parameters upon the magnetron sputtering system. Because the high effectiveness of the tungsten doping has been obtained for the doping level below 10% according to literary information, maximum vanadium (V) deposition rate together with minimum tungsten (W) deposition rate has been initially aimed.

TCR of the VWO films has been measured between -2.48 %/K and -3.31 %/K, and the variation of noise corner frequency from 0.6 kHz to 8 kHz has been observed. In addition to these results of VWO, a favorable VO_x recipe which has the highest performance done at METU in terms of resistance, TCR, noise and uniformity has also attained during the studies. Structural characterization of VWO is achieved using XPS, XRD, and AFM characterization techniques.

Other than the sputtering parameters, post-annealing process and oxygen plasma exposure was examined as well. A general observation of the post-annealing is that it decreases not merely the TCR but also the noise of the deposited film. A short-period oxygen plasma exposure has a constructive effect on the noise behavior.

Fabricated vanadium tungsten oxide with sandwich type resistor structure shows very close but better bolometric properties when compared with the yttrium barium copper oxide (YBCO), which is another material being studied in scope of other theses at METU.

XPS, XRD and AFM characterization methods have been used for the structural characterization of vanadium-tungsten-oxide.

Keywords: Microbolometer, Vanadium Tungsten Oxide (VWO), Vanadium Oxide (VO_x), Planar Type Resistors, Sandwich Type Resistors, Temperature Coefficient of Resistance (TCR), X-Ray Diffraction (XRD), X-Ray Photoelectron Spectroscopy (XPS), Atomic Force Microscope (AFM).

ÖZ

MİKROBOLOMETRELER İÇİN YÜKSEK BAŞARIMLI

AKTİF MALZEMELERİN GELİŞTİRİLMESİ

EROĞLU, Numan

Yüksek Lisans, Mikro ve Nanoteknoloji Bölümü

Tez Yöneticisi : Prof. Dr. Tayfun AKIN

Ortak Tez Yöneticisi : Prof. Dr. Raşit TURAN

Ağustos 2011, 112 Sayfa

Bu tez çalışmasında, doğru akımlı reaktif magnetron birlikte sıçratma yöntemi kullanılarak, soğutmasız kızılötesi algılayıcılar için aktif algılayıcı malzeme vanadyum-tungsten-oksidin üretimi anlatılmıştır. Vanadyum-tungsten-oksit, soğutmasız kızılötesi algılayıcı uygulamaları için yüksek direnç sıcaklık sabiti, düşük gürültü özellikleri ve düşük özdirenç değeri ile öne çıkmış vanadyum-oksit malzemesinin katkılanmış şeklidir.

Vanadyum-oksit bazı eksiklikleri ile beraber ürüne dönüştürülmüş soğutmasız kızılötesi algılayıcılar için büyük çapta tercih edilen bir malzemedir. Vanadyum-oksit üretimi, değişken malzeme özellikleri ve tek parçalı ve CMOS uyumlu yüzey mikro işleme için gerekli olan düşük sıcaklık ihtiyacı nedeniyle oldukça zordur. Bu nedenle, yüksek başarımlı

daha kolay üretilebilecek yeni bir malzemeye ihtiyaç duyulmaktadır. Bu tez çalışması, soğutmasız kızılötesi algılayıcılar için aktif malzeme olarak yüksek başarımlı vanadyum-tungsten-oksidin geliştirilmesine yönelik ODTÜ'de yapılan ilk çalışmadır.

Vanadyum-tungsten-oksit kaplama çalışmaları öncelikle magnetron sıçratma sisteminin kaplama değişkenlerinin etkilerinin ölçülmesi ile başlamıştır. Kaynaklardaki bilgilere göre tungsten katkılamanın en büyük etkisi % 10 seviyesinin altında gerçekleştiğinden, başlangıçta vanadyum için en yüksek, tungsten için en düşük kaplama oranı hedeflenmiştir.

Direnç sıcaklık sabiti -2.48 %/K ve -3.31 %/K arasında ölçülmüş ve gürültü köşe frekansının 0.6 kHz den 8 kHz e kadar değiştiği gözlenmiştir. Vanadyum-tungsten-oksit ile alınan bu sonuçlara ilave olarak, çalışmalar sürecinde direnç, sıcaklık direnç sabiti, gürültü seviyesi ve direnç değişmezliği ile ODTÜ'de yapılan en iyi vanadyum-oksit kaplama reçetesine ulaşılmıştır. Vanadyum-tungsten-oksit malzemesinin yapısal tanısı XPS, XRD ve AFM teknikleri kullanılarak yapılmıştır.

Sıçratma işlemi değişkenlerine ilave olarak, tavlama ve oksijen plazman uygulaması da incelenmiştir. Genel bir gözlem olarak tavlama işlemi, kaplanmış olan malzemenin özdirencini düşürürken, sıcaklık direnç sabitini ve gürültü davranışını da düşürmektedir. Kısa süreli oksijen plazma uygulaması kaplanan malzemenin gürültü davranışı açısından olumlu bir etki göstermektedir.

Sandviç tipi direnç yapısı ile üretilen vanadyum-tungsten-oksit, ODTÜ'de diğer tezler kapsamında kullanılan itriyum-baryum-bakır-okside çok yakın fakat daha iyi bolometrik özellikler göstermiştir.

Anahtar Kelimeler: Mikrobolometre, Vanadyum Tungsten Oksit (VWO), Vanadyum Oksit (VO_x), Düzlemsel Tip Elektrot, Sandviç Tip Elektrot, Direnç Sıcaklık Sabiti (TCR), X-Işını Kırınımı (XRD), X-Işını Difraksiyon Spektroskopisi (XPS), Atomik Kuvvet Mikroskopu (AFM).

To my wife, Zeynep

ACKNOWLEDGEMENTS

First and foremost, I owe my deepest gratitude to my advisor Prof. Dr. Tayfun AKIN for his continuous support of my M.Sc. study and research, for his ceaseless guidance, enthusiasm and his broad knowledge. It was a great chance for me to meet and work with him.

I also would like to express my sincere appreciation to my co-supervisor Prof. Dr. Raşit TURAN. In addition to his gentle manner and encouraging advice, his lectures guided me a lot throughout this thesis study.

I would like to extend my thanks to Dr. M.Yusuf TANRIKULU for sharing his immense knowledge, valuable comments and endless support. I also would like to thank to Dr. Murat TEPEGÖZ for his priceless advice which broaden my viewpoint. My heartfelt thanks goes to Orhan AKAR, the boss, who helped me sort out my problems with his great experience.

My special thanks also goes to Ufuk ŞENVELI and Eren ÇANGA. Their guidance, contributions, and self-sacrifice always encouraged me during all aspects of deposition studies. A big thank you to Akın AYDEMİR for his patience and help with my etching process and SEM works.

I am indebted to Burak EMİNOĞLU for his great fellowship. The noise measurements would not have been possible without his great efforts.

Osman AYDIN and Selçuk KESKİN deserve a special mention for their vigorous and resolute support let alone their close rapport. Additionally, they were always present to hearten me in hard times, relieve my stress and provide help in cleanroom when necessary.

I greatly appreciate and wish to thank Özgecan DERVİŞOĞLU for her excellent assistance during this thesis study.

I am very appreciative of Şeniz Esra KÜÇÜK and Alperen TOPRAK of their contribution to the early stages of TCR and noise measurements.

I would also like to kindly thank the members of VLSI design laboratory and METU MEMS research group for their never-ending support and friendship. I am thankful to the staff of METU MEMS Research and Applications Center for creating the best working atmosphere and their friendship.

I acknowledge and express my gratitude to Turkish Naval Forces for giving me such an opportunity in METU.

I wish to thank my family for always being there for me no matter what.

Last but by no means least, I also would like to give my special thanks to my wife, Zeynep EROĞLU. In no way could this thesis have been written without her devotion, encouragement, understanding, and assistance.

TABLE OF CONTENTS

ABSTRACT iv

ÖZ vi

ACKNOWLEDGEMENTS ix

TABLE OF CONTENTS xi

LIST OF TABLES xiv

LIST OF FIGURES xvi

CHAPTERS

1. INTRODUCTION 1

   1.1 Infrared Radiation 3

   1.2 Infrared Detection 5

   1.3 Infrared Detectors 7

   1.4 Microbolometers 9

      1.4.1 Diode Type Microbolometers 11

      1.4.2 Resistive Type Microbolometers 12

   1.5 Noise in Resistive Bolometers 13

   1.6 Important Figures of Merit for Bolometers 15

      1.6.1 Responsivity (R) 15

      1.6.2 Noise Equivalent Power (NEP) 16

      1.6.3 Noise Equivalent Temperature Difference (NETD) 16

   1.7 Objectives and Organization 17

2. ACTIVE DETECTOR MATERIALS AND FABRICATION DETAILS 19
2.1 Determination of Active Material 19
2.1.1 Comparison of Active Materials 22
2.2 Vanadium Tungsten Oxide (VWO) as an Active Material 25
2.3 Sputtering and the Deposition System 29
2.4 Resistive Structures 33
2.4.1 Planar Type Resistors 34
2.4.2 Sandwich Type Resistors 36
2.4.3 Enhanced Sandwich Type Resistors 38
2.5 Optimization of Fabrication Steps 41
3. DEPOSITION AND CHARACTERIZATION 45
3.1 Preliminary Works 45
3.1.1 Optimization of Thickness Uniformity 46
3.1.2 Determination of Process Conditions 47
3.1.3 Determination of the Mask Set 51
3.2 Bolometric Characterization 52
3.2.1 Resistivity Measurements 53
3.2.2 TCR Measurements 55
3.2.3 Noise Measurements 57
4. EXPERIMENTAL RESULTS AND STRUCTURAL CHARACTERIZATION .. 61
4.1 Analysis of Bolometric Properties in Different Deposition Conditions 61
4.1.1 Influence of Vanadium Power 62
4.1.2 Influence of Tungsten Power 65
4.1.3 Influence of Oxygen Flow 68
4.1.4 Influence of Argon Flow 71

4.1.5 Influence of Working Pressure....74
4.1.6 Influence of Hot Deposition Condition....77
4.1.7 Influence of Post-Annealing....80
4.1.8 Influence of Oxygen Plasma....83
4.2 Studies on Optimized VWO Recipe....85
4.3 Structural Characterization....87
4.3.1 AFM Results....87
4.3.2. XRD Results....89
4.3.3 XPS Results....91
5. CONCLUSION AND FUTURE WORKS....95
REFERENCES....99
APPENDIX....104

LIST OF TABLES

TABLES

Table 2.1: General TCR values of the common materials for bolometric applications [18, 19]. 20

Table 2.2: Foundations and their active materials [14, 16, 18, 21-27]. 23

Table 2.3: Comparison of flicker noise values with different materials in literature [13, 24]....... 24

Table 2.4: Limitations of the sputtering system used for VWO deposition. 32

Table 2.5: Deposition condition of the sample used for etching trials. . 43

Table 3.1: Thickness uniformity measurements of the vanadium and tungsten samples. 47

Table 3.2: Limitation of the actual V power as a result of the plasma current limitation....... 50

Table 3.3: Determined recipe which is taken as a reference for further studies....... 51

Table 3.4: Resistivity measurements of the reference recipe given in Table 3.3....... 55

Table 3.5: Summary of the measurements for the reference recipe given in Table 3.3. The NETD is calculated for the reference and the following recipes in Chapter 4 by using constant parameters given in Table 3.7....... 60

Table 4.1: Recipes of the samples used to investigate the influence of vanadium power on bolometric properties. 63

Table 4 2: Summary of the measurements at different vanadium power levels....... 65

Table 4.3: Recipes of the samples used to investigate the influence of tungsten power on bolometric properties. 66

Table 4.4: Summary of the measurements for the samples deposited at different tungsten power....... 68

Table 4.5: Recipes of the samples used to investigate the influence of oxygen flow on bolometric properties 69

Table 4.6: Summary of the measurements for the samples deposited at different oxygen flow rates. 71

Table 4.7: Recipes of the samples used to investigate the influence of argon flow on bolometric properties 72

Table 4.8: Summary of the measurements for the samples deposited at different argon flow rates. 74

Table 4.9: Recipes of the samples used to investigate the influence working pressure on bolometric properties. 75

Table 4.10: Summary of the measurements for the samples deposited at different working pressures. 77

Table 4.11: Recipes of the samples used to investigate the influence of deposition at different substrate temperatures on bolometric properties. 78

Table 4.12: Summary of the measurements for the samples deposited at different substrate temperatures. 80

Table 4.13: Summary of the measurements for the samples annealed at 300 °C for different time periods. 82

Table 4.14: Summary of the measurements for the samples exposed to oxygen plasma for different time periods. 84

Table 4.15: Optimized VWO recipe of this thesis study and its bolometric properties. 85

Table 4.16: Comparison between bolometric properties of optimized recipe before and after PECVD conditions. 86

Table 4.17: Comparison of YBCO and VWO shows almost identical results. 86

Table 4.18: Summary of the AFM characterization 87

Table 4.19: Atomic ratios of the studied samples. 92

LIST OF FIGURES

FIGURES

Figure 1.1: The spectral exitance of a typical blackbody. The yellow line shows the regime of the sun surface and the red is the regime of room temperature [3]. 2

Figure 1.2: The electromagnetic spectrum including the visible and the infrared sub-regions [4]........ 4

Figure 1.3: Transmittance of the atmosphere with respect to wavelength. The dominant absorbing molecules are indicated in the below box [5]. 5

Figure 1.4: The spectral exitance of various kinds of blackbodies at different temperatures. The straight line shows the peak points of the exitance according to Wien's Displacement Law [6]. 6

Figure 1.5: The principle structure of a thermal infrared detector [9].. 8

Figure 1.6: The Wheatstone bridge, Rx/R3=R1/R2 for V_g is balanced [10]. 10

Figure 1.7: A representative perspective view of a microbolometer detector pixel [6]........10

Figure 1.8: SEM images of some state of art detectors (a) 37μm VO_x based detector by NEC, (b) 50μm a-Si based detector by LETI, (c) 40μm YBCO based detector by Mitsubishi [12]........13

Figure 2.1: Key detector noise sources and their NETD contributions to the total NETD. Overall noise of the system is dominated by the flicker noise of the VO_x [15]. 21

Figure 2.2: Transmittance and metal-insulator transition behavior of pure VO_2 (a) and W-doped VO_2 (b) [34]........26

Figure 2.3: TCR dependency on the concentration of VW alloy (a) and TCR dependency on the oxidation time for $V_{0.95}W_{0.05}$ alloy (b) [14]......28

Figure 2.4: An illustration of the diode sputtering mechanism [42]; collision of free electrons with the plasma gas (1), driving off an outer shell electron and ionization (2), acceleration of positively charged ion by the applied electric field (3), ejection of source material in neutral particles (4), deposition of the material on substrate (5). 29

Figure 2.5: The schematic illustration of magnetron sputtering mechanism [43]. 30

Figure 2.6: The schematic of the AJA sputtering system [45]...........31

Figure 2.7: Dependence of NETD on resistance considering self-heating affects [9]. 34

Figure 2.8: Cross sectional (a) and perspective (b) view of planar type resistors. 35

Figure 2.9: Perspective view of serpentinely formed planar structure (finger type) [6]. 35

Figure 2.10: The representative view of a sandwich type resistor structure. 36

Figure 2.11: Cross sectional view of fabrication steps of the planar type resistor. 37

Figure 2.12: Cross sectional view of enhanced sandwich type resistors. 38

Figure 2.13: Cross sectional view of fabrication steps of the enhanced sandwich type resistors. 39

Figure 2.14: Formation of the electrodes using Aqua Regia (5:2:1) is shown for finger structures with both 0.7 µm (a) and 1.5 µm (b) finger thickness. 42

Figure 2.15: HIROX (a) and SEM (b, c) photos of Au etching of 0.5 µm structures. The thinning at the edges in (c) is a result of pyramid-like shaping of the S1805 during hardbaking. 42

Figure 2.16: A VWO resistor which has been etched in diluted hydrogen peroxide at 31:1 ratio. Because the photoresist is not stripped, the undercut can be easily seen at the edges of the active material layer. . 44

Figure 3.1: The thickness measurements are conducted at the numbered points as shown on the template....................................46

Figure 3.2: Deposition rate measurements of V, VO_2, V_2O_5 and W in different deposition power (a), O_2/Ar flow (b) and working pressure (c) conditions. 48

Figure 3.3: Electrode structures used in the selected mask-set for VWO fabrication and characterization. 52

Figure 3.4: The layout of the 6″ wafer used during bolometric characterization studies of VWO film..54

Figure 3.5: A picture of the TCR measurement package...................55

Figure 3.6: The measured resistance vs. temperature (a) and TCR vs. temperature curve of the reference recipe......................................56

Figure 3.7: Arrhenius plot of resistance vs. temperature is linear which shows the resistance change is a thermally activated process.. 57

Figure 3.8: The schematic of the noise measurement circuitry. 58
Figure 3.9: Noise measurement result of the reference recipe...........59
Figure 4.1: Resistivities of the samples deposited at different vanadium power levels. 63
Figure 4.2: TCR measurements of the samples deposited at different vanadium power levels. 64
Figure 4.3: Noise behavior of the samples deposited at different vanadium power levels. 64
Figure 4.4: Resistivities of the samples deposited at different tungsten power levels. 66
Figure 4.5: TCR measurements results of the samples deposited at different tungsten power levels. 67
Figure 4.6: Noise behavior of the samples deposited at different tungsten power levels. 67
Figure 4.7: Resistivities of the samples deposited at different oxygen flow rates. 69
Figure 4.8: TCR measurements of the samples deposited at different oxygen flow rates. 70
Figure 4.9: Noise behavior of the samples deposited at different oxygen flow rates. 70
Figure 4.10: Resistivities of the samples deposited at different argon flow rates. 72
Figure 4.11: TCR measurement results of the samples deposited at different argon flow rates. 73
Figure 4.12: Noise behavior of the samples deposited at different argon flow rates. 73
Figure 4.13: Resistivities of the samples deposited at different working pressures. 75
Figure 4.14: TCR measurement results of the samples deposited at different working pressures. 76
Figure 4.15: Noise behavior of the samples deposited at different working pressures. 76
Figure 4.16: Resistivities of the samples deposited at different substrate temperatures. 78
Figure 4.17: TCR measurements of the samples deposited at different substrate temperatures. 79
Figure 4.18: Noise behavior of the samples deposited at different substrate temperatures. 79

Figure 4.19: Resistivities of the sample annealed for different time periods........81

Figure 4.20: TCR measurements of the sample annealed at 300 °C for different time periods........81

Figure 4.21: Noise behavior of the sample annealed at 300 °C for different time periods........82

Figure 4.22: TCR measurements of the sample exposed to oxygen plasma for different time periods........83

Figure 4.23: Noise behavior of the sample exposed to oxygen plasma for different time periods........84

Figure 4.24: 3D AFM maps taken from samples S3 (a), S5 (b), S1 (c), S10 (d), S18 (e) and 90-minute post-annealed S3 (f).in 0.5 µm x0.5 µm area........88

Figure 4.25: XRD pattern of (100) Si wafer........89

Figure 4.26: XRD results of S3, S5 and post-annealed S3. Measurements are performed using GIXD technique at 2° incidence angle........90

Figure 4.27: Peak fitting of $V2p_{3/2}$ core level for S5 (pure VO_x)........93

Figure 4.28: V2p core level binding energy comparison of undoped (S5) and W-doped (S3) VO_x samples........93

Figure A.1: AFM results of the film fabricated using the recipe of S3 (3D view (a), Phase Imaging Mode (b), and Roughness (c))........104

Figure A.2: AFM results of the film fabricated using the recipe of S3 and exposed to oxygen plasma for 60 minutes (3D view (a), Phase Imaging Mode (b), and Roughness (c))........105

Figure A.3: AFM results of the film fabricated using the recipe of S3 and post-annealed at 300 °C for 90 minutes (3D view (a), Phase Imaging Mode (b), and Roughness (c))........106

Figure A.4: AFM results of the film fabricated using the recipe of S1 (3D view (a), Phase Imaging Mode (b), and Roughness (c))........107

Figure A.5: AFM results of the film fabricated using the recipe of S5 (3D view (a), Phase Imaging Mode (b), and Roughness (c))........108

Figure A.6: AFM results of the film fabricated using the recipe of S10 (3D view (a), Phase Imaging Mode (b), and Roughness (c))........109

Figure A.7: AFM results of the film fabricated using the recipe of S18 (3D view (a), Phase Imaging Mode (b), and Roughness (c))........110

Figure A.8: AFM results of the film fabricated using the recipe of S13 (3D view (a), Phase Imaging Mode (b), and Roughness (c))........111

Figure A.9: AFM results of the film fabricated using the recipe of S12 (3D view (a), Phase Imaging Mode (b), and Roughness (c))........112

CHAPTER 1

INTRODUCTION

History of the infrared radiation begins in 1800 with the discovery of Herschel; that is, the red end of the sunlight after a prism heats a thermometer up much more than the visible portion of the spectrum [1]. This region beyond the visible spectrum is called the infrared spectrum today.

The discovery of Herschel has opened the door of seeing in darkness or obscured visibility. Motivation for that is very simple: the desire of doing things that can be done in luminous conditions. Though using an artificial illumination source or a low-light image intensifiers are the low-cost solutions to that, they suffer from their low illumination range and risk of detectability [2].

The infrared detectors use not the reflected energy in visible spectrum but the radiated energy in the infrared portion of the electromagnetic spectrum. All the hot objects, the objects at a temperature above 0 K, emanate infrared energy depending on their temperature and this emitted energy from a blackbody at an absolute temperature is described by the Planck's law quantitatively. Figure 1.1 shows the spectral exitance of a blackbody at different temperatures. The yellow line in the figure is the spectral exitance regime for the temperature of the sun and it can be seen here that it reaches its peak in the visible region. On the other hand, the spectral exitance of the objects at room

temperature lies outside of the visible range which makes the visibility of these objects impossible without an external illumination source. Infrared detectors solve that problem and make it possible to create an image of any object at room temperature by using the infrared energy emitted.

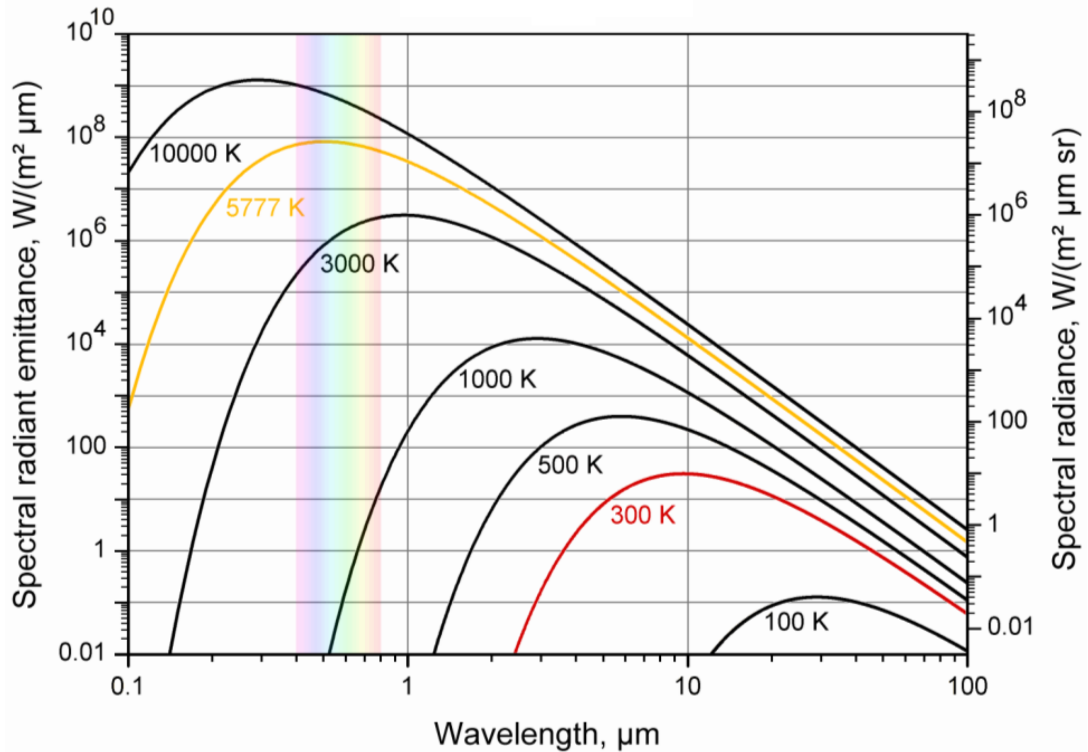

Figure 1.1: The spectral exitance of a typical blackbody. The yellow line shows the regime of the sun surface and the red is the regime of room temperature [3].

Infrared detectors can be divided into two groups: Photon detectors and thermal detectors. Photon detectors are based on the generation of photo current by the creation of electron-hole pairs with the aid of photons. This kind of detectors provides an outstanding performance on the observation of the objects at room temperature. However, their cooling requirement to cryogenic temperature makes these detectors expensive and bulky. The thermal detectors rely on an indirect sensing

in which the radiant infrared energy alters the properties of the temperature sensitive active material by heating it up. This temperature-dependent change in the active material is sensed by a read-out circuitry to create the image. Depending upon their operability at room temperature (RT), the uncooled thermal detectors provide low-cost, low-power consumption, and portability.

This thesis is a study on such an active material which shows a resistive change under an infrared radiation exposure. Generally, an active material for a high-performance uncooled detector should have the properties of low resistivity for the fabrication of acceptable resistive structures, low noise behavior and high TCR. The development of such a material, VWO, has been performed in METU-MEMS Research and Applications Center by using the direct current reactive co-sputtering method.

Following sections of this chapter give comprehensive information about the infrared detection and theory. Section 1 explains the infrared spectrum as a part of electromagnetic spectrum, and Section 2 touches briefly on the detection mechanism. Section 3 provides basic information about the infrared detector types. Section 4 is mainly about the microbolometers and reveals the details of resistive type microbolometers. Section 5 describes the noise contributions to the uncooled detectors. Section 6 explains the most important figures of merit for uncooled detectors, while Section 7 summarizes the objectives of this thesis and the layout.

1.1 Infrared Radiation

The observation of Herschel during his studies with the sunlight was the more heating of the red filter than the filters of other visible regions [1].

This was the first indication of the existence of another emitted energy beyond the red light what is called infrared light. The infrared waves cover a wide range of electromagnetic spectrum which is between wavelengths of 0.74 µm and 1000 µm. Figure 1.2 shows how the infrared region is placed in the electromagnetic spectrum including the sub-regions and the visible region.

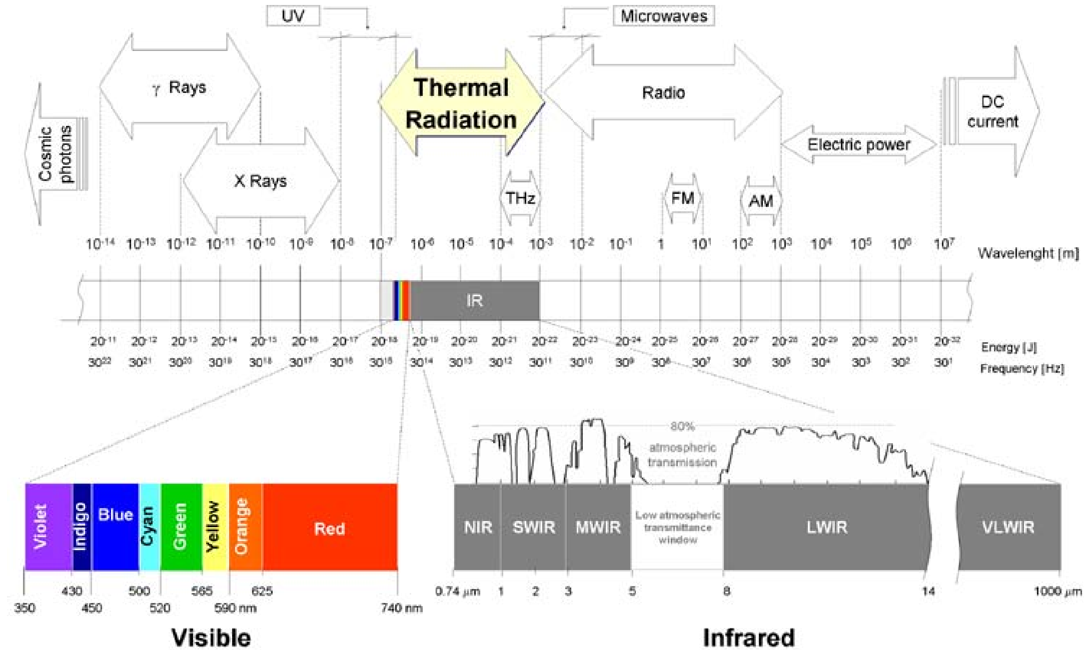

Figure 1.2: The electromagnetic spectrum including the visible and the infrared sub-regions [4].

The infrared region can be divided into 5 main sub-regions. And the transmittance of the atmosphere for infrared rays is different for different regions and wavelengths. Most of the infrared rays are absorbed by the molecules in the atmosphere such as O_2, H_2O, CO_2. Figure 1.3 shows the infrared transmittance of the atmosphere with respect to wavelength.

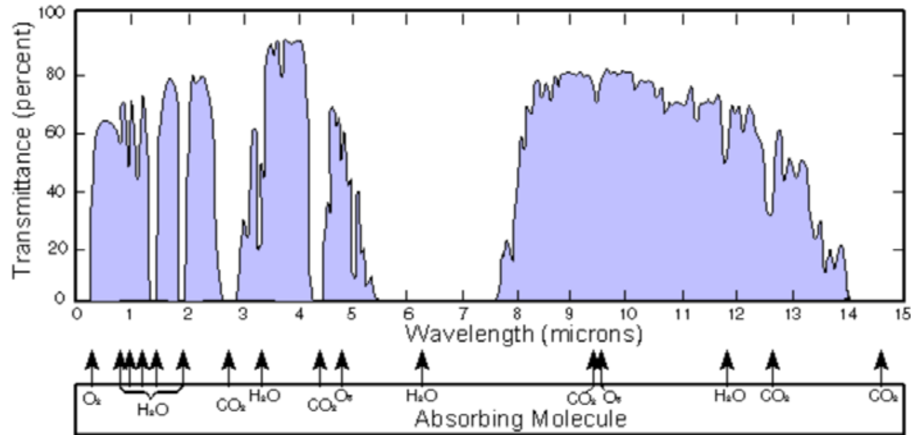

Figure 1.3: Transmittance of the atmosphere with respect to wavelength. The dominant absorbing molecules are indicated in the below box [5].

As seen from Figure 1.3, the atmosphere provides a selective transmission for different wavelengths. The regions out of 3-5 µm and 8-12 µm have very low transmittance which makes the detection of infrared rays impossible. The transmittance of the two main regions is relatively high and enables the detectors to detect the infrared rays.

1.2 Infrared Detection

The detection mechanism of an infrared detector relies on the detection of the emitted infrared power from the target and the detection of current by the creation of electron-hole pairs or the detection of the change in electrical properties.

All objects at a temperature higher than the absolute zero emit infrared power. The blackbody is the reference body and a perfect radiator which has a unity absorbance and emissivity. Absorbance can be defined as the ratio of the absorbed radiance to the incident radiance of an object. The emissivity is the ratio of the emitted power of an object to the

emitted power of the blackbody. Planck's law, which describes the thermal radiation emitted from a blackbody with respect to wavelength, is formulated as follows;

$$M_e(\lambda, T) = \frac{2\pi hc^2}{\lambda^5 (e^{\frac{hc}{\lambda kT}} - 1)} \tag{1.1}$$

where M_e spectral exitance, λ is the wavelength, k is the Boltzmann constant, h is the Planck's constant, T is the temperature, c is the speed of light. Integration of this equation over the interested band and the multiplication of the result with surface area of the blackbody give total thermal radiation at a specific temperature.

The wavelength where the maximum radiance takes place can be found by equalizing the derivative of Equation 1.1 to zero. This point is expressed by the Wien's Displacement Law as follows;

$$\lambda_{max} = \frac{2898}{T} \tag{1.2}$$

where λ_{max} is the wavelength of maximum radiance in μm and T is the temperature in K. The peak wavelength of the spectral distribution for a blackbody at room temperature is around 10 μm which is the mid-point of the 8-12 μm band (Figure 1.4).

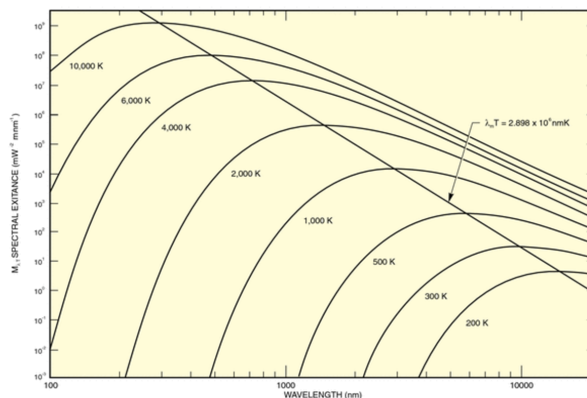

Figure 1.4: The spectral exitance of various kinds of blackbodies at different temperatures. The straight line shows the peak points of the exitance according to Wien's Displacement Law [6].

This is another important aspect of the detector for the choice of working band depending on the temperature range of the target.
Figure 1.4 also shows that the wavelength of the maximum radiance moves towards shorter wavelengths as the temperature of the object increases. Hence, 3-5 μm band is a more convenient choice for the observation of the hotter objects.

1.3 Infrared Detectors

Detection of the infrared radiation can be analyzed in three main categories: photon detection, wave interaction detection and thermal detection [7].

Photon detection mechanism mainly depends on the detection of the changed electronic energy distribution [8] as a result of the interaction of incident photons with electrons of the sensitive material and creation of photo-excited carriers. The optimum performance of photon detectors is achieved at the lowest ratio of thermally generated carriers to those photo-excited carriers. This is only possible by cooling the detector to cryogenic temperatures according to the detector design and the working temperature. This cooling requirement accompanies the use of special pumping systems which increases the cost substantially [9]. The detectors based on this mechanism perform an extraordinary performance at the expense of portability and higher cost because of their cooling requirement.

The wave interaction detection of the infrared radiation relies on the detection of the intensity of incident electromagnetic radiation and sensing the magnitude of the electric field vector. However, none of the studies based on this theory has given practical results for the detection of infrared radiation [7].

Thermal detectors, the third class of IR detectors, operate by sensing the change in a measurable property of a material due to the temperature rise as a result of absorption of the incident infrared energy. Hence, a heat flow equation which describes the change in temperature as a result of incident energy forms the basis for the thermal infrared detection mechanism. Figure 1.5 shows a principle structure of a thermal infrared detector.

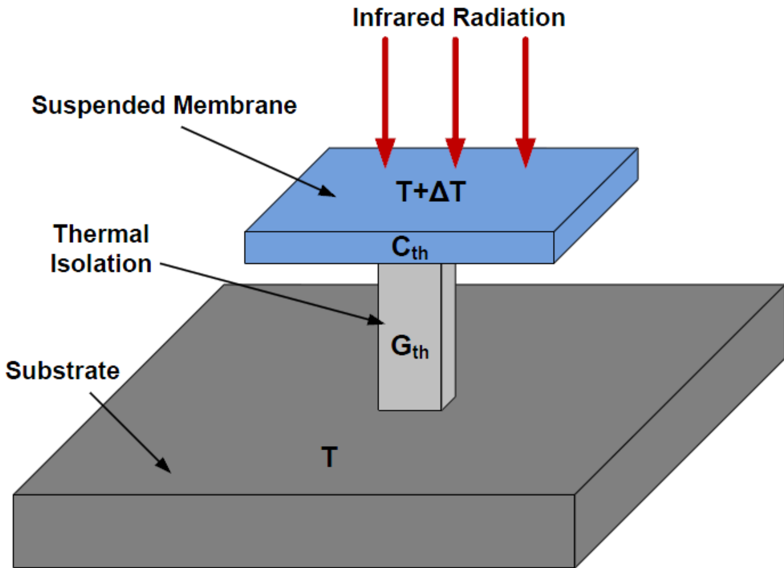

Figure 1.5: The principle structure of a thermal infrared detector [9].

As seen from the figure, the substrate and the suspended membrane which is the sensitive part of the detector with the thermal capacitance of C_{th} are thermally isolated from one another by a heat sink with the thermal conductance of G_{th}.

The temperature of the suspended membrane is raised up as a result of the absorbed infrared radiation while the substrate is kept at a constant temperature via heat sink. This temperature change results in a change in a measurable property of a sensitive material and this change can be measured as follows [2];

- Resistance change (bolometer)
- Thermoelectric effect
- Pyroelectric effect
- Oil-film evaporation (evaporagraph)
- Semiconductor absorption-edge shift
- Thermoelastic effect
- Liquid crystal color change
- Gas pressure change (Golay cell)

Because of their indirect detection mechanism, overall performance of a thermal detector is not as good as photon detectors. Nonetheless, their operability at room temperature without cooling requirement makes them much more affordable and portable for industrial, medical, scientific, and military applications.

Among the above-mentioned techniques, the principal ones shown to date are the resistive bolometric effect, the thermoelectric effect and the pyroelectric effect.

VWO, the main subject of this thesis study, is a material for the resistive applications which changes its resistivity under incident infrared radiation. The rest of this section gives detailed information regarding the resistive microbolometer structure.

1.4 Microbolometers

The first bolometer dates back to 1880, as Samuel Pierpont Langley constructed the first thermal infrared detector [6]. The design was quite simple but successful. He used two identical platinum strips as resistance instead of R_1 and R_2 in the Wheatstone bridge in Figure 1.6. Only one of them is covered with lampblack so it is isolated from the infrared radiation. As the other strip is exposed to IR, platinum heats up

and resistance changes, as a consequence, the balance of the Wheatstone bridge is distributed. This design was fine enough to sense a cow from a quarter mile away.

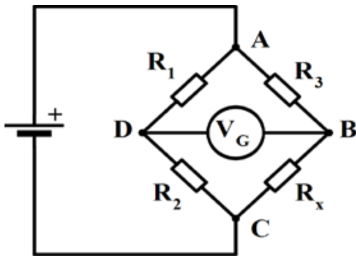

Figure 1.6: The Wheatstone bridge, Rx/R3=R1/R2 for V_g is balanced [10].

Roughly 100 years after the very first bolometer in 1880, first micromachined bolometric infrared imaging array was constructed by the team of R.Andrew Wood at the Honeywell Technology Center [2,6].

A very commonly used approach to the microbolometer today is the placing of the resistive bridges on top of the CMOS read-out circuit by surface micromachining.

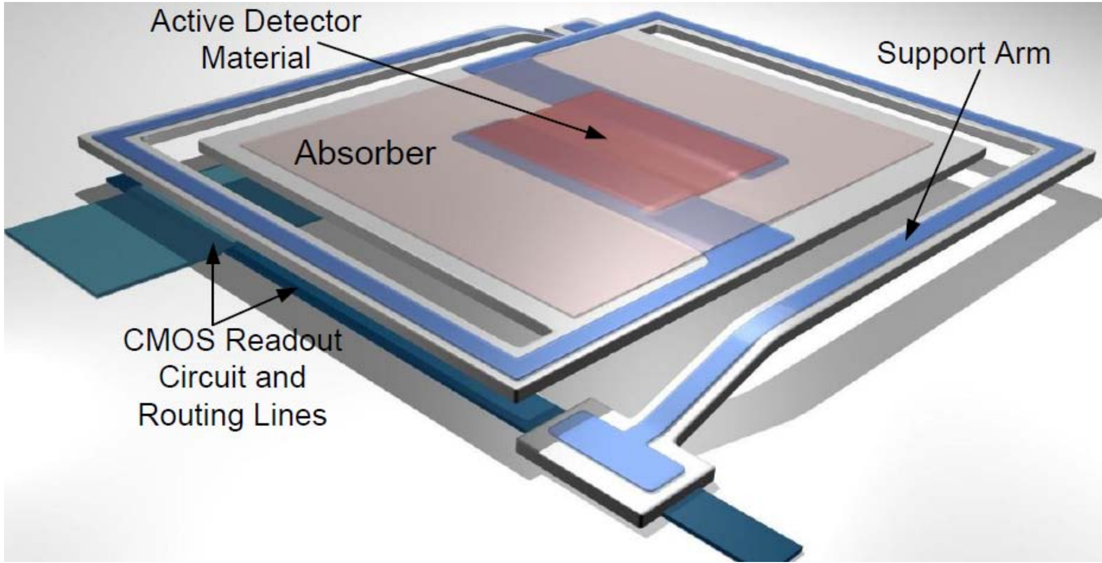

Figure 1.7: A representative perspective view of a microbolometer detector pixel [6].

In Figure 1.7, the bridge is thermally isolated by destroying the physical contact between the bridge and the surroundings. The incident infrared radiation on the bridge increases the temperature of the material as the suspended structure is thermally isolated. The infrared sensitive material on the body of the pixel shows reaction to this temperature change by changing its electrical properties and this change is measured by a CMOS read-out circuitry for the image generation.

Microbolometers can be classified under two subcategories: diode type microbolometers and resistive type microbolometers. These are summarized in two different sections below, with more emphasis on the resistive type microbolometers as this study aims to develop an active detector material for resistive type microbolometers.

1.4.1 Diode Type Microbolometers

This type of microbolometer uses the change in the diode current or voltage due to temperature change and is fabricated by using bulk-micromachining methods. The forward current of the diode shows a temperature dependent property [11] and this dependency can be extracted from:

$$I_d = I_s\left(e^{qV_d/nkT} - 1\right) \tag{1.3}$$

Where I_d is the diode forward current, I_s is the saturation current, V_d is the forward bias voltage, q is the electron charge, k is the Boltzmann constant and T is the temperature.

Fabrication of this kind of detectors is rather straightforward which reduces the price significantly. However, the performance they can offer is much lower in terms of sensitivity. Therefore, these kinds of detectors are generally preferred for applications where the image quality is not much crucial [9].

1.4.2 Resistive Type Microbolometers

Different from the diode type microbolometers, resistivity of the material shows a temperature dependency and as the temperature of the material increases as a result of infrared radiation the resistivity changes. The change in the resistivity as a function of temperature which is called TCR can be expressed as follows:

$$\alpha = \frac{1}{R}\frac{dR}{dT} \tag{1.4}$$

Where α is the TCR, R is the resistance and T is the temperature. TCR of a material shows the rapidness of the resistance change and determines the sensitivity of the material to a change in temperature. Thus, the TCR comes up as an important property of the material.

Various kinds of materials are used to date as a temperature sensing material. Today, the manufactured microbolometers are based on three common materials which are VO_x, amorphous silicon (a-Si) and YBCO [12].

VO_x proved to be successful after it was used by the Honeywell in 1983 as the first demonstration of the resistive bolometric array [2]. Its TCR value of 2-3 %/K and low noise property make it a good choice for the uncooled resistive infrared imager manufacturers Raytheon, Indigo, Lockheed Martin, DRS, BAE which have the license. A-Si providing TCR value of 2-3 %/K is another material for resistive microbolometer application. The companies ULIS and LETI use this material for their uncooled applications. YBCO is a relatively new material which exhibits a TCR over 3 %/K. This material has been used in Mitsubishi Electric Corporation and University of Texas at Arlington [6]. YBCO is also the basic material used in METU-MEMS Research and Applications Center for research studies. VWO is also a new material in the field. Studies of Moon with this material show promising bolometric properties with the TCR above -3 %/K and low flicker noise contribution [13, 14].

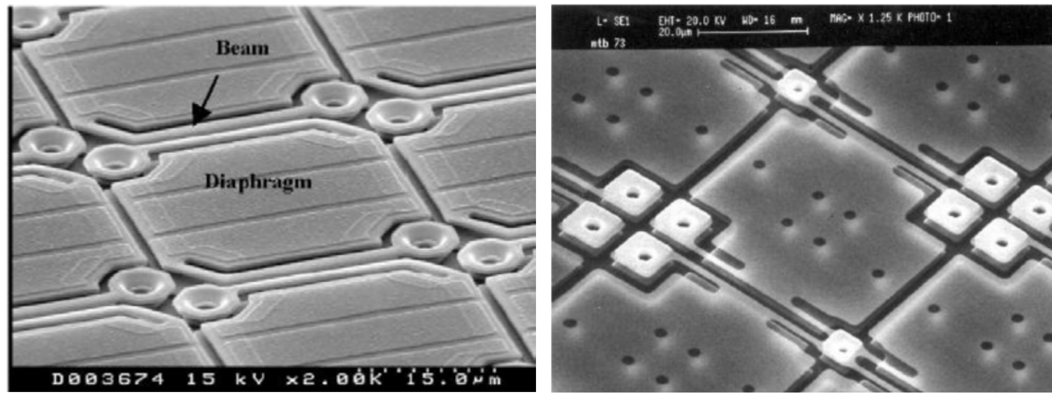

(a) (b)

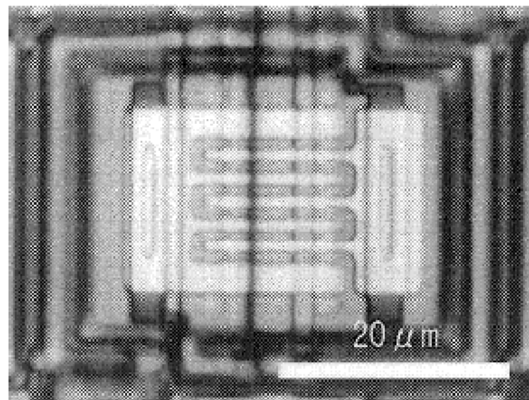

(c)

Figure 1.8: SEM images of some state of art detectors (a) 37µm VO_x based detector by NEC, (b) 50µm a-Si based detector by LETI, (c) 40µm YBCO based detector by Mitsubishi [12].

1.5 Noise in Resistive Bolometers

All kinds of infrared detectors have different noise contributions. The noise contributions in the thermal detectors can be classified under three categories: Johnson noise, 1/f noise (flicker noise), and thermal fluctuation noise [15].

Johnson noise, present in all resistors and equal at all frequencies, is caused by the thermal agitation of charge carriers in resistive structure as a result of the voltage fluctuations across its terminals.

This fluctuation is independent of the applied bias and can be expressed as:

$$V_{n,Johnson} = \sqrt{4kTR\Delta f} \tag{1.5}$$

Where k is the Boltzmann constant, T is the temperature, R is the resistance of the resistive structure and Δf is the electrical bandwidth.

Flicker noise is the second noise source and currently has the highest contribution to the total noise of the microbolometer system. The flicker noise is highly frequency dependent and has a characteristic 1/f power spectral density at all frequencies [15]. The formula of the flicker noise can be given as:

$$V_{n,1/f} = \sqrt{\int_{f_2}^{f_1} \frac{V_d^2 k_{1/f}}{f} df} = V_d \sqrt{k_{1/f} \ln \frac{f_2}{f_1}} \tag{1.6}$$

where V_d is the detector bias, $k_{1/f}$ is the flicker noise constant, f_1 is the lower noise bandwidth limit, f_2 is the upper noise bandwidth limit. Though the main reason for the existence of this noise is still ambiguous, it appears to result from the imperfections in the material, deposition conditions or electrical contacts [2].

Thermal fluctuation noise results from the heat exchange between the body of the bolometer and its ambience. The suspending body of the bolometer is combined to the substrate. Any temperature difference either in the body or in the substrate causes a heat exchange between them. The root mean square (rms) value for temperature fluctuation noise is given as [6]:

$$V_{n,TF} = R_V \sqrt{\frac{4kTG_{th}}{\mu}} \tag{1.7}$$

where R_V is the voltage responsivity, k is the Boltzmann constant, T is the temperature, G_{th} is the thermal conductance and μ is the absorbance

of the detector. However, because today's bolometers are generally kept at a constant temperature and work in a vacuum environment, the contribution of thermal fluctuation noise to the total noise is very small and is generally ignored at noise calculations.

1.6 Important Figures of Merit for Bolometers

The most important figure of merits for microbolometers are the responsivity ($\mathcal{R}$), noise equivalent power (NEP), noise equivalent temperature difference (NETD) and detectivity (D^*).

1.6.1 Responsivity ($\mathcal{R}$)

Responsivity is the voltage or current read from the output for a unit power of incident infrared energy. Its measurement depends on the biasing method and can be measured in either A/W or V/W. The expression for both current responsivity ($\mathcal{R}_I$) and voltage responsivity ($\mathcal{R}_V$) can be given as:

$$\mathcal{R}_V = \frac{\mu I_d R_d \alpha}{G_{th}\sqrt{1+(\omega\tau)^2}} \quad (1.8)$$

$$\mathcal{R}_I = \frac{\mu V_d \alpha}{R_d G_{th}\sqrt{1+(\omega\tau)^2}} \quad (1.9)$$

where $\mathcal{R}_v$ is the voltage responsivity, $\mathcal{R}_I$ is the current responsivity, μ is the absorbance of the detector, I_d is the detector bias current, V_d is the detector bias voltage, R_d is the detector resistance, α is the TCR of the active material, G_{th} is the thermal conductance, ω is the input signal modulation and τ is the thermal time constant. Both equations show that the responsivity directly depends on the TCR.

1.6.2 Noise Equivalent Power (NEP)

The noise equivalent power (NEP) can be defined as the amount of absorbed infrared energy by the detector which generates an output signal equal to *rms* of total noise. This parameter has the unit of Watt (W) and can be expressed:

$$NEP = \frac{V_n}{R_v} \tag{1.10}$$

where V_n is the total rms noise and R_v is the voltage responsivity.

1.6.3 Noise Equivalent Temperature Difference (NETD)

The noise equivalent temperature difference is an indispensable performance parameter for infrared imaging systems. It can be explained as the temperature difference between two side-by-side blackbodies which give an electrical output difference equal to unity signal to noise ratio between two halves of the array when viewed by an infrared imaging system [16]. Niklaus *et al.* suggested a comprehensive model for the NETD calculation and the expression is given as [17]:

$$NETD = \frac{4F^2 V_n}{\mathcal{R}_V A \emptyset_{\lambda_1-\lambda_2} (\frac{\Delta P}{\Delta T})_{\lambda_1-\lambda_2}} \tag{1.11}$$

where F is the f-number of the optic, V_n is the total noise voltage of the system including read-out circuitry, $\mathcal{R}_v$ is the responsivity, A is the pixel pitch, Φ is the transmission of interested bandwidth, $(\Delta P/\Delta T)_{\lambda_1-\lambda_2}$ is the change in power per unit area by incoming radiation from a blackbody at temperature T (the temperature contrast) [6].

Because the NETD, the most significant performance parameter, defines the smallest sensible temperature variation of a bolometric array, the smallest NETD is always desirable. Such a small NETD can be obtained

by a lower noisy system, higher pixel area and responsivity and optics with smaller f-number.

1.7 Objectives and Organization

The goal of this thesis is to develop a new material, namely Vanadium-Tungsten-Oxide, which is compatible with the monolithic CMOS fabrication by using DC magnetron reactive co-sputtering technique. What is expected from this material is reflecting high performance properties such as high TCR, low noise behavior and reasonable resistivity for bolometric applications. The specific objectives of this study are listed below:

1. Determination of reference deposition conditions. A reliable sputtering recipe is needed to fabricate a film which has reasonable bolometric properties to take as a reference. Hence, making an optimization on this recipe is much more sensible and straightforward.

2. Investigation of the effects of deposition conditions on bolometric properties and definition of an optimized recipe. The sputtering parameters change the bolometric properties of the deposited film. Thus, how the bolometric properties change as a result of change in deposition parameters should be analyzed and as a result an optimized recipe which gives a good uniformity besides good bolometric properties should be defined for fabrication.

3. Selection of the resistive electrode structure for experiments conducted within this thesis study.

4. Determination of the etching method for both electrode and active material layers. Selectivity of the proposed etchant is an essential

point which enables to fabricate the resistive structure on a suspended bolometric structure.

5. Tests and Characterization of the developed material. Definition of the material structure by XRD, XPS, and AFM characterization methods is quite important in terms of establishing a relationship between the material structures and deposition conditions together with bolometric properties.

The contents of the following chapters can be summarized as follows:

Chapter 2 discusses and elaborates on the details of active materials for bolometers and active material selection, presents an introduction regarding the deposition method and resistive electrode structures and explains the etching optimization for both electrode and active material layers.

Chapter 3 is mainly about the fabrication of the newly developed material for bolometric applications. It explains the preliminary works before fabrication studies and reveals the attained reference recipe. At the same time, it discusses the test methods concerning bolometric characterization including the test results of reference recipe.

Chapter 4 focuses on the experimental results and both bolometric and structural characterization of deposited films under various sputtering conditions. It also makes a comparison between the optimized VWO and YBCO in view of enhanced-sandwich type structure.

Chapter 5 concludes the studies about VWO deposition and defines the future works to that will improve the results.

CHAPTER 2

ACTIVE DETECTOR MATERIALS AND FABRICATION DETAILS

This chapter explains the active detector materials used in uncooled microbolometer technology and gives details about the fabrication of VWO resistors. Section 2.1 provides general information regarding active materials in literature and industry, and it also compares the basic bolometric properties of these materials. Section 2.2 is principally about the target material, VWO. It mentions the reasons behind the doping idea of VO_x while it gives information regarding its applicability in bolometers according to poor literary sources. Section 2.3 reveals the theory of sputtering method and the specifications of the sputtering system which is used during VWO deposition studies. Section 2.4 defines the structures which can be used for resistor fabrication using VWO or other suitable active materials for bolometric applications. The etching optimization studies regarding VWO and electrode layers including both wet and dry etching has been discussed in Section 2.5.

2.1 Determination of Active Material

Choice of the active material is the most significant step which directly defines the performance of a well designed detector and determines the electrical parameters.

In order to make sensible determination, one needs to take the TCR property, noise behavior, resistivity and the process compatibility of the material into account.

TCR, as described in Chapter 1 is a pure property of the material with no tradeoff. A high TCR value is always desired due to its direct inverse relation with the resultant NETD. Table 2.1 summarizes the general TCR values of the most common materials used in fabrication of resistive microbolometers [18, 19].

Table 2.1: General TCR values of the common materials for bolometric applications [18, 19].

Material	TCR (%/K)
VO_x	-2 to -3
a-Si:H	-2.4 to -4
Si_xGe_{1-x}	-2.4
YBCO	-2.99 to -3.5
Poly-Si	-0.7 to -3.7

Noise in microbolometers is another issue which is highly material dependent. Thermal fluctuation noise which is mainly related to the thermal structure of the detector is known as a fundamental limit on the detector performance. However, for bolometers which operate out of temperature fluctuation noise limits because of their low thermal conductance (G_{th}), other noise sources (Flicker noise and Johnson noise) generally dominate the overall system noise. Figure 2.1 shows a result of NETD contributions of different noise sources in a VO_x based detector fabricated by BAE Systems.

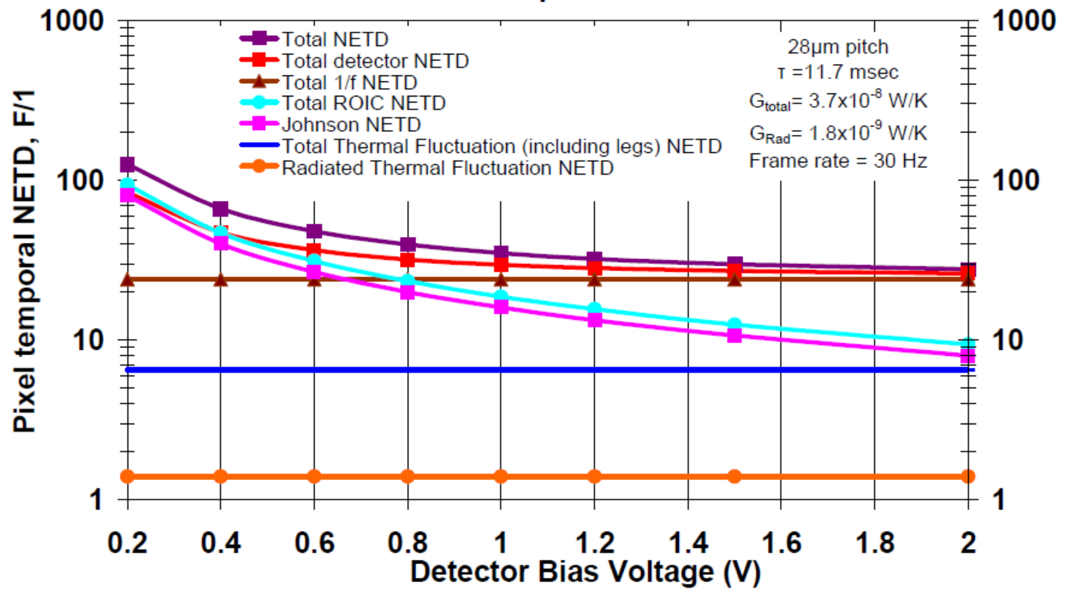

Figure 2.1: Key detector noise sources and their NETD contributions to the total NETD. Overall noise of the system is dominated by the flicker noise of the VO_x [15].

As seen from the figure, the flicker noise of the active material has a limiting and dominating effect on the performance of the microbolometer while the Johnson noise which occurs in all kinds of resistors approach the thermal fluctuation noise at high bias voltages. The resistivity of the active material should also be taken into account for the reason of its indirect effect on the determination of the electrode structure. The geometrical shape of the electrode structure is defined according to the resistivity of the material for the purpose of acquiring desired resistance values at the end of the fabrication. This criterion also affects the size of the pixel as well as the absorption parameter.

The process of the chosen material should also be compatible with the other steps and layers of the fabrication. The temperature is the most restrictive parameter because of the metal layers in a monolithic CMOS fabrication technique. Hence, all the fabrication and the lithography steps of the material should be conducted below 400 °C [20].

On the other hand, the etching of the material must be conducted selectively without any hazard to pre-deposited layers.

2.1.1 Comparison of Active Materials

Since the development of the first bolometer structure using VO_x by Honeywell, a great effort has been spent on the usage of different kind of materials as bolometric material. The materials can be arranged as;

- vanadium oxide (VO_x)
- amorphous Silicon (a-Si) or poly-Si
- amorphous silicon carbide (a-SiC)
- amorphous yttrium barium copper oxide (a-YBCO)
- amorphous or poly silicon germanium (a-SiGe)
- germanium silicon oxide ($Ge_xSi_{1-x}O_y$)
- manganites ($Ln_{1-x}A_xMnO_3$)

Companies and institutions working on the resistive bolometer technology are given in Table 2.2 [14, 16, 18, 21-27]. As can be seen from the table, the most popular materials used by the foundations are VO_x, a-Si, poly-SiGe, $Si_xGe_{1-x}O_y$ YBCO and metals like titanium.

VO_x is known to be the most widely used material for commercialized uncooled microbolometer applications. The most important reason for the favor of VO_x in uncooled infrared imaging technology is surely its bolometric properties as described above in this chapter. While it provides a favorable TCR between -2 and -3 %/K, it comes into prominence with its low resistivity, low noise behavior and CMOS process compatibility. A comparison of the flicker noise, which is the dominant noise source of microbolometers, with different materials is given in Table 2.3. It is obvious that VO_x and as a VO_x based material VWO show relatively low noise properties.

Table 2.2: Foundations and their active materials [14, 16, 18, 21-27].

Country	Foundation	Material
USA	Raytheon	VO_x, a-Si
	BAE	VO_x
	DRS	VO_x
	Sarcon	-
	Indigo	VO_x
	InfraredVision Technologies	VO_x
	University of Texas	YBCO, $Si_xGe_{1-x}O_y$:H
	University of Michigan	-
	FLIR	VO_x
	L-3	VO_x, a-Si, a-SiGe
Canada	INO	VO_x
	Carleton University	$Ge_xSi_{1-x}O_y$
France	ULIS	a-Si
	LETI LIR	a-Si
Japan	NEC	VO_x
	Mitsubishi	YBCO
Korea	KAIST	VO_x, VWO
UK	QinetiQ	metal, Ti
Belgium	XenICs	Poly-SiGe
	IMEC	Poly-SiGe
Israel	SCD	VO_x
China	Huazhong University	VO_x
	Institute of Microelectronics	Poly-SiGe
Russia	Vavilov Optical Institute	VO_x
	Russian Academy of Sciences	VO_x
India	Bharathiar University	VO_x

Table 2.3: Comparison of flicker noise values with different materials in literature [13, 24].

Material	1/f noise (V^2/Hz)
VWO	4×10^{-15} @ 20 Hz, 5.4 μA
VO_x	2.3×10^{-14} @ 30 Hz, 25 μA
a-YBCO	9×10^{-14} @ 20 Hz, 0.41 μA
Poly-Si	9×10^{-14} @ 10 Hz
Manganites	5×10^{-13} to 2e-12 @ 10 Hz, 1 μA
a-$Ge_xSi_{1-x}O_y$	7×10^{-13} @ 250 Hz, 4 μA
Doped a-Si	81×10^{-8} @ 25 Hz
a-Si	4×10^{-12} @ 1Hz, 33 nA
Sputtered a-Si:H	5×10^{-8} @ 10 Hz, 160 mA
PECVD a-Si:H	1.1×10^{-6} @ 10 Hz, 160 mA
a-SiC:H	8×10^{-14} @ 20 kHz
Poly-SiGe	1×10^{-11} @ 1Hz

Vanadium metal forms a great number of oxide phases and all of these show a metal-insulator transition at critical temperatures specific to their stoichiometric phases [28]. However, just a few of these phases are stable enough for microbolometer applications, and these include V_2O_3, VO_2 and V_2O_5 [29]. The transition temperature of these states are 155 K for V_2O_3, 530 K for V_2O_5 and 340 K for VO_2 which is a very useful temperature also for other technological applications such as optical switching and limiting thermal relays [30]. While each of these states has its own drawbacks, the mixed form of these states shows prominent bolometric properties. As V_2O_3 provides a very low resistivity which couples with a low noise contribution, its TCR value is not as good as the other phases. The VO_2 phase is normally the desired form of this bolometric material which offers low resistivity with high TCR; however the fabrication of VO_x in this state necessitates high cost ion beam

techniques. The V_2O_5 phase has also good TCR but its resistance is very high causing high noise in device [31].

Another material that is successfully used in microbolometer technology is a-Si. While it provides a good TCR value between -2 and -3 %/K, its high resistivity requires a high temperature annealing that makes the monolithic integration somewhat difficult. This material can be deposited at low temperatures as low as 75 °C. The TCR and sheet resistance properties depend on the doping concentration, deposition and annealing temperature [16].

YBCO is a relatively new material which exhibits a TCR up to -3.5 %/K with a fair noise level. It is a superconducting material which exhibits a crystallographic and amorphous structure depending on its deposition technique. However, for the semiconductor applications such as the case being considered, it can be deposited in amorphous form by RF sputtering at room temperature without any need of annealing. YBCO is also the base material of the bolometer related works at METU [6, 9, 11, 12].

2.2 Vanadium Tungsten Oxide (VWO) as an Active Material

Both vanadium oxide and tungsten oxide have been known as extensively studied materials for electrochromic and thermochromic applications [32]. The unique reversible metal insulator transition property of vanadium dioxide at 68 °C has aroused interest in its applicability in electrochromism and thermochromism. Its high transparency to visible and IR region of the electromagnetic spectrum in semiconductor phase and low transparency to IR region at metallic phase evoked the idea of using this material for optical switches, smart window applications etc.

Having the capability of altering this transition temperature is also an important issue which enlarges the application field of this material. In early 1970s, Eastwood *et al.* focused on the changing transition temperature of vanadium dioxide (VO_2) by doping with tungsten (W) and germanium (Ge) and patented [33]. This method is still a research subject for the smart windows applications today. Figure 2.2 is an example of this application and shows a comparison of the deposited VO_2 film both in W-doped and pure form. It is apparent that the transition temperature of the pure VO_2 is reduced from 63 °C to 28 °C which is very close to room temperature as a consequence of increasing W content in VO_2 film. However, the mechanism that leads to the reduction of transition temperature due to incorporation of dopants in the VO_2 lattice is not yet well understood [34].

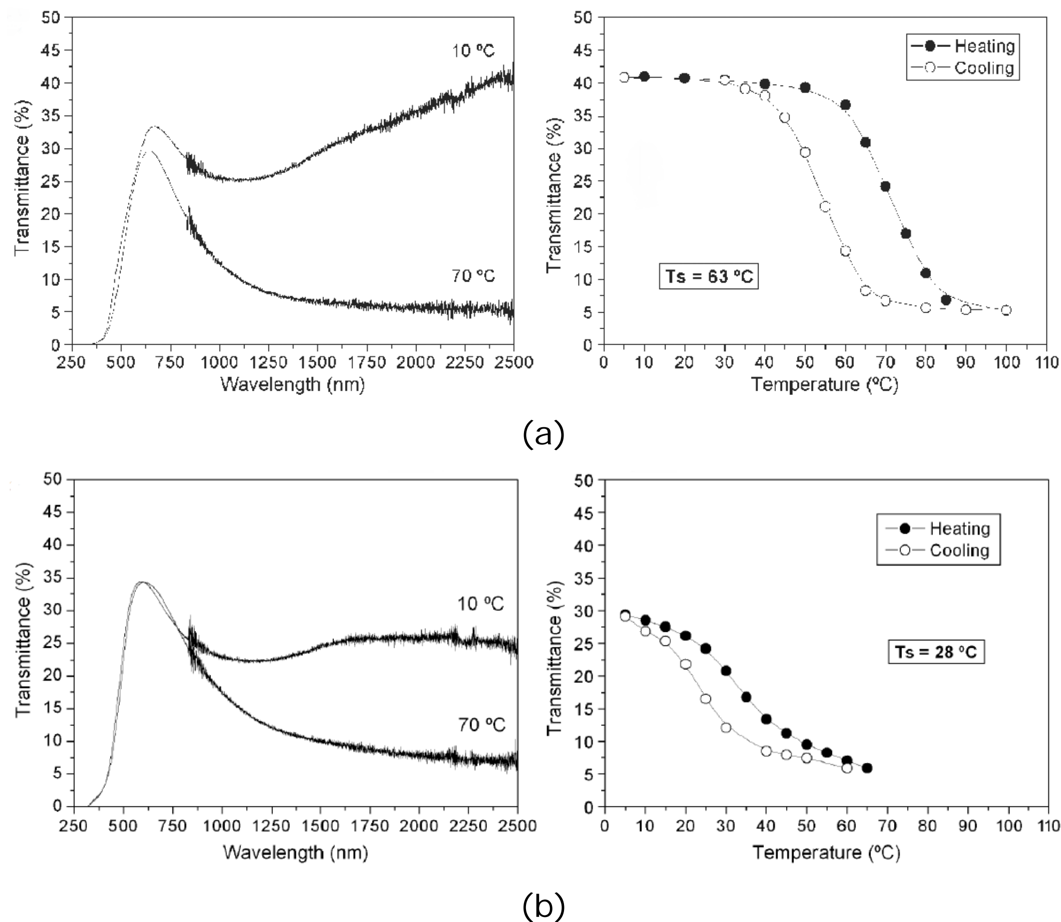

Figure 2.2: Transmittance and metal-insulator transition behavior of pure VO_2 (a) and W-doped VO_2 (b) [34].

In terms of microbolometers, the studies regarding curing the general downsides of vanadium oxide such as its high resistive phases and difficulties in fabrication in stable phases, were first licensed by Jackson Jr. *et al.* in 1994 [35]. This invention was solely focused on the resistivity property of vanadium oxide and managed to decrease the resistivity by W-doping using reactive co-sputtering method. However, his invention gives a rough description about the doping effect of tungsten on the target material and does not reveal any information regarding the other bolometric properties related to the performance [36].

The literary sources on W-doped vanadium oxide for bolometric applications have been very poor till early 2000s. In 2004, Moon announced their studies in Korean Institute of Science and Technology (KIST) and came up with a new fabrication method of VWO for uncooled infrared imaging with its promising bolometric properties [14]. The fabrication of the bolometric material has been performed in two steps; deposition and oxidation. The concentration of deposited VW alloy has been controlled by the number of the tungsten chips attached on the V target and both V and W co-sputtered in argon (Ar) plasma without any oxygen access. Following the deposition step by conventional RF sputtering, the oxidation has been executed as a second phase in oxygen ambiance at 300 °C intending to allow oxygen to react with the VW thin film and to diffuse into the alloy for various time periods. While it has been generally hard to oxidize vanadium metal below 400 °C, oxidation of vanadium-tungsten alloy at lower temperatures has been accomplished. Another observation has been the increase in resistivity caused by the increase in tungsten concentration which means that the addition of tungsten to vanadium brings about an easier oxidation. It has been found that the deposited VWO has TCR values in range of -1.5~-4 %/K on the variation of W concentration and oxidation time [14, 37-41]. The dependency of TCR on the concentration of W and the oxidation time is presented in Figure 2.3. It is evident that

the W concentration below 10% gives desirable high TCR values. The noise performance of VWO fabricated by this group has also showed a staring result as spoken in Section 2.1.1.

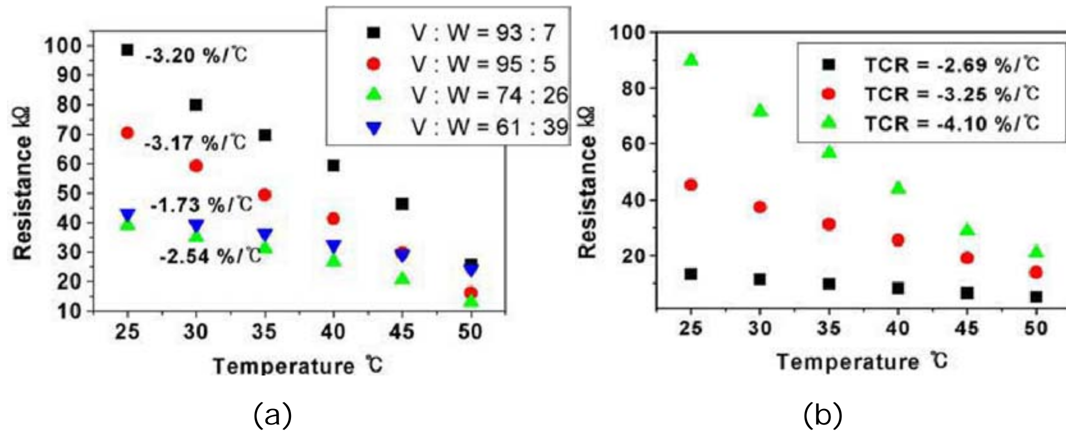

(a) (b)

Figure 2.3: TCR dependency on the concentration of VW alloy (a) and TCR dependency on the oxidation time (▲- 90 minutes,●- 60 minutes, ■-30 minutes) for $V_{0.95}W_{0.05}$ alloy (b) [14].

In light of this limited information on microbolometer applications of this material, the promising and improvable bolometric properties of VWO and the feasibility of our facility for the fabrication, research for this material had been worth studying.

The studies which are subject of this thesis study have been carried out in METU-MEMS Research and Applications Center. Differently from the other sputtering techniques in literature for bolometric applications of VWO, the depositions have been performed using DC reactive magnetron co-sputtering technique using vanadium and tungsten targets separated from each other.

2.3 Sputtering and the Deposition System

Sputtering is a physical vapor deposition method which relies on the ejection of the atomic particles from a solid target via collision and erosion by energetic ions. The mechanism of sputtering is visually explained in Figure 2.4.

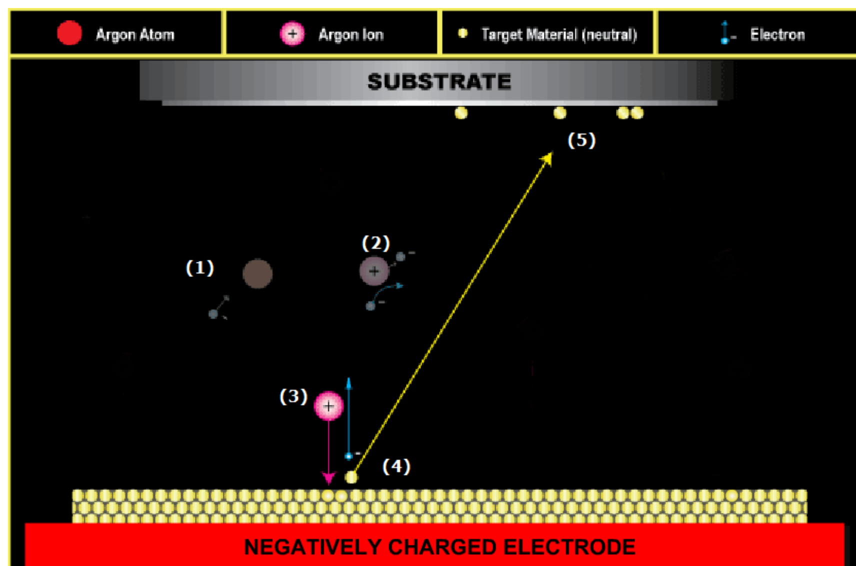

Figure 2.4: An illustration of the diode sputtering mechanism [42]; collision of free electrons with the plasma gas (1), driving off an outer shell electron and ionization (2), acceleration of positively charged ion by the applied electric field (3), ejection of source material in neutral particles (4), deposition of the material on substrate (5).

At the very first step, gaseous plasma is needed to be created inside the sputtering chamber for the generation of ions. Ar is the most commonly used gas for this purpose owing to its inert and relatively cheap properties [11]. In a diode sputtering system, the target (cathode) is generally negatively biased while the substrate (anode) is held neutral. Free electrons are accelerated by the effect of electric field as a result of potential difference in vacuumed chamber and collide with Ar atoms.

This collision culminates in positively ionization of the Ar atoms which forms the plasma. The electric field speeds up the positively charged Ar^+ ions towards the target. As the Ar^+ ions bombard the surface of the target material, they erode and eject neutral clusters from the target. These ejected clusters travel in a path till they find a contact surface. When a substrate is placed on the path, it gets deposited by the target material [42].

There are two major problems concerning to diode sputtering method; low deposition rate, and overheating and structural damage to substrate resulting from continuous electron bombardment.

Magnetron sputtering is the enhanced version of diode sputtering which uses the magnetic field of magnets below target to eliminate these two main drawbacks of diode sputtering. The magnets placed below the target create a magnetic field that traps the free electrons. While this method solves the continuous electron bombardment at the substrate site, as seen from the Figure 2.5 excess of electrons above the target material increase the probability of Ar ionization remarkably which lead to higher deposition rate [42].

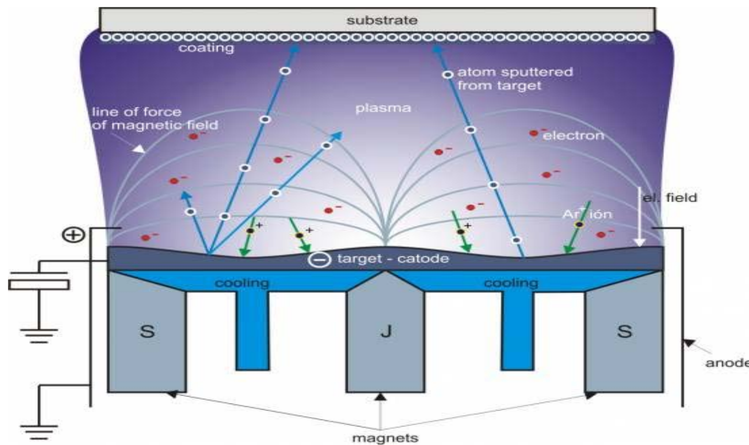

Figure 2.5: The schematic illustration of magnetron sputtering mechanism [43]. The secondary electrons resulting from the free electron-Ar collision and Ar bombardment of the target surface are trapped in the magnetic field just above the target surface.

The potential difference between target and substrate is created by DC or RF sources. A DC source is generally preferred for use in metal targets. However, because of the charge accumulation on the surface of dielectric targets, RF sources are used for insulator deposition.

For the VWO deposition studies in METU-MEMS Research and Applications Center, the product of AJA Company is used as the sputtering system (Figure 2.6). The chamber used for VWO deposition consists of three sputtering sources; one RF source and two DC sources. DC sources are used for the sputtering of VWO because of the metallic property of the W and V targets, and better electrochemical and structural properties of the VO_x which is the main material in the fabricated thin film [44].

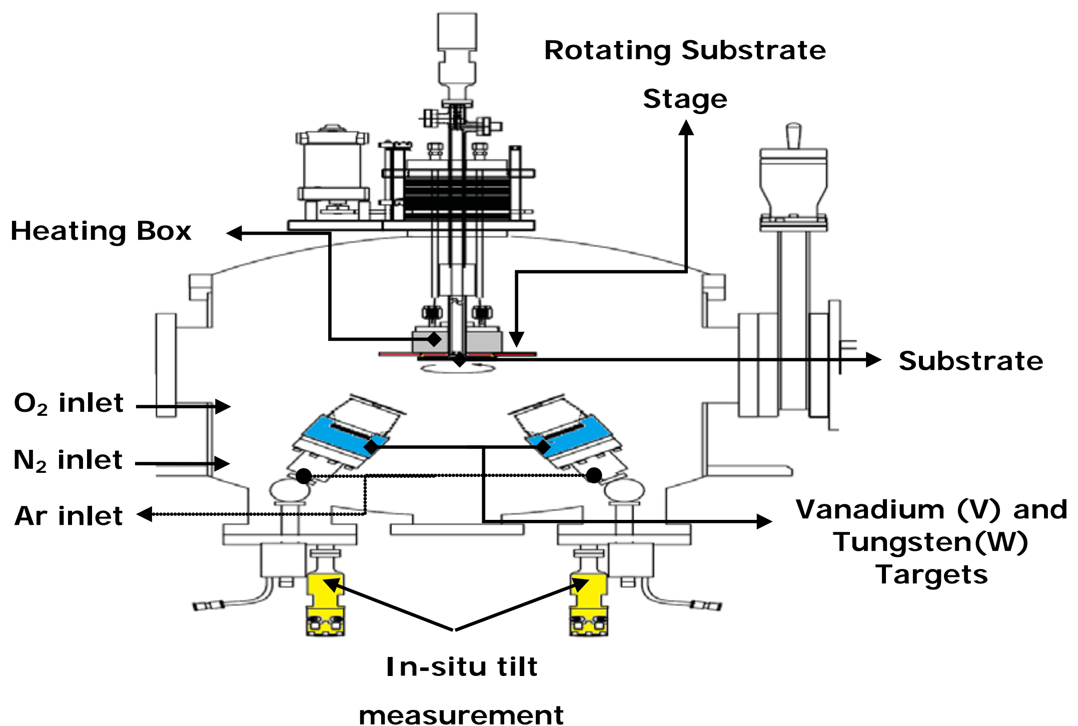

Figure 2.6: The schematic of the AJA sputtering system [45].

This sputtering system is configured as a confocal system. This confocal geometry and the rotating substrate chuck provide a higher thickness uniformity of the deposited material. The uniformity of the deposition

can also be controlled by the individual tilt control mechanism of the targets. The substrate can also be heated up to 500 °C by Ultra Violet lamps in the heater box.

Another important advantage of this system is its co-sputtering property which provides the deposition of two different materials at the same time with the capability of individual timing, power and plasma controls. Ar is supplied the system as the main sputtering gas which generates the plasma and, O_2 and N_2 can also be fed into the system as reactive gases. The flow of these gases can be precisely controlled by independent mass flow controllers. The deposition of VWO relies on the fact of reaction of O_2 molecules with the concurrently and independently sputtered W and V atoms which is called reactive sputtering.

To sum up, the deposition conditions of the material can be controlled by adjusting the applied power, gases flow rates, substrate temperature, pressure, speed of rotation, tilt of the targets, target-substrate distance and deposition time. The limitations of the parameters are given in Table 2.4.

Table 2.4: Limitations of the sputtering system used for VWO deposition.

Parameters		Limitations
Power (Watts)		0-1500
Plasma Current (mA)		2000
Substrate Temp.		500 °C
Gas Flow (sccm)	**Ar**	0-50
	O_2	0-10

It should be noted here that the plasma current strongly determines the applicable power of the system. It has been frequently observed during the studies that a change in a parameter other than the power also may cause a change in the power because of the plasma current limitation.

2.4 Resistive Structures

The resistivity of an active material in bolometer is an important parameter for the resistive structure determination. The resultant resistance of an active material deposited structure can be given as:

$$R = \rho \frac{L}{Wt} \tag{2.1}$$

where R is the resistance, ρ is the resistivity of the active material, L is the length of the resistive path, W is the width of the resistive path and t is the thickness of the active material.

First of all, one should determine the desired resistance values for the bolometric application. At this point the effect of resistance on the NETD should be considered for the optimum resistance determination. A higher resistance gives way to a higher NETD. Accordingly, it makes sense that the resistance should be as low as possible. However, the self-heating effect of the CMOS readout circuitry should be taken into account in this case. Lower resistance values necessitate a lower biasing current which also results in a higher NETD. Therefore, an optimized resistance value that eliminates both of these conditions should be found. A simulation which was done by Ufuk Şenveli in Figure 2.7 shows the dependence of NETD on the resistance considering the self-heating effect [9]. According to the designed readout circuitry simulation, the optimized resistance values are found between 60kΩ and 100kΩ.

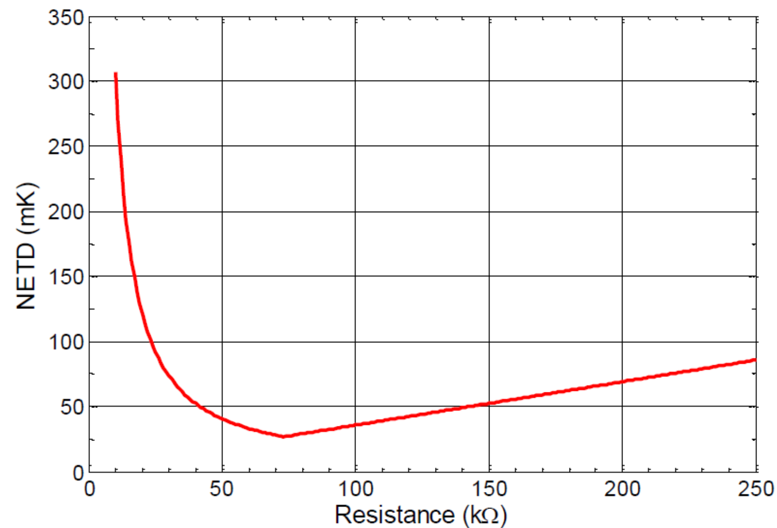

Figure 2.7: Dependence of NETD on resistance considering self-heating affects [9].

As seen from the Equation 2.1, the resistance is described by both resistivity which is an active material property and the geometrical shape of the resistive structure. After the determination of the suitable resistance values, the geometry of the resistive structure should be considered according to the design and the resistivity of the active material. There are mainly three types of resistive structures studied at METU. These are planar type resistors, sandwich-type resistors and enhanced sandwich-type resistors [9].

2.4.1 Planar Type Resistors

The most straightforward method of the resistor fabrication is the planar type resistor. The resistive area is formed by depositing and forming the active area between two electrodes. As the current flow parallel to the substrate surface, the resistance of the material is measured using the pads at each side of the electrodes. Figure 2.8 shows the cross sectional and perspective view of this kind of resistors.

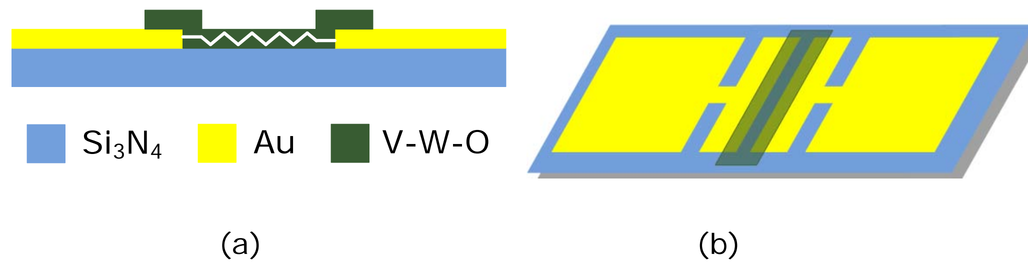

(a) (b)

Figure 2.8: Cross sectional (a) and perspective (b) view of planar type resistors.

Seeing that the resistance is formed between the electrodes, the spacing between each electrode represents the L in Equation 2.1 while the width of the electrode structures is the W in same equation. Thickness (t) is the controllable deposition parameter here. Desired resistance values can be obtained by adjusting the thickness of the active material as a function of deposition time.

Planar type resistors can also be designed in a serpentine formation (finger type) as in Figure 2.9 to increase the W of the electrode for high resistive materials. It is possible to reach relatively low $^{L}/_{W}$ ratios by increasing the number of fingers and decreasing the spacing. However, the fabrication of the finger type structures mainly depends on the critical dimensions of the design and etching capabilities.

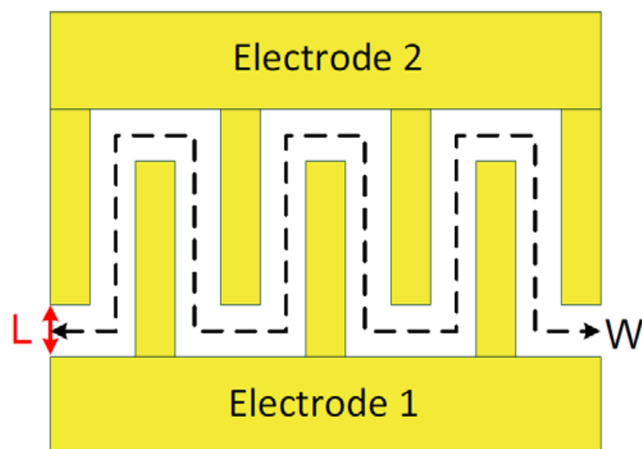

Figure 2.9: Perspective view of serpentinely formed planar structure (finger type) [6].

Although the lithographical sources are adequate for the formation of 0.5 µm structures, the safe minimum features for wet etching is 1.5 µm because of anisotropic etching property of wet etching [9]. The dry etching which is studied in scope of this thesis work is an option for eliminating the drawbacks of wet etching.

There are mainly two downsides of planar type resistors for high resistive materials. Achieving the desired low resistance values is only possible by increasing the number of fingers or depositing the material thicker. However, increasing the number of fingers implies a reduction in the absorbance as a result of larger metallic area and the thicker deposition implies higher thermal capacitance (C_{th}) which gives rise to higher thermal time constant (τ) decreasing the frame rate of the FPA.

Despite these drawbacks, the planar type resistor structure is more preferable than the other resistor structures because of its straightforward fabrication and sufficiency for the bolometric characterization of the VWO material.

Representative fabrication steps of the planar type resistor are shown in Figure 2.10.

2.4.2 Sandwich Type Resistors

Sandwich type resistors are used to decrease the resistance of high resistive materials avoiding deposition of large metallic layer and thicker active material. As seen from the Figure 2.11, the total resistance is the sum of two serially generated resistances.

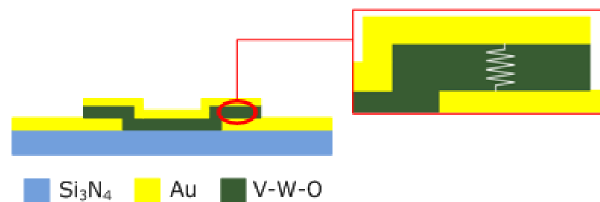

Figure 2.10: The representative view of a sandwich type resistor structure.

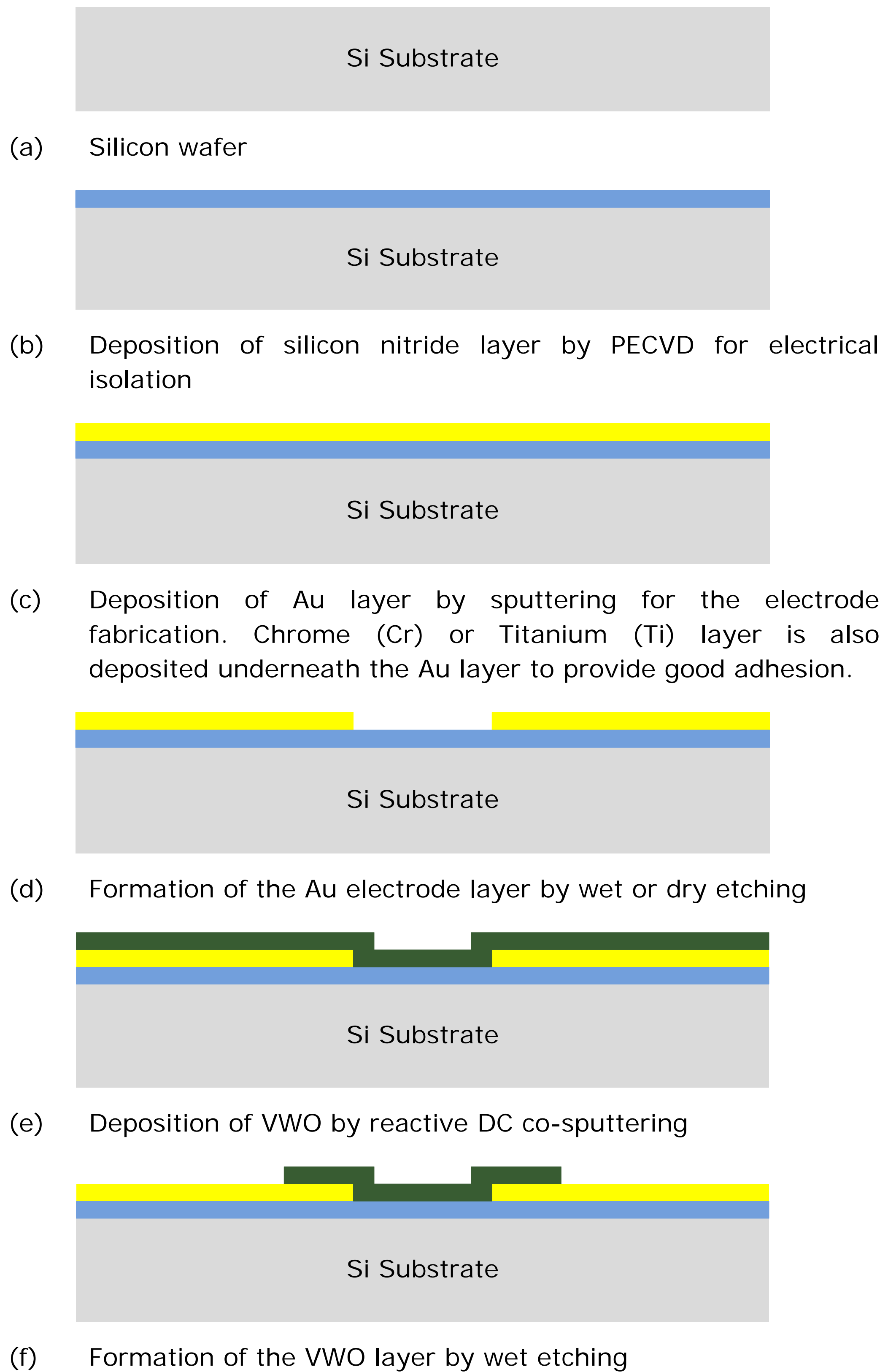

Figure 2.11: Cross sectional view of fabrication steps of the planar type resistor.

The total resistance is determined by the overlapping areas of the electrodes. While the overlapping area defines the area (Wt) in Equation 2.1, the length (L) is determined by the thickness of the VWO material.

Thus, desired resistance values can be achieved by adjusting the thickness of the material. Having lower thickness brings about lower resistance values in a smaller metallic area with respect to the planar type resistors.

This structure requires a full symmetry for uniform resistance values. Overlay errors are very common in lithography, especially in contact aligners but also they result from the significant difference in thermal expansion coefficients of the mask and the substrate [9].

2.4.3 Enhanced Sandwich Type Resistors

This resistor type is developed by Ufuk Şenveli [9] to eliminate the shortcomings of the sandwich type resistors when used together with the YBCO as the active detector material. The previous studies at METU showed that the sandwich type resistors suffer from the high oxygen desorption of YBCO during PECVD nitride deposition at 300 °C which brings about a significant increase in resistance. A general cross-section view of enhanced sandwich type resistor is given in Figure 2.12.

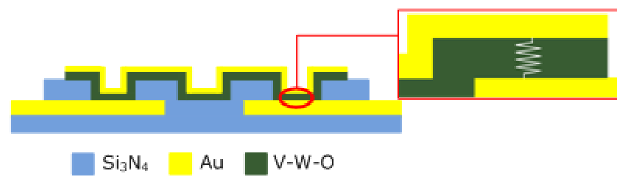

Figure 2.12: Cross sectional view of enhanced sandwich type resistors.

The formation of the resistances in this structure is similar to enhanced type resistors. However, the definition of the electrode area borders by

second nitride deposition prevents the shortcomings resulting from lithographic overlay errors. Furthermore, the deposition of second nitride layer before active material removes the oxygen desorption of YBCO during process.

Enhanced sandwich type resistor structure is the current method in METU-MEMS Research and Applications Center regarding microbolometer studies with YBCO. At the end of the optimization studies, VWO has also been deposited using this structure and the bolometric properties have been investigated and compared with the ones of YBCO within the scope of this thesis.

The fabrication steps of the VWO with enhanced sandwich type resistive structure are shown in Figure 2.13.

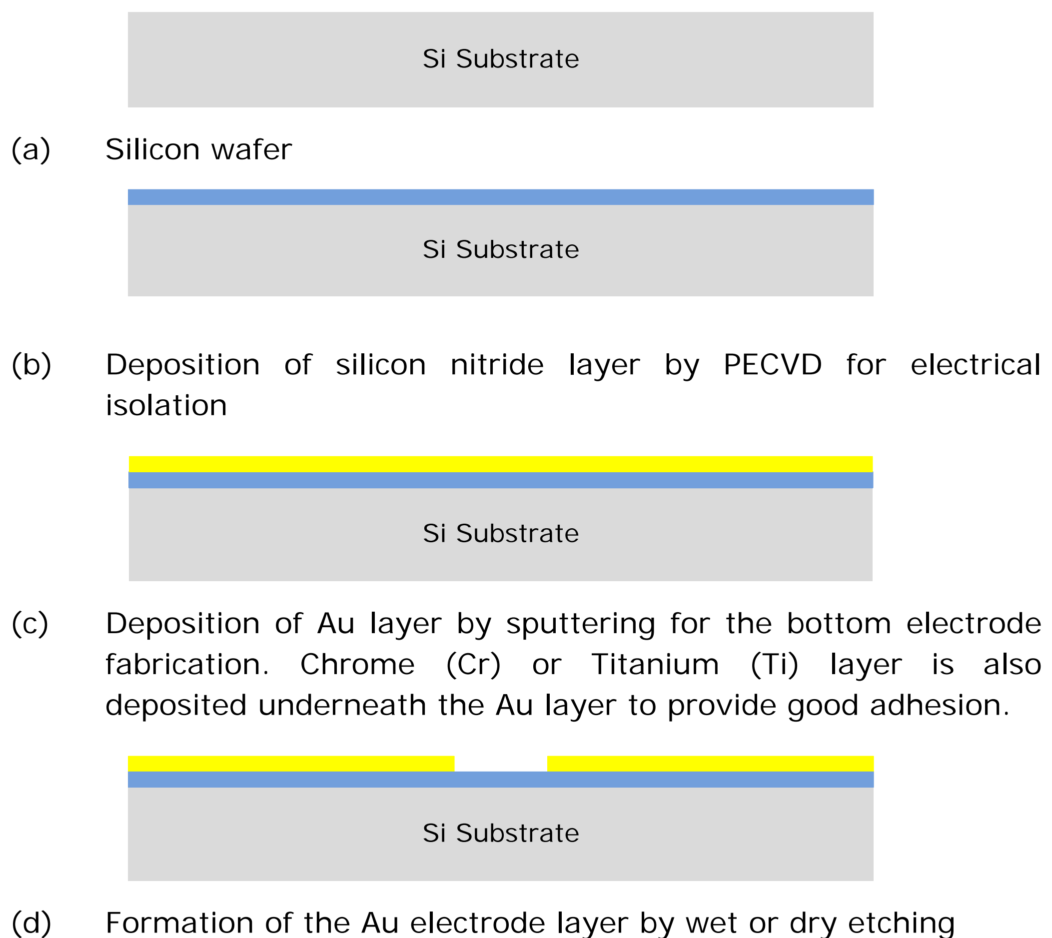

(a) Silicon wafer

(b) Deposition of silicon nitride layer by PECVD for electrical isolation

(c) Deposition of Au layer by sputtering for the bottom electrode fabrication. Chrome (Cr) or Titanium (Ti) layer is also deposited underneath the Au layer to provide good adhesion.

(d) Formation of the Au electrode layer by wet or dry etching

Figure 2.13: Cross sectional view of fabrication steps of the enhanced sandwich type resistors.

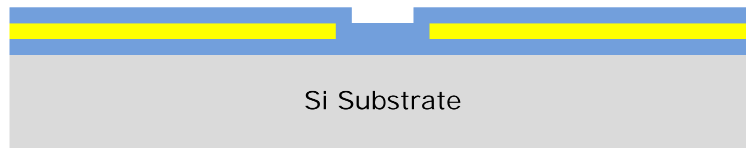

(e) Deposition of second silicon nitride layer by using PECVD for defining the bottom electrode area

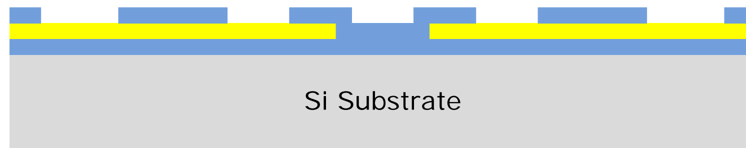

(f) Formation of the second silicon nitride layer by RIE

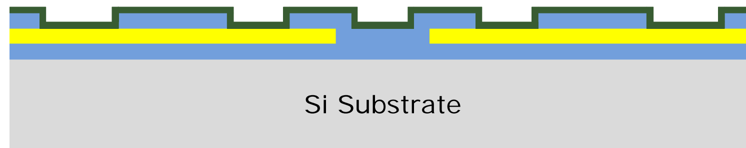

(g) Deposition of VWO by reactive DC co-sputtering

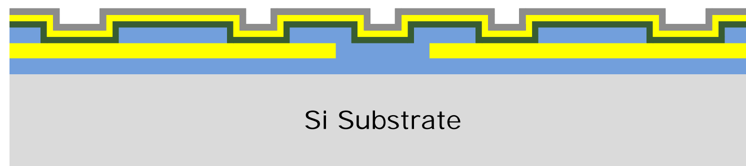

(h) Deposition of Au and Ti layer by sputtering for the bottom electrode fabrication

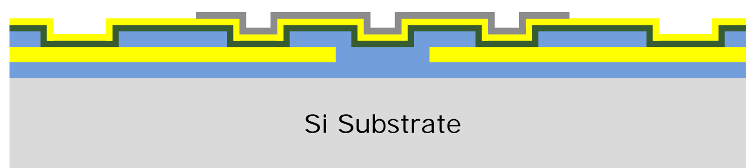

(i) Formation of Ti layer by wet etching

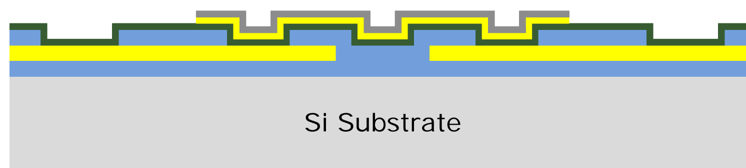

(j) Formation of Au layer by inverse sputtering

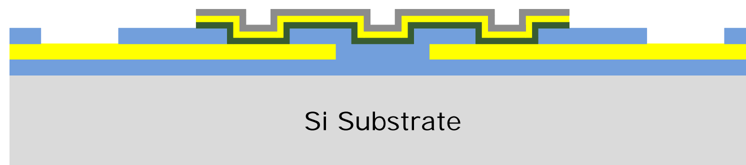

(k) Formation of VWO by wet etching

Figure 2.13: (continued)

2.5 Optimization of Fabrication Steps

Critical fabrication steps for VWO resistor fabrication are formations of electrode layers and the VWO material. This chapter focuses on the etching optimizations of these two layers.

Planar type resistor structure is decided to be the most straightforward and sufficient method for the bolometric characterization of an active detector material. This process is comprised of three deposition and two lithographic steps. The electrodes are deposited by AJA sputtering system using Au as the main electrode material. However, Au layer weakly adheres on the silicon nitride layer. To prevent this and provide a good adhesion of Au, an additional Cr or Ti layer is deposited before Au deposition. Formations of these two layers are conducted in one lithographic step by using dry or wet etching, which is the generally used and optimized etching method in METU for the fabrication of resistors. Wet etching of the Au layers in METU-MEMS Research and Applications center can be done using commercial (TFA) Au etchant by Transene Company or Aqua Regia which is a mixture of H_2O (distilled water), HCL (hydrochloric acid), and HNO_3 (nitric acid) as 7:2:1 ratio.

The latest wet etching optimization studies regarding the etching of Au layer has been conducted by Eren Çanga [11]. His study has showed that the Aqua Regia as 5:2:1 ratio gives better etching properties with less undercut and mousebites. For this reason, Aqua Regia in 5:2:1 ratio is the chosen wet etchant for Au layers of the electrode structures. However, that should be kept in mind that undercutting is an inherent fact of the wet etching. Though the preferred etchant is the optimized recipe for Au etching, it is still not possible to pattern the finger structures less than 1 µm. Figure 2.14 shows the structures etched by using Aqua Regia (5:2:1).

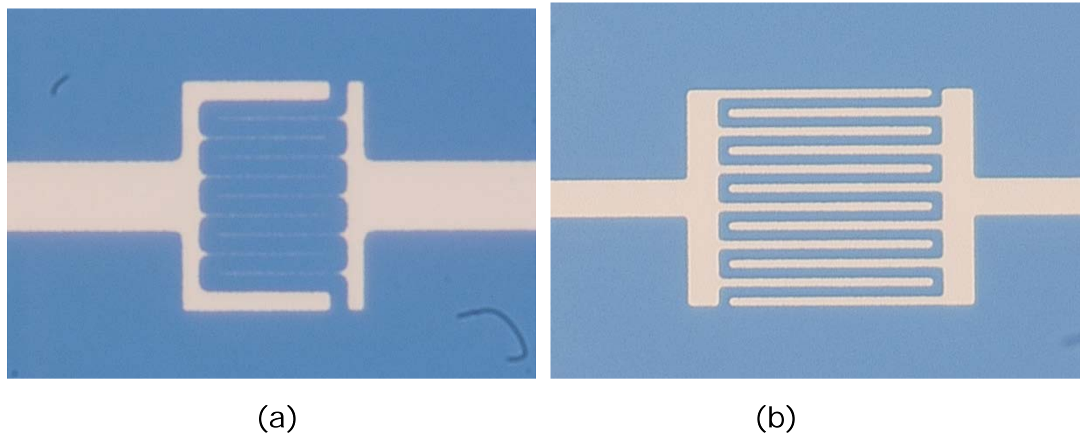

(a) (b)

Figure 2.14: Formation of the electrodes using Aqua Regia (5:2:1) is shown for finger structures with both 0.7 µm (a) and 1.5 µm (b) finger thickness.

Dry etching method can be thought as a healing option for the undercutting problem. Use of MRIE (metal reactive ion etching) method is optimized for the etching of 50 nm thick Au layers during the electrode fabrication studies. The biggest problem with the MRIE has been the adhesion of sputtered Au particles to the sidewalls of the structures. This problem is solved by Akın Aydemir by using a thinner photo resist, S1805, with an additional very thin Ti layer (~15 nm) to prevent adhesion [46]. The etching results of the 0.5 µm finger structures using MRIE can be seen in Figure 2.15.

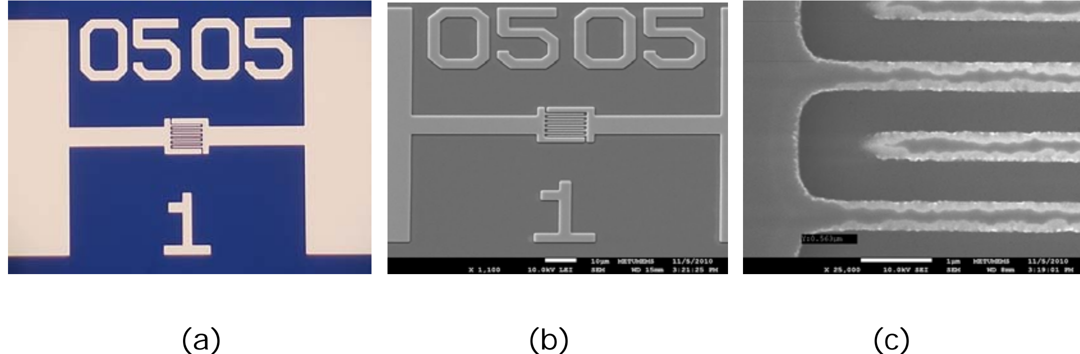

(a) (b) (c)

Figure 2.15: HIROX (a) and SEM (b, c) photos of Au etching of 0.5 µm structures. The thinning at the edges in (c) is a result of pyramid-like shaping of the S1805 during hardbaking.

Following the MRIE etching of the Au layer, EKC 265 solution is used to remove the adherent Au particles from the structures and the sample is exposed to oxygen plasma for the cleaning and photo resist stripping process. Because the oxygen plasma is also used for the Cr etching, the pre-deposited Cr layer providing adhesion to Au layer is also etched at this step. If Ti is used instead of Cr, Ti etching can be applied before oxygen plasma with a mixture of H_2O, H_2O_2 (hydrogen peroxide), HF (hydrofluoric acid) as 400:1:1 ratio.

The etching trials regarding the VWO have been conducted following the determination of initial deposition conditions given in Table 2.5.

Table 2.5: Deposition condition of the sample used for etching trials.

Deposition Condition	
V Power (W)	655
W Power (W)	32
Ar Flow (sccm)	30
O_2 Flow (sccm)	5
Base Pressure (mTorr)	$< 10^{-7}$
Pressure (mTorr)	3
Substrate Temperature (°C)	Room Temperature
Deposition Time (sec)	1000

Though the preferred etching method is dry etching by use of CF_4 (tetrafluoromethane), wet etching has been decided as the first option to prevent any contamination which can be resulted from this new material. The etching trials have been conducted by taking the selectivity of the etchant for pre-deposited layers into account. H_2O_2 has become the first tried solution because of its known etching capability

for both the VO_x [44] and W. As a result of these trials, it has been observed that the mixture of H_2O and H_2O_2 as 31:1 ratio successfully etches the VWO providing a reasonable undercut and high selectivity. Figure 2.16 shows a picture of the sample after VWO etching in a diluted hydrogen peroxide.

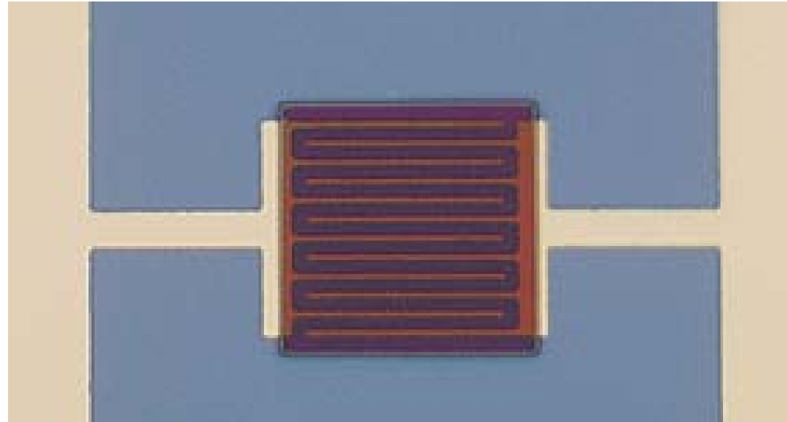

Figure 2.16: A VWO resistor which has been etched in diluted hydrogen peroxide at 31:1 ratio. Because the photoresist is not stripped, the undercut can be easily seen at the edges of the active material layer.

The etching trials of VWO using diluted HCL, H_2SO_4 (sulfuric acid), HNO_3 (nitric acid) have not showed any observable etching properties in five minutes for 225 nm-sample deposited in pre-mentioned conditions.

CHAPTER 3

DEPOSITION AND CHARACTERIZATION

This chapter discusses the deposition process of VWO. Section 3.1 is mainly about the preliminary works which are done before the deposition of the VWO. It explains the optimization of the targets before deposition process, and reveals how the initial sputtering conditions are determined while making a short introduction concerning the mask used in resistor fabrication. Section 3.2 explains the characterization methods used for resistivity, TCR and noise measurements after the determination of the reference VWO deposition recipe which shows promising bolometric properties. NETD calculation for the reference recipe is also performed in this section and the parameters used for NETD calculations conducted within this study are revealed.

3.1 Preliminary Works

Before initializing the deposition studies, a few prerequisites should be determined. These prerequisites for the fabrication of resistive thin film are; the optimization of the deposition uniformity of targets that are planned to be used during fabrication, the determination of the sputtering parameters, the determination and the analysis of the mask set.

3.1.1 Optimization of Thickness Uniformity

Optimization of thickness uniformity is a very salient issue for resistance measurements. It is highly related to the resistance non-uniformity in FPA and its proper operation. What is more, a low non-uniformity ends in a uniform etching which gives similar undercuts in the end and increases the yield.

The non-uniformity optimizations for a co-sputtering process should be carried out separately for each of the target. So as to measure the thickness of the deposited film, a step height should be formed by applying lithography and etching processes to the deposited film. Both of V and W targets are deposited in the same sputtering conditions without any oxygen flow but at different deposition powers. Deposited vanadium metal is etched in diluted HNO_3 and tungsten metal is etched in diluted H_2O_2 solutions. The thickness measurements of the samples are performed with Veeco Dektak 8 stylus profiler. Thickness of each sample is measured at 9 different points along 6″ wafer according to the template given in Figure 3.1.

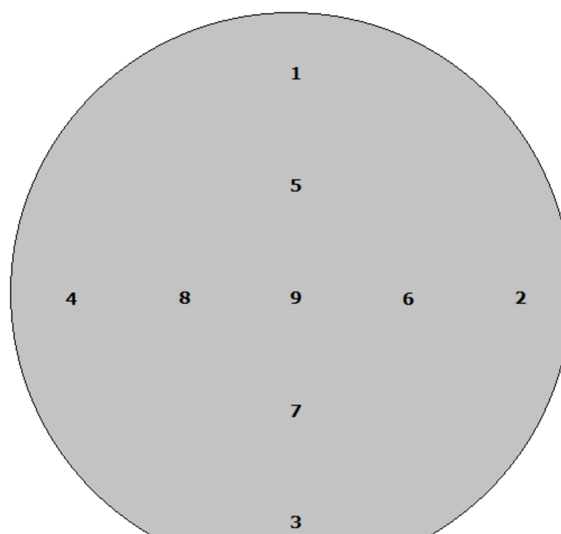

Figure 3.1: The thickness measurements are conducted at the numbered points as shown on the template.

Non-uniformity of the samples is calculated by using the formula given below;

$$U(\%) = \frac{t_{max} - t_{min}}{2t_{ave}} x100 \qquad (3.1)$$

where U is the non-uniformity, t_{max} is the maximum measured thickness, t_{min} is the minimum measured thickness, t_{ave} is the average thicknesses measured from 9 points.

The non-uniformity of both targets is controlled by in-situ tilt adjustment mechanism of AJA sputtering system. The measurement results are shown in Table 3.1.

Table 3.1: Thickness uniformity measurements of the vanadium and tungsten samples (vanadium samples are coded with V while tungsten samples are coded with W).

Sample	Power (W)	Ar flow (sccm)	Pressure (mTorr)	Tilt	Non-uniformity (%)
V1	580	30	3	19	2.56
V2	580	30	3	19.5	1.77
V3	580	30	3	**19.4**	**1.4**
W1	75	30	3	20	2.61
W2	75	30	3	20.2	2.05
W3	75	30	3	**20.3**	**1.5**
W4	75	30	3	20.5	6.4

3.1.2 Determination of Process Conditions

Initial deposition parameters for AJA sputtering system have been conducted using the integrated thickness measurement system, MCM-160 (product of McVac), including quartz crystal sensors. It has been

aimed to measure the deposition rate of V, VO_2, V_2O_5 and W under different deposition conditions such as deposition power, pressure and O_2/Ar ratio as the reactive and the sputtering gases. These rough measurements can be seen in Figure 3.2.

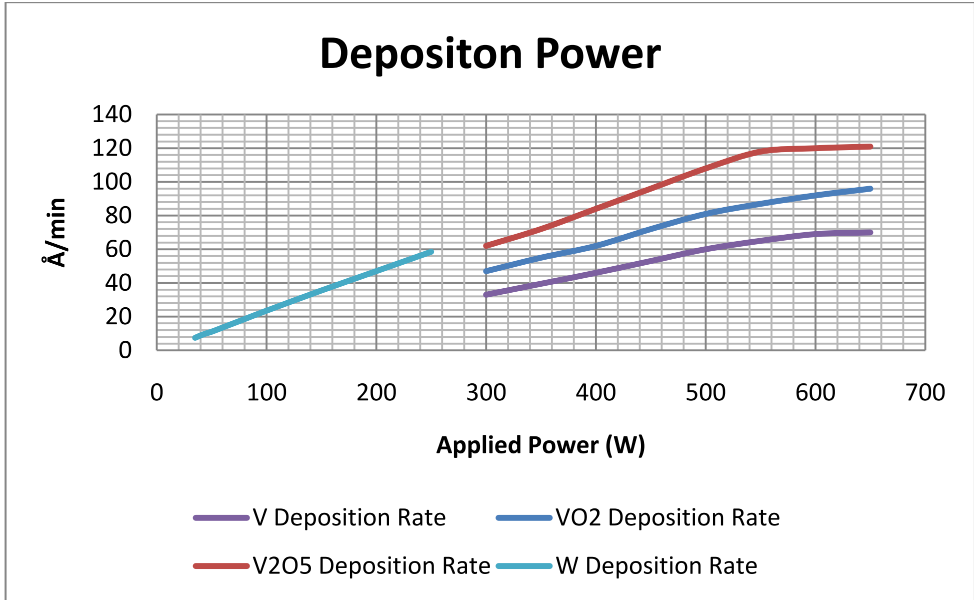

(a) @ 3mTorr pressure, 45 sccm Ar and 2 sccm O_2 flow

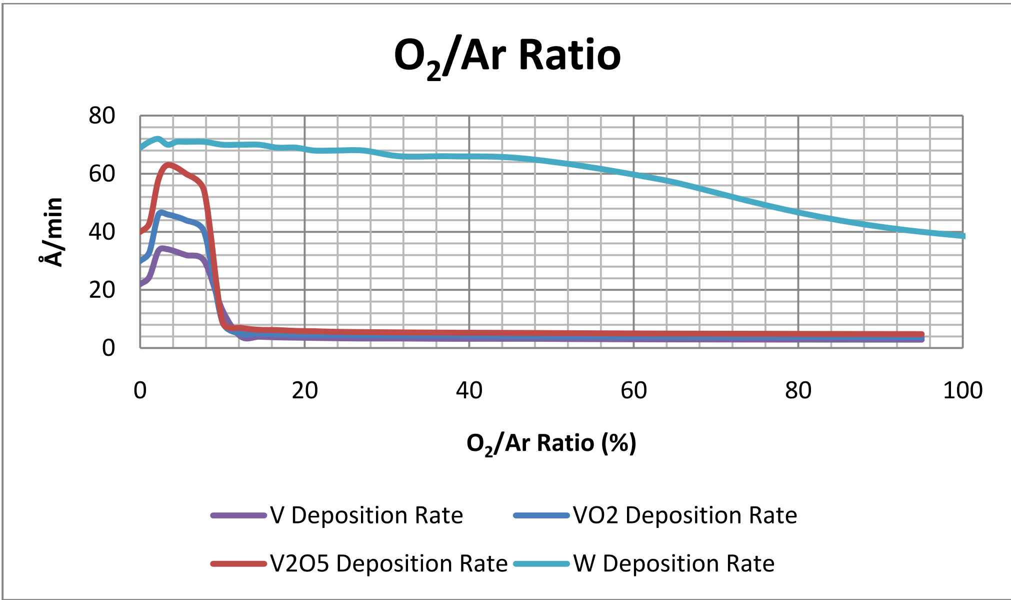

(b) @ 5mTorr pressure and 300 W power for both V and W targets

Figure 3.2: Deposition rate measurements of V, VO_2, V_2O_5 and W in different deposition power (a), O_2/Ar flow (b) and working pressure (c) conditions.

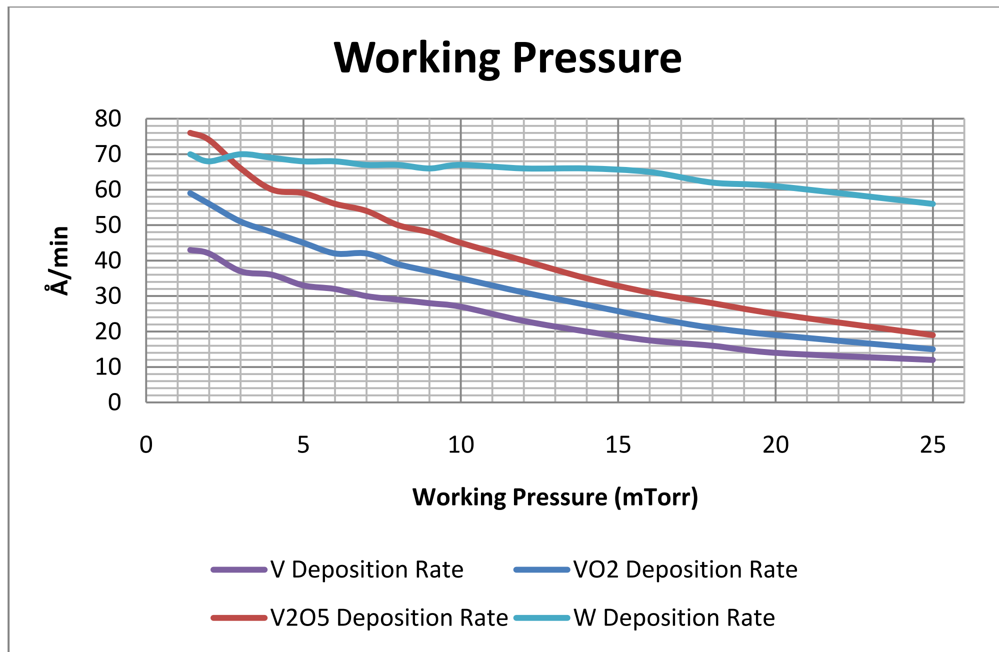

(c) @ 300 W power for both V and W targets, 45 sccm Ar flow and 2 sccm O_2 flow

Figure 3.2: (continued)

When all the parameters are kept constant except for the deposition power, the sputtering of W target is much easier at lower DC powers. The deposition rate of a 40 Å/min can be reached at ~170 Watt while it is ~360 Watt in V case. Because the best bolometric results are taken when the W concentration is below 10% according to Moon's studies [37], this result informs that the power of V should be adjusted according to W power and it should be kept at low levels.

The result of O_2/Ar ratio shows that the formation of VO_x molecules increases when the O_2/Ar ratio is below 10%. Hence, a higher deposition ratio with V and its components can be acquired by keeping O_2 flow below or equal to 10% of Ar flow.

The result related to the pressure effect indicates that the deposition rate of V is much more affected when compared to W's and one can

acquire a higher V deposition rate by applying a lower working pressure to the sputtering system.

It has been realized during these studies that, the plasma current which cannot be externally controlled is highly related to the above mentioned deposition parameters. It limits the power when it reaches 2000 mA even though the upper limit of the system is 1500 Watts. For this reason, the deposition power of the V target, relatively higher than the W target, has been determined by taking this fact into account. Table 3.2 shows how the deposition parameters limit the power of V target as a result of the plasma current limitation at 2000 mA.

Table 3.2: Limitation of the actual V power as a result of the plasma current limitation (the changes are marked in **bold** characters)

Sample	Ar Flow (sccm)	O_2 flow (sccm)	Pressure (mTorr)	Set Power (W)	Actual Power (W)
1	45	-	5	610	610
2	45	-	5	**660**	643
3	45	-	5	**710**	643
4	45	-	**1,5**	710	714
5	30	5	3	655	655
6	30	**3**	3	655	624
7	30	**2**	3	655	610

Deposition studies regarding the fabrication of VWO are initialized in view of these measurements. It should be mentioned here that it is very significant to pre-sputter the V and W in Ar atmosphere in order to ensure oxide free metallic surface. Hence, the pre-sputtering of both targets for 5 minutes at high target power is conducted prior to all depositions.

A couple of recipes which show promising bolometric properties and are capable of being used as a reference have been determined during numerous deposition trials. However, the recipe shown in Table 3.3 has been decided on by taking the plasma current limitation and reproducibility into consideration. In further studies, influence of V power is examined in Table 4.1, influence of W power in Table 4.3, influence of oxygen flow in Table 4.5, influence of Ar flow in Table 4.7, influence of working pressure in Table 4.9, influence of hot deposition in Table 4.11, influence of post-annealing in Section 4.1.7 and influence of oxygen plasma in Section 4.1.8.

Table 3.3: Determined recipe which is taken as a reference for further studies.

Deposition Conditions		Properties	
V Power (W)	554	Resistivity (Ω-cm)	73
W Power (W)	35	TCR (%/K)	-3.03
Ar Flow (sccm)	30	Noise corner frequency (kHz)	1.4
O_2 Flow (sccm)	3	Thickness non-uniformity (%)	3.7
Base Pressure (mTorr)	$< 10^{-7}$	Resistance non-uniformity (%)	23
Pressure (mTorr)	3		
Substrate Temperature (C)	RT		

3.1.3 Determination of the Mask Set

The mask set in resistor fabrication is important for the determination of the electrode structures. Because the planar type resistor structures imply a straightforward fabrication in two steps and their sufficiency for bolometric characterization, a 6″ mask-set previously fabricated in

METU-MEMS Research and Applications Center is used for the fabrication of VWO resistors. This mask-set consists of numerous planar resistors structures with finger and non-finger electrodes as seen in Figure 3.3. This smorgasbord provides a large scale $L/_W$ ratio between 0.003 to 0.1 which results in a variety of resistance values at the end of the fabrication. Before VWO deposition studies, the layout of the selected mask has been inspected and all $L/_W$ ratios which determine the resistance have been calculated.

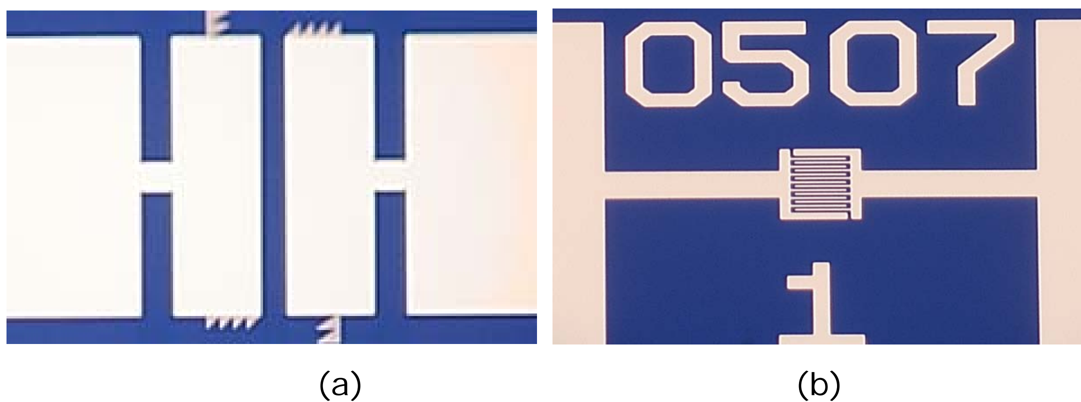

Figure 3.3: Electrode structures used in the selected mask-set for VWO fabrication and characterization.

3.2 Bolometric Characterization

NETD is the most significant performance parameter for microbolometers and defines the smallest sensible temperature variation of a bolometric array. Resistivity, TCR and noise behavior are the most important active material properties that define the NETD which is always desired to be at low levels. The measurement methods about these parameters are clarified in the following sub-sections including the measurement results of the reference recipe given in Table 3.3.

3.2.1 Resistivity Measurements

Resistivity of a material is the function of the sheet resistance and this relation can be explained as:

$$\rho = R_s \, x \, t \qquad (3.2)$$

where ρ is the resistivity, R_s is the sheet resistance and t is the thickness of the resistive structure.

The sheet resistances of VWO samples fabricated within the scope of this thesis have been measured using 4 point-probe instruments available in METU MEMS Research and Applications Center. The VWO layer, sheet resistance of which is measured using 4 point-probe instruments, has been fabricated on a 0.2 μm silicon nitride layer. However, the measurement results have been found to be inconsistent and very far from the expected values most probably due to the contact problem between the VWO and the probes. Thus, the resistivities of the fabricated VWO samples are determined by hand-calculation using the formula given in below:

$$\rho = \frac{RWt}{L} \qquad (3.3)$$

where ρ is the resistivity, R is the measured resistance, W is the width of the resistive path, L is the length of the resistive path, and t is the thickness of the deposited VWO layer. Since the undercutting is in the nature of wet etching, the length and width of the resistive paths are measured after each etching process in order to make a precise calculation.

The resistivity uniformity across the wafer is another important issue to increase the yield and to operate the FPA of the detector properly. Throughout the studies, it has been observed that there is a variation of the resistivities across the wafer as a result of compositional inequalities. Hence, this issue is also examined during the studies and

the resistivity non-uniformity of the VWO samples are measured by calculating the resistivity values of 5 different regions (L1, L5, L9, R9 and W9 shown in Figure 3.4).

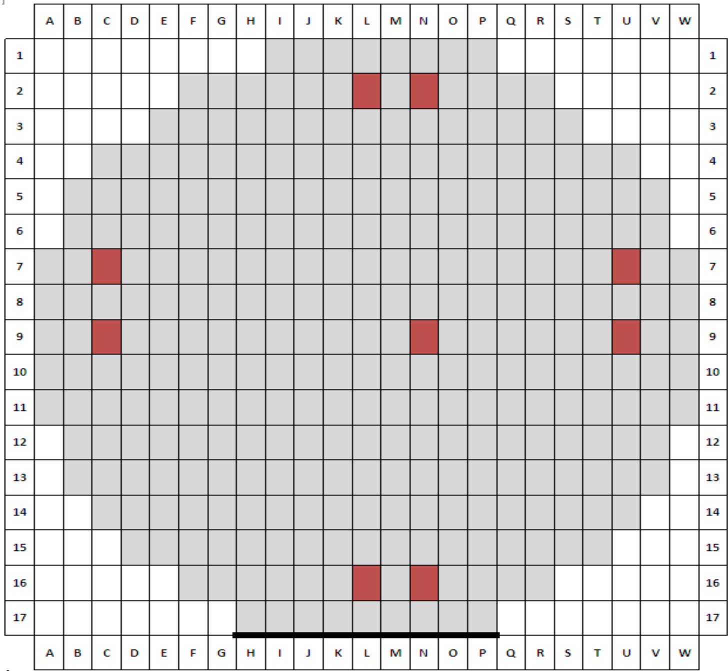

Figure 3.4: The layout of the 6″ wafer used during bolometric characterization studies of VWO film. The wine colored regions consist of the alignment marks for ASML PAS 5500/200B Stepper lithography system. Dies L1, L5, L9, R9 and W9 are used for the resistivity measurements and for the determination of thickness and resistivity non-uniformity, while dies L3 and L7 are used for TCR and Noise measurements of deposited VWO samples.

The resistivity non-uniformity of the reference recipe given in Table 3.4 is found as 23% which is very high. This high non-uniformity improved to 1% during the studies which are discussed in Chapter 4. Table 3.4 indicates the resistivity measurement results of the reference recipe. During this thesis study, the resistivity value of die L5 for each wafer is used for resistivity comparison.

Table 3.4: Resistivity measurements of the reference recipe given in Table 3.3.

Die	L1	L5	L9	R9	W9
ρ (Ω-cm)	57	73	89	72	56

3.2.2 TCR Measurements

TCR measurements of this study are conducted in a Tenney environmental chamber in which temperature and humidity are controllable. Though the temperature of the chamber can be externally controlled, in order to make a precise measurement, a temperature sensor AD590 is packaged together with the sample on the same alumina base as seen in Figure 3.5.

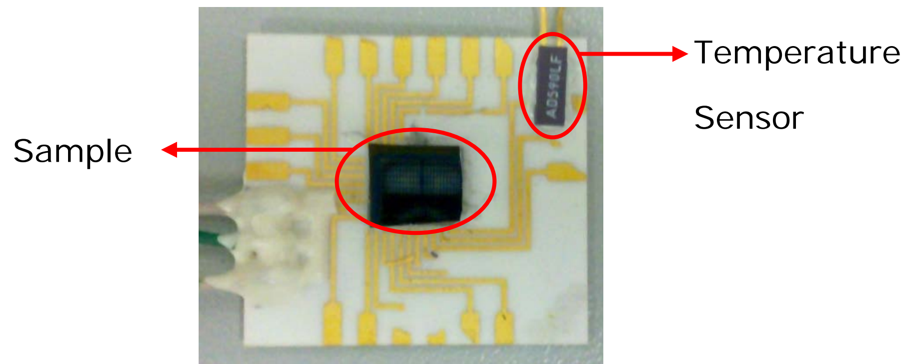

Figure 3.5: A picture of the TCR measurement package.

AD590 temperature sensor is biased at a constant voltage of 5 V and the current is read. The read value from the multi-meter is temperature in Kelvin. The resistor structure is biased at the constant current of 10 μA and the voltage variation is read during the heating of the chamber from 15 to 35 °C. The received output data that are the current of the AD590 temperature sensor and the voltage of the resistor are

read by HP Vee software. The obtained data showing the resistance change as a function of temperature are fitted to a polynomial curve the derivation of which gives the dR/dT component of the Equation 1.4.

The measurement of the reference recipe shows a relatively high TCR of -3.03 %/K (L3) at 23 °C as seen in Figure 3.6. This TCR is obtained from the die L3 and L7 also shows almost equal TCR at -3.02 %/K. During this thesis study, the TCR measured from die L3 for each recipe and wafer is used for TCR comparison.

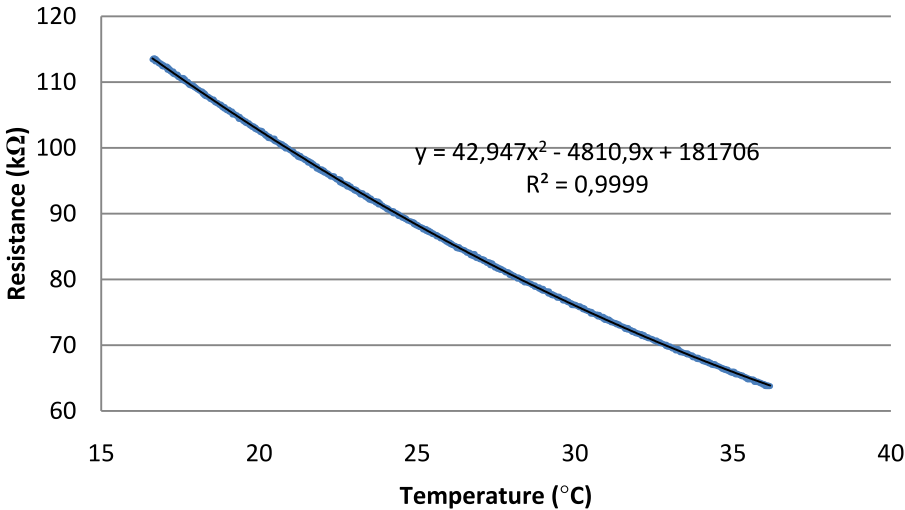

(a)

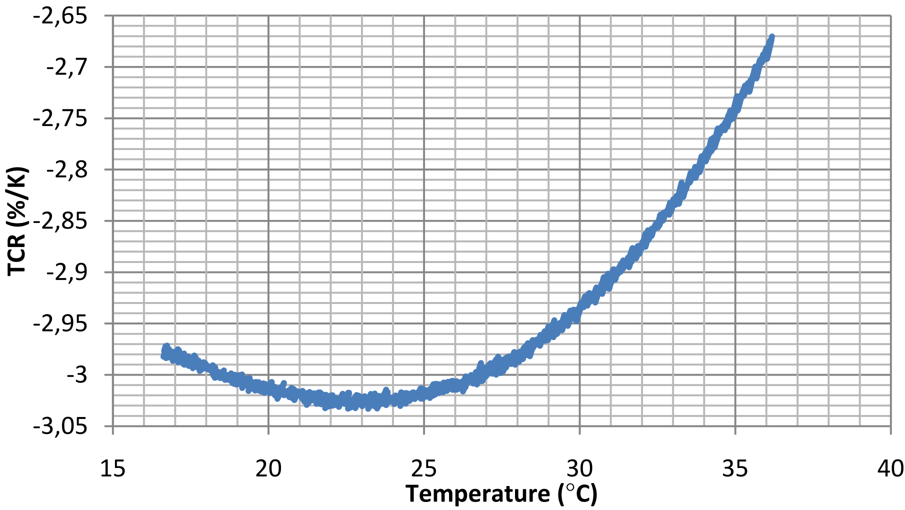

(b)

Figure 3.6: The measured resistance vs. temperature (a) and TCR vs. temperature curve of the reference recipe.

TCR measurement of the reference recipe also demonstrates that the resistance change with respect to temperature is fitted to Arrhenius relation given as below:

$$R = R_0 e^{(-E_a/kT)} \tag{3.4}$$

where R is the resistance, R_0 is the pre-exponential factor, E_a is the activation energy, k is the Boltzmann constant, T is the temperature in K. This compatibility can be seen in Figure 3.7 and the figure shows that the conduction of the VWO is a thermally activated process [47].

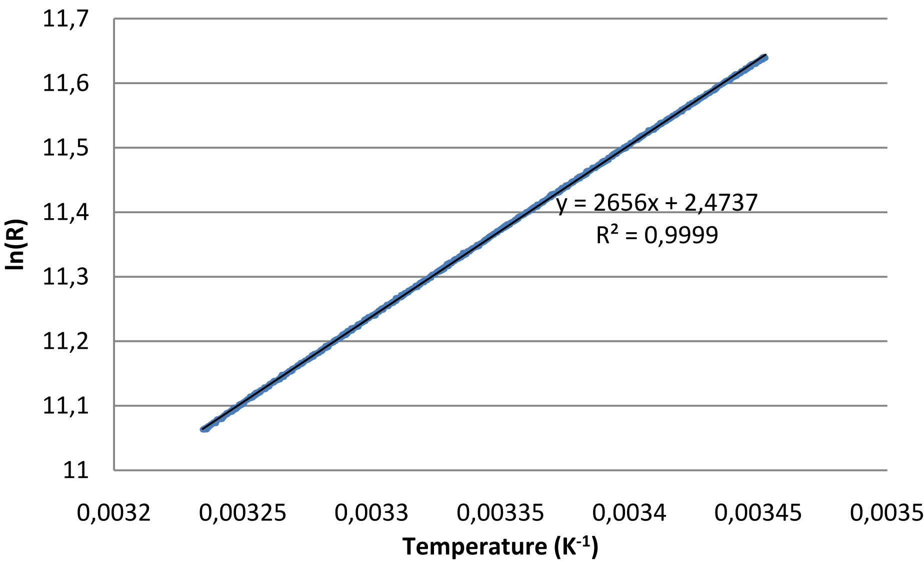

Figure 3.7: Arrhenius plot of resistance vs. temperature is linear which shows the resistance change is a thermally activated process. The activation energy is calculated as 0.229 eV.

3.2.3 Noise Measurements

The flicker noise and the Johnson noise are two major noise sources in resistor structures. Flicker noise is a frequency dependent noise source and appears under biased conditions. It dominates the total noise of the system at low frequencies. On the other hand, as the frequency

increases it settles on the floor which is equal to Johnson noise. Johnson noise in resistor structure always exists under bias or no bias conditions. The frequency where the flicker noise is equal to Johnson noise or where the total noise is twice as much as the Johnson noise is called corner frequency. This frequency is the point where the flicker noise commences to lose its dominance.

The noise measurements of the fabricated VWO resistors are conducted using a charge transimpedance amplifier (CTIA) inside the nested Faraday Cage and an Agilent Dynamic Signal Analyzer. Figure 3.8 displays a simplified schematic of the noise measurement circuitry.

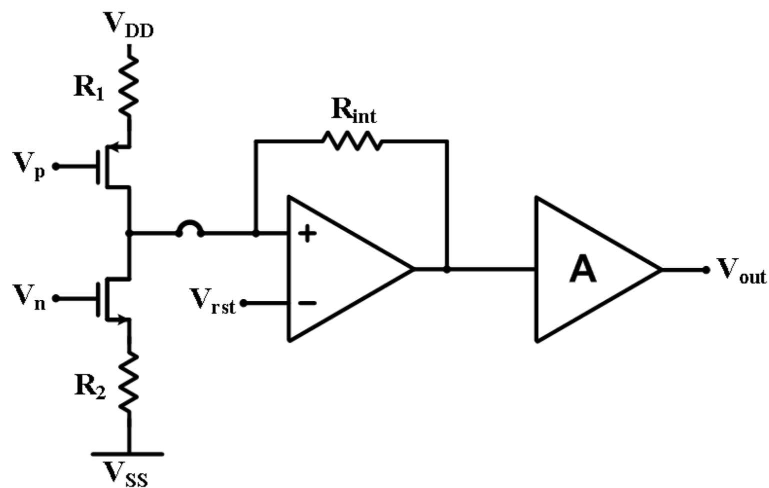

Figure 3.8: The schematic of the noise measurement circuitry.

It consists of two resistors which are fabricated out of VWO, transistors of the CTIA stage and amplifiers. The fabricated resistors which are marked as R_1 and R_2 in the test circuit represent the pixel resistor in the FPA and the reference resistor respectively. For a proper operation resistance of R_1 and R_2 should be the same or as close as possible. V_p and V_n are used to adjust the current passing through the resistors and they are adjusted in such a way that the current passing through both resistors are equal. Eventually, the current at the input amplifiers is just

the noise current and this is converted to voltage as it is amplified at the output.

During the noise measurements of VWO samples, the current of the resistors is adjusted according to the constant current of 20 μA. The noise measurement result of the reference recipe is given in Figure 3.9 and Table 3.5. The NETD is calculated for the reference and following recipes in Chapter 4 by using constant parameters given in Table 3.6. This and further noise measurement results given in Chapter 4 generally exhibit lower noise behavior of VWO when compared to the other studies in which YBCO [6] and VO_x [44] are used in METU with planar type resistor structures. The noise measurements are conducted with dies L3 and L7 and during the thesis study the noised measured from die L3 is used for comparison with other recipes.

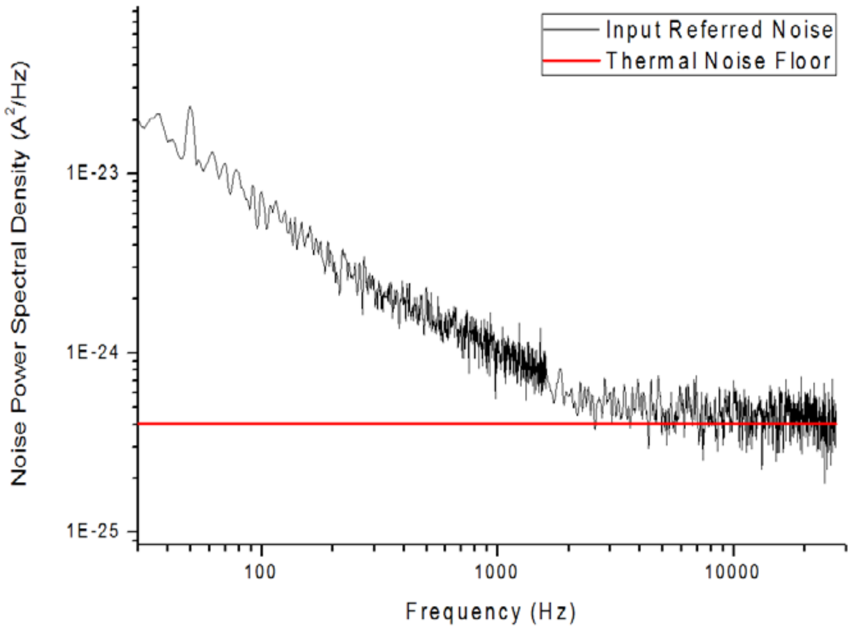

Figure 3.9: Noise measurement result of the reference recipe.

Table 3.5: Summary of the measurements for the reference recipe given in Table 3.3. The NETD is calculated for the reference and the following recipes in Chapter 4 by using constant parameters given in Table 3.7.

Resistance (kΩ)	82
Theoretical Noise Floor (Johnson noise)(A^2/Hz)	4.04×10^{-25}
Measured Noise/Theoretical noise @ 8.4 kHz	1.48
Flicker noise corner frequency (kHz)	1.4
TCR (%/K)	-3,03
NETD (mK)	46

Tablo 3.6: Parameters used for NETD calculation

Parameters	Value
Array Size	384x288
Pixel Pitch(μm)	35
Fill Factor (%)	44
Absorptance (%)	50
Thermal Conductance (W/K)	4×10^{-8}
Time Constant (ms)	15
Integration Time (μs)	60

CHAPTER 4

EXPERIMENTAL RESULTS AND STRUCTURAL CHARACTERIZATION

This chapter reveals all the results taken throughout this thesis study. Section 4.1 discusses the different sputtering conditions for VWO deposition. The bolometric characterization of the deposited films which includes uniformity, resistivity, TCR and noise measurements is examined in detail. Section 4.2 reveals the attained optimized recipe and makes a brief comparison between VWO and YBCO. Section 4.3 explains the structural characterization methods including obtained results.

4.1 Analysis of Bolometric Properties in Different Deposition Conditions

The fabrication of the VWO active material which is the subject of this thesis study is conducted by using reactive DC magnetron co-sputtering method. Controllable parameters of this method are DC power applied to both V and W targets, the atmospheric conditions such as pressure and flow of gases, and the temperature of the substrate. Literary sources inform that the substrate temperature for deposition of VO_x material is generally in the temperature range of 200-300 °C [44]. On the whole, the studies regarding fabrication of VWO are also performed at high deposition or at post-annealing temperatures [34, 48, 49].

Post-annealing is a method following the deposition of the material to change the stoichiometric structure into the desired form by using the heat-effect and reaction of the samples with reactive gases.

All of these deposition parameters and post-deposition processes are analyzed in scope of VWO studies by taking the recipe given in Table 3.3 as a reference and the results are present in subsections below including the thickness and resistivity uniformity for 6″ wafer.

4.1.1 Influence of Vanadium Power

The DC power of the vanadium target is set to four different levels while keeping the other parameters constant, and the changes in the bolometric properties are observed. The applied power levels for V target are set to 504 W, 533 W, 554 W and 624 W which are coded from S1 to S4 respectively. The power levels above 624 W cannot be applied on account of plasma current limitation as discussed in Chapter 3. The applied recipes for this study are shown in Table 4.1 and it indicates that the highest V power results in a more uniform deposition in terms of resistivity.

The results of resistivity measurements are shown in Figure 4.1 by taking the measured resistivity at the die L5 as a reference. It can be clearly seen here that the resistivity of the fabricated VWO thin film decreases as the applied power to V target increases. TCR measurements are conducted for the samples S1, S3 and S4. The measurement results of S3 and S4 are almost the same, and the TCR of the deposited film at 504 W gives higher TCR result at the expense of resistivity. Noise measurements are also performed using S1, S3 and S4 and the results of the samples are given in Figure 4.3 and all measurements are summarized in Table 4.2. According to the calculated corner frequencies by taking the die L3 as a reference, the deposition case at 504 W exhibits relatively low noise behavior when compared to the others.

Table 4.1: Recipes of the samples used to investigate the influence of vanadium power on bolometric properties.

	S1	S2	S3(ref)	S4
V Power (W)	**504**	**533**	**554**	**624**
W Power (W)	35	35	35	35
Ar flow (sccm)	30	30	30	30
O_2 flow (sccm)	3	3	3	3
Pressure (mTorr)	3	3	3	3
Deposition Temperature (°C)	RT	RT	RT	RT
Thickness Non-uniformity (%)	1	3.1	3.7	2.2
Resistivity Non-uniformity (%)	24	21	23	14

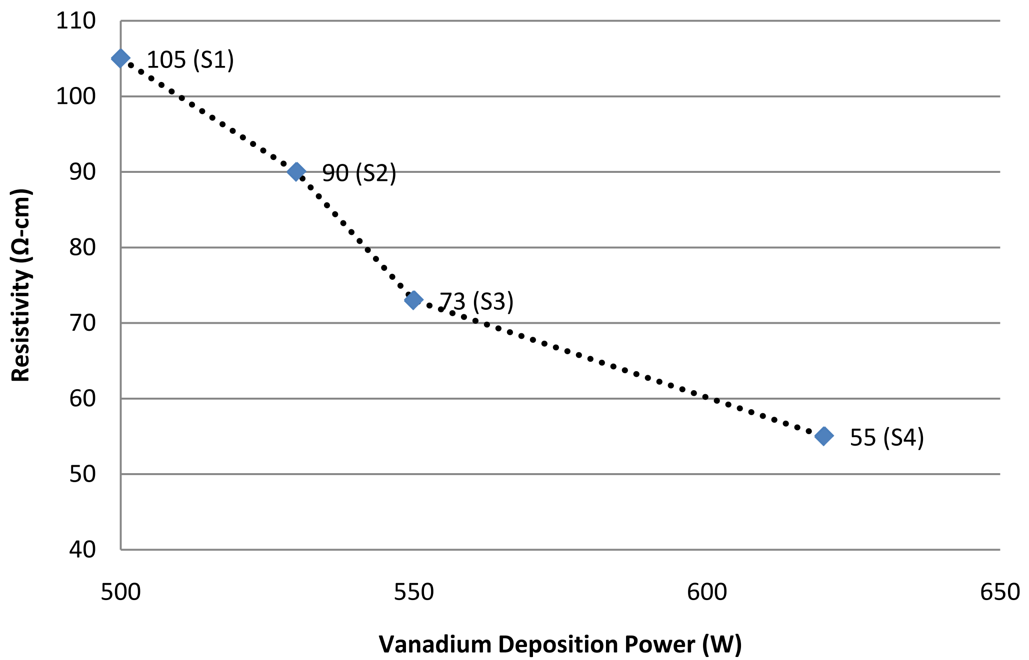

Figure 4.1: Resistivities of the samples deposited at different vanadium power levels.

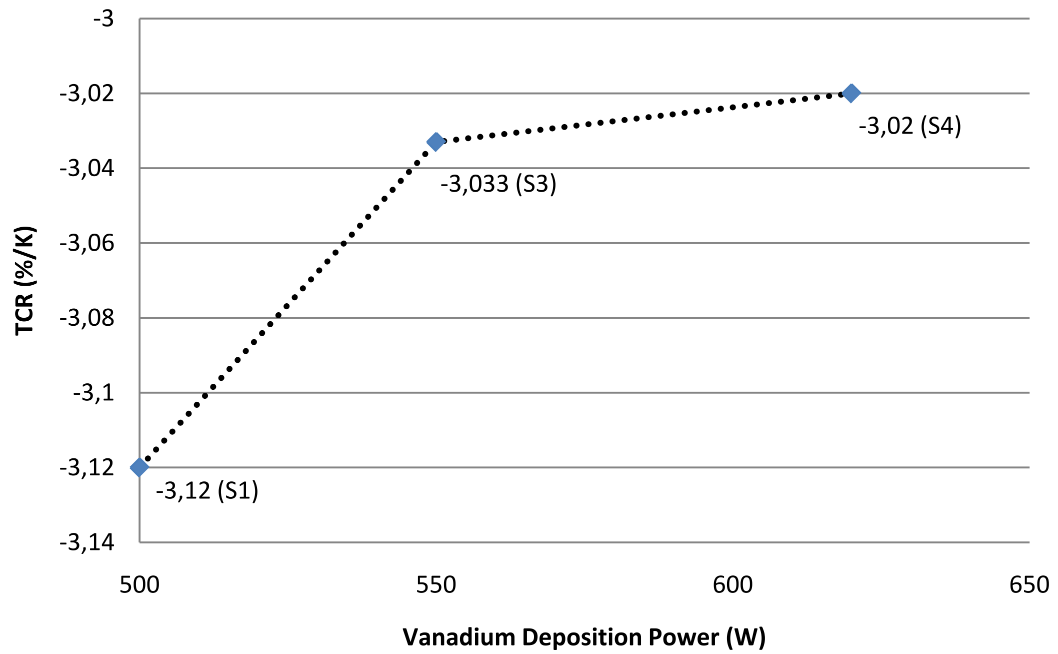

Figure 4.2: TCR measurements of the samples deposited at different vanadium power levels.

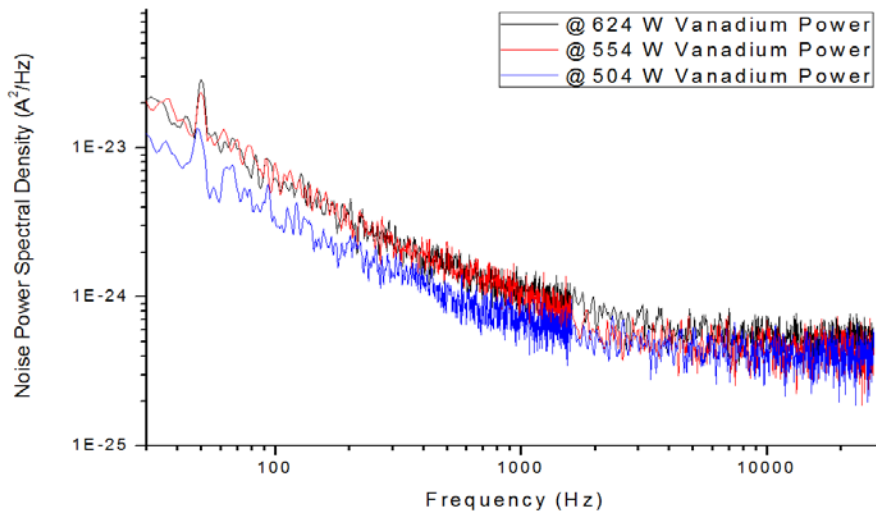

Figure 4.3: Noise behavior of the samples deposited at different vanadium power levels.

Table 4 2: Summary of the measurements at different vanadium power levels.

	@624 W	@554W	@504W
Resistance (kΩ)	70	82	92
Theoretical Noise Floor (Johnson noise)(A^2/Hz)	$4.73x10^{-25}$	$4.04x10^{-25}$	$3.6x10^{-25}$
Measured Noise / Theoretical noise @8.4 kHz	1.45	1.48	1.36
Flicker noise corner frequency (kHz)	1.1	1.4	0.9
TCR (%/K)	-3.12	-3.03	-3.02
NETD* (mK)	44	46	39

*Parameters for NETD calculations are given in Page 61 (Table 3.6).

4.1.2 Influence of Tungsten Power

This issue is also the focal point of this thesis which investigates the fabrication of W-doped vanadium oxide that has improved bolometric properties. The study which explores the influence of W power is performed at four different W power including 0 W, 35 W (reference), 45 W and 60 W power levels. The study at 0 W tungsten power level naturally does not create a W-doped vanadium oxide but the VO_x which is widely used in microbolometer industry. The results belonging to VO_x are fairly noteworthy, and show very good resistivity uniformity with a very good TCR result (-2.48 %/K) comparable with the literary sources [20, 31]. Bolometric properties of this VO_x sample have also been the best found out in METU so far. Recipes used for this study are given in Table 4.3 including the non-uniformity results of both thickness and resistivity. The resistivity measurement results demonstrate that the existence of W species in the deposition system visibly increases the resistivity to a certain extent and then the resistivity begins to decrease as shown in Figure 4.4. TCR measurements are carried out using samples S3, S5 and S6 which show reasonable resistivity for bolometric

applications. According to the results of TCR measurements shown in Figure 4.5, TCR also increases like the resistivity and reaches -3.31 %/K at 45 W tungsten power case which is a relatively high TCR for bolometer applications and comparable with the TCR of YBCO studies previously done at METU [6, 9, 11, 12]. The noise measurement result of deposition at 45 W tungsten power also decreases remarkably. These measurements are performed using samples used for TCR measurements, and results are shown in Figure 4.6. All results are summarized in Table 4.4.

Table 4.3: Recipes of the samples used to investigate the influence of tungsten power on bolometric properties.

	S5	S3(ref)	S6	S7	S8
V Power (W)	554	554	554	554	554
W Power (W)	**-**	**35**	**45**	**60**	**70**
Ar flow (sccm)	30	30	30	30	30
O_2 flow (sccm)	3	3	3	3	3
Pressure (mTorr)	3	3	3	3	3
Deposition Temperature (°C)	RT	RT	RT	RT	RT
Thickness Non-uniformity (%)	4.2	3.7	1.1	2.4	1.2
Resistivity Non-uniformity (%)	8	23	15	20	28

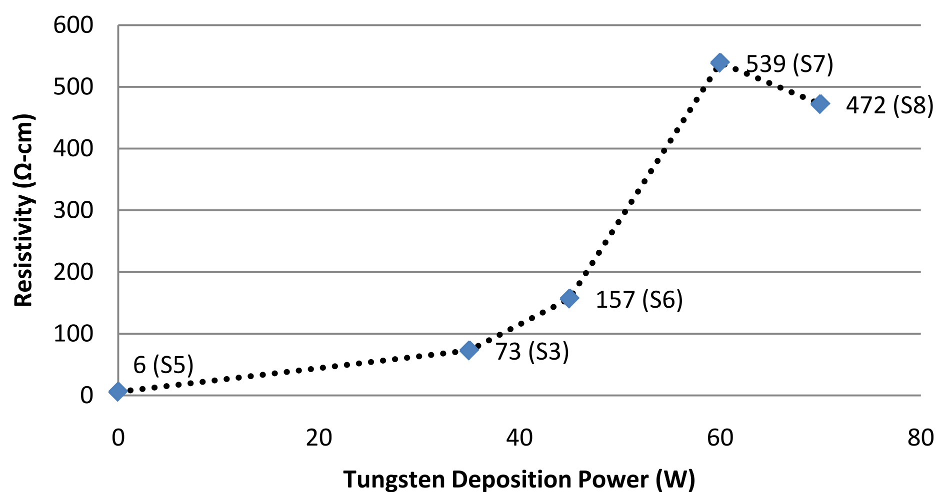

Figure 4.4: Resistivities of the samples deposited at different tungsten power levels.

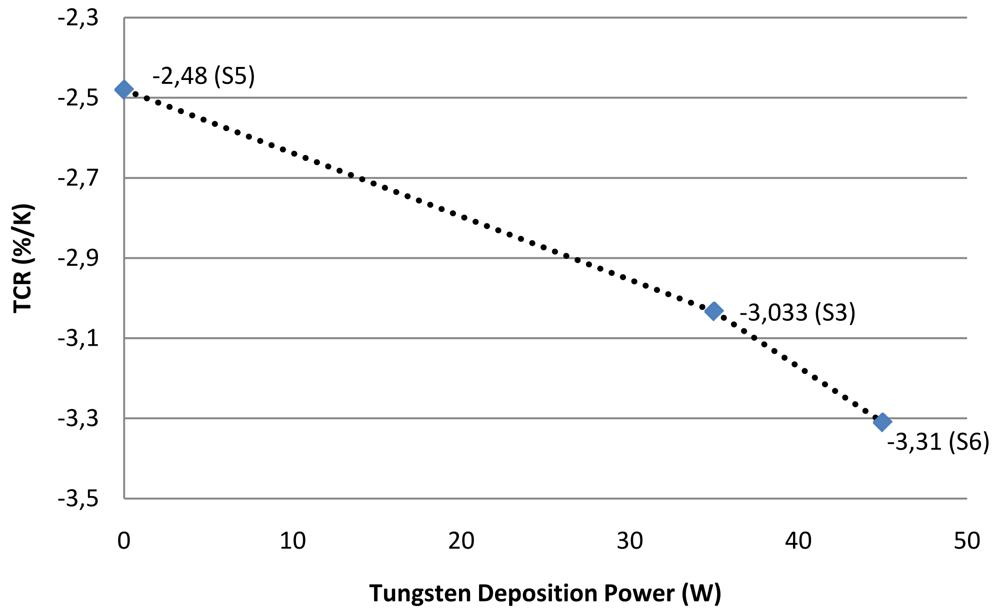

Figure 4.5: TCR measurements results of the samples deposited at different tungsten power levels.

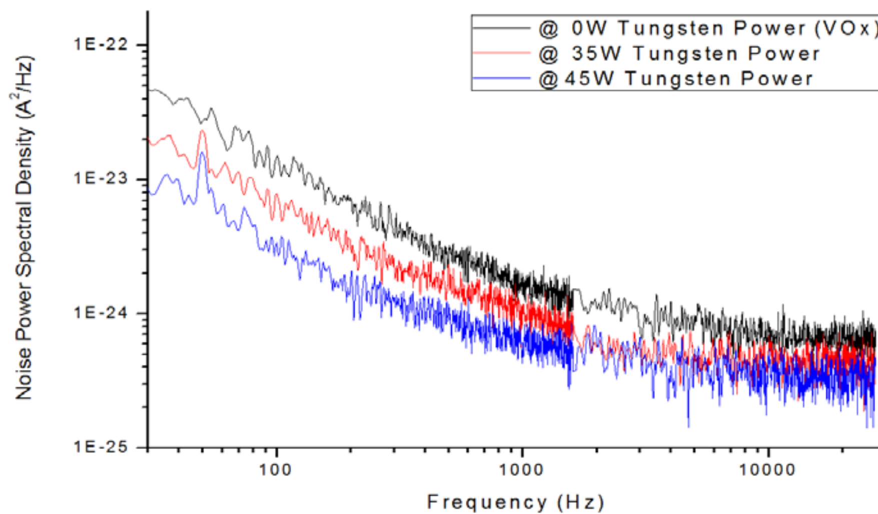

Figure 4.6: Noise behavior of the samples deposited at different tungsten power levels.

Table 4.4: Summary of the measurements for the samples deposited at different tungsten power.

	@0W(VO_x)	@35W	@45W
Resistance (kΩ)	62	82	100
Theoretical Noise Floor (Johnson noise)(A^2/Hz)	$5.34x10^{-25}$	$4.04x10^{-25}$	$3.31x10^{-25}$
Measured Noise / Theoretical noise @8.4 kHz	1.77	1.48	1.35
Flicker noise corner frequency (kHz)	2.2	1.4	0.8
TCR (%/K)	-2.48	-3.03	-3.31
NETD* (mK)	67	46	35

*Parameters for NETD calculations are given in Page 61 (Table 3.6).

4.1.3 Influence of Oxygen Flow

The investigation of the variation in the oxygen flow on the deposited VWO film is made at four different oxygen flow rates. The studied recipes are shown in Table 4.5 including the thickness and resistivity non-uniformity. It can be monitored from the results that the non-uniformity of the deposited VWO film increases as oxygen flow in the chamber rises. Studies regarding tungsten power influence have showed that the resistivity uniformity is enhanced when the tungsten contribution to the system is removed. As a consequence, it can be concluded that the resistivity non-uniformity results from compositional change of tungsten-oxygen interaction at 3 mTorr.

The resistivity shows a direct relation with the increasing oxygen flow, and this also couples with an increase in TCR as seen from Figures 4.7 and Figure 4.8. TCR of 4.5 sccm and 5.5 sccm cases give similar results but the increase in TCR is far more observable when the 3 sccm and 4.5 sccm cases are compared. TCR and noise measurements are

executed using the samples S3, S9 and S10. The noise measurement of S10 exhibits an abnormally higher noise with corner frequency at 7.5 kHz. Noise measurement results of the samples can be seen in Figure 4.9. All measurement results regarding bolometric properties are presented in Table 4.6.

Table 4.5: Recipes of the samples used to investigate the influence of oxygen flow on bolometric properties

	S3(ref)	S9	S10	S11
V Power (W)	554	554	554	554
W Power (W)	35	35	35	35
Ar flow (sccm)	30	30	30	30
O_2 flow (sccm)	**3**	**4.5**	**5.5**	**6**
Pressure (mTorr)	3	3	3	3
Deposition Temperature (°C)	RT	RT	RT	RT
Thickness Non-uniformity (%)	3.7	2.4	1.2	1.7
Resistivity Non-uniformity (%)	23	25	45	67

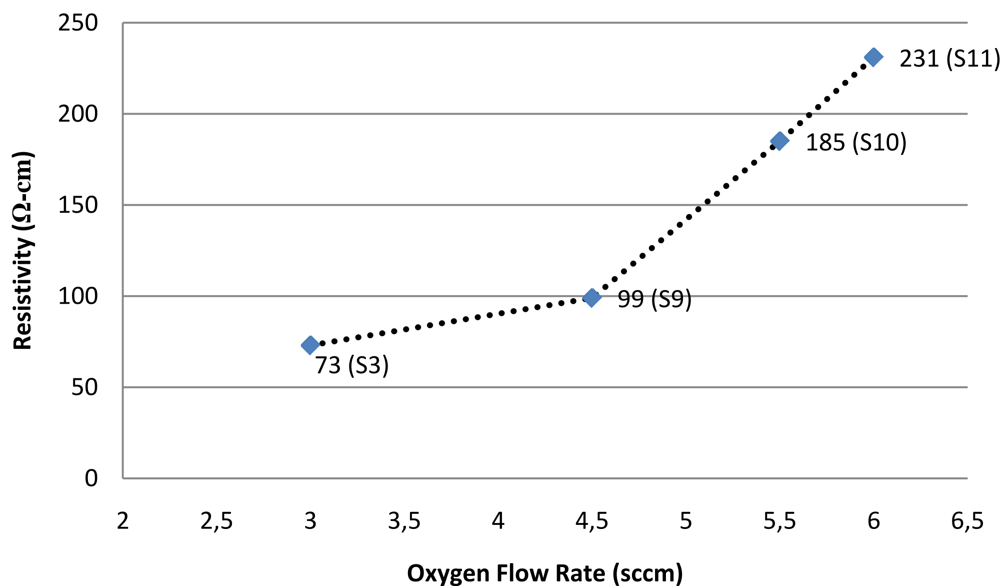

Figure 4.7: Resistivities of the samples deposited at different oxygen flow rates.

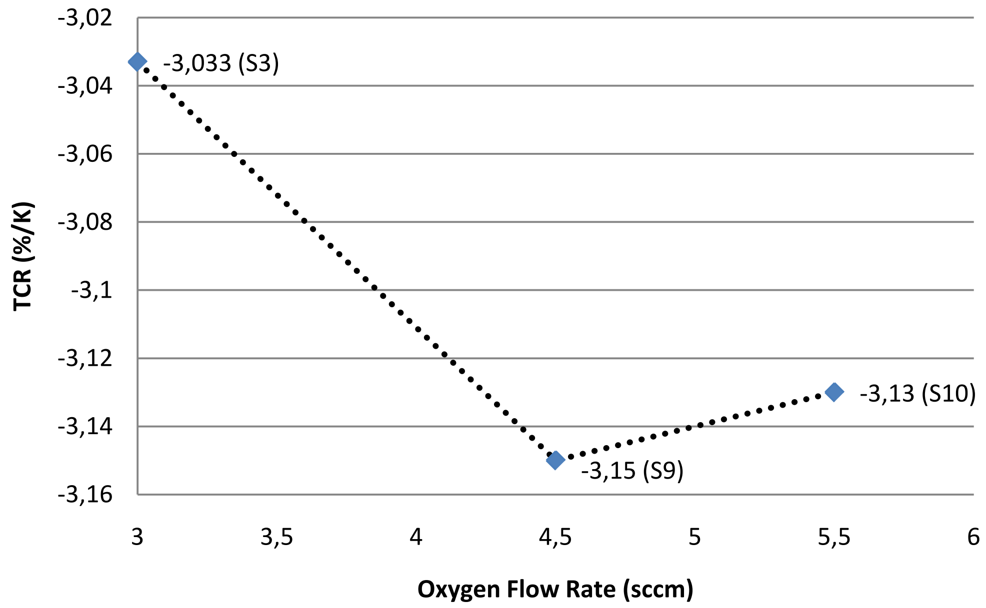

Figure 4.8: TCR measurements of the samples deposited at different oxygen flow rates.

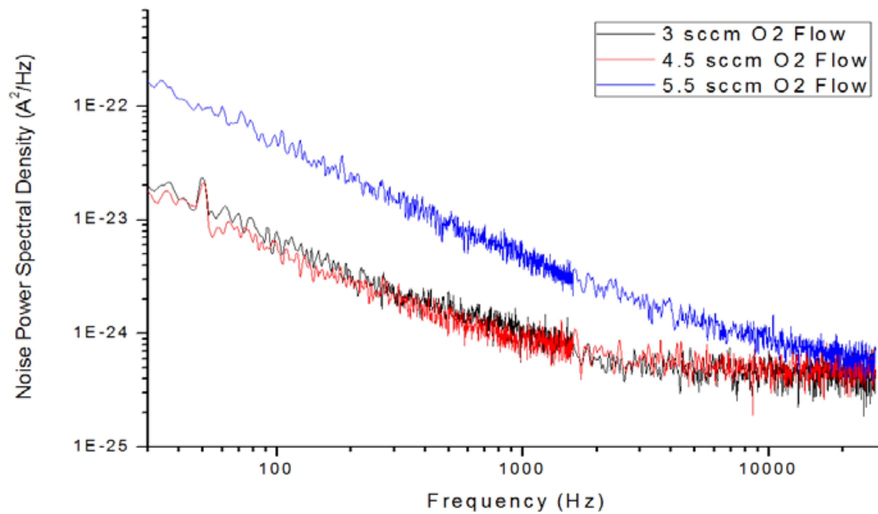

Figure 4.9: Noise behavior of the samples deposited at different oxygen flow rates.

Table 4.6: Summary of the measurements for the samples deposited at different oxygen flow rates.

	@ 3 sccm	@4.5 sccm	@5.5 sccm
Resistance (kΩ)	82	72	81
Theoretical Noise Floor (Johnson noise)(A^2/Hz)	4.04×10^{-25}	4.6×10^{-25}	3.31×10^{-25}
Measured Noise / Theoretical noise @8.4 kHz	1.48	1.36	3.27
Flicker noise corner frequency (kHz)	1.4	1	7.5
TCR (%/K)	-3.03	-3.15	-3.13
NETD* (mK)	46	44	78

*Parameters for NETD calculations are given in Page 61 (Table 3.6).

4.1.4 Influence of Argon Flow

Ar flow rate of the sputtering system directly influences the deposition rates of the samples. This is studied by depositing VWO at two more different Ar flow rates except the reference. The recipes used for this study are given in Table 4.7. The resistivity measurements have made it clear that the reference sample provides the lowest resistivity, and both the increase and the decrease in Ar flow resulted in an increase in resistivity (Figure 4.10). In 20 sccm Ar flow case, resistivity increase can be resulted from raised ratio of W species in the film according to XPS results. However, the 40 sccm case shows a reduction in W and such an increase in resistivity can be resulted from increase in the formation of high resistive V states. The Change in TCR is a lot more observable in 20 sccm Ar flow rate. The change in TCR can be seen in Figure 4.11. The noise measurement results in Figure 4.12 and Table 4.8 display a noticeable noise reduction with corner frequencies at 0.8 kHz.

Table 4.7: Recipes of the samples used to investigate the influence of argon flow on bolometric properties

	S12	S3(ref)	S13
V Power (W)	554	554	554
W Power (W)	35	35	35
Ar flow (sccm)	**20**	**30**	**40**
O_2 flow (sccm)	3	3	3
Pressure (mTorr)	3	3	3
Deposition Temperature (°C)	RT	RT	RT
Thickness Non-uniformity (%)	1.2	3.7	1.6
Resistivity Non-uniformity (%)	17	23	18

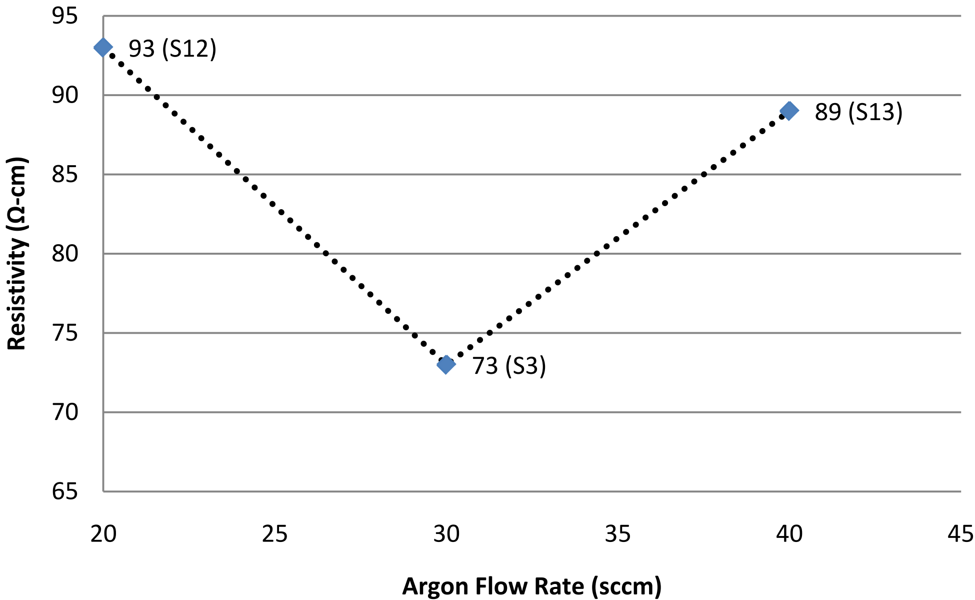

Figure 4.10: Resistivities of the samples deposited at different argon flow rates.

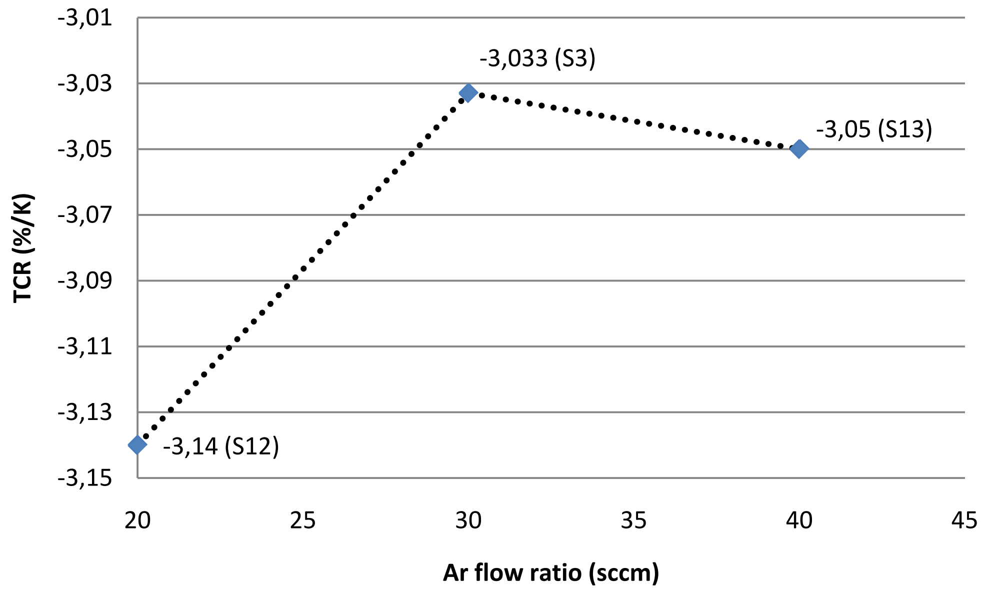

Figure 4.11: TCR measurement results of the samples deposited at different argon flow rates.

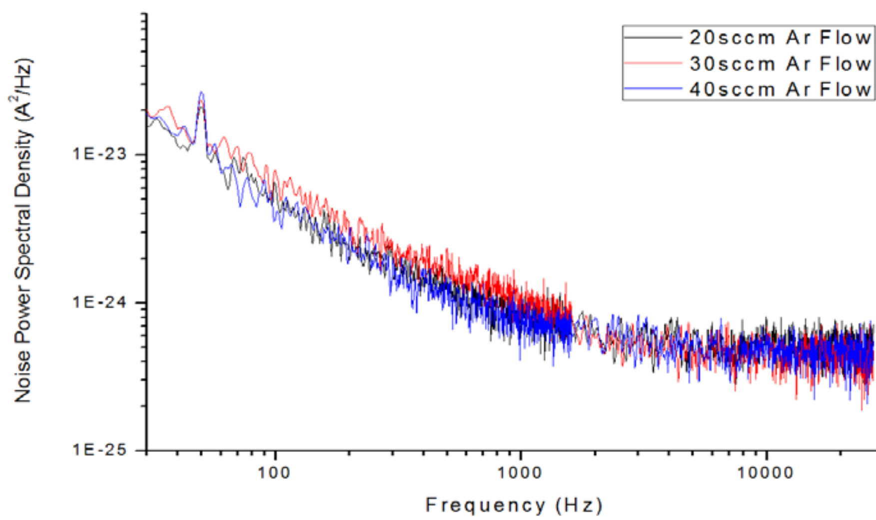

Figure 4.12: Noise behavior of the samples deposited at different argon flow rates.

Table 4.8: Summary of the measurements for the samples deposited at different argon flow rates.

	@ 20 sccm	@ 30 sccm	@ 40 sccm
Resistance (kΩ)	70	82	78
Theoretical Noise Floor (Johnson noise)(A^2/Hz)	$4.73x10^{-25}$	$4.04x10^{-25}$	$4.25x10^{-25}$
Measured Noise / Theoretical noise @8.4 kHz	1.32	1.48	1.37
Flicker noise corner frequency (kHz)	0.8	1.4	0.8
TCR (%/K)	-3.14	-3.03	-3.05
NETD* (mK)	43	46	44

*Parameters for NETD calculations are given in Page 61 (Table 3.6).

4.1.5 Influence of Working Pressure

Working pressure influence on bolometric properties was examined at four different pressure levels of 2, 3, 4 and 5 mTorr which have been coded as S14, S3, S15 and S16 respectively as shown in Table 4.9. It should be noted here that the resistivity non-uniformity of the sample S14 is found to be perfect. The conducted resistivity measurements show an increasing regime as the pressure increases as seen in Figure 4.13. TCR and noise measurements have been conducted using the samples S14, S3 and S15. S15 indicates an increasing TCR as the pressure increases as a result of an increasing resistivity (Figure 4.14). However, S14 shows an exceptional TCR results and gives higher TCR with lower resistivity which is a desired bolometric property. According to the noise measurement results shown in Figure 4.15 and Table 4.10, working pressure of 2 mTorr is also fairly advantageous in terms of noise. All measurements results are summarized in Table 4.10.

Table 4.9: Recipes of the samples used to investigate the influence working pressure on bolometric properties.

	S14	S3(ref)	S15	S16
V Power (W)	554	554	554	554
W Power (W)	35	35	35	35
Ar flow (sccm)	30	30	30	30
O_2 flow (sccm)	3	3	3	3
Pressure (mTorr)	**2**	**3**	**4**	**5**
Deposition Temperature (°C)	RT	RT	RT	RT
Thickness Non-uniformity (%)	1	3.7	1.5	1.5
Resistivity Non-uniformity (%)	1	23	23	28

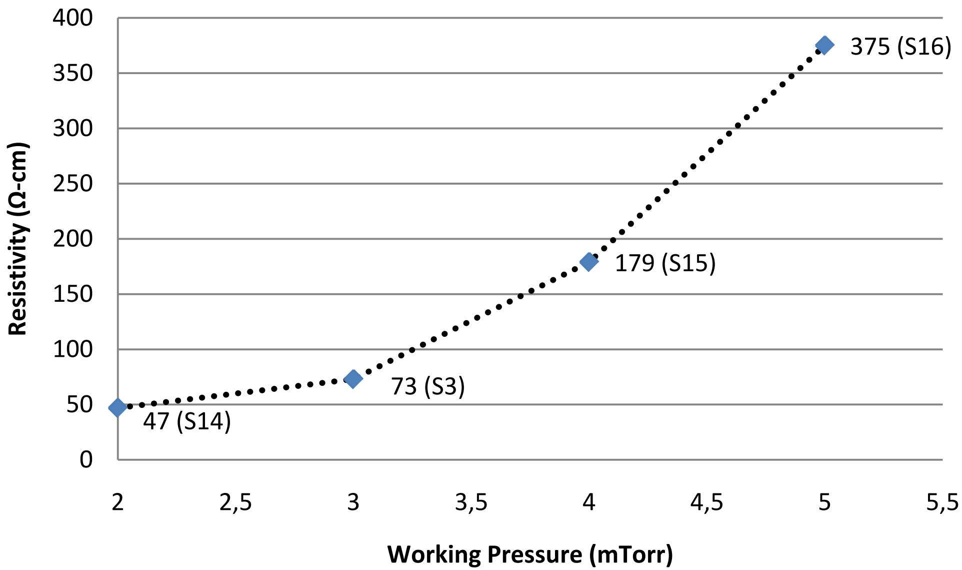

Figure 4.13: Resistivities of the samples deposited at different working pressures.

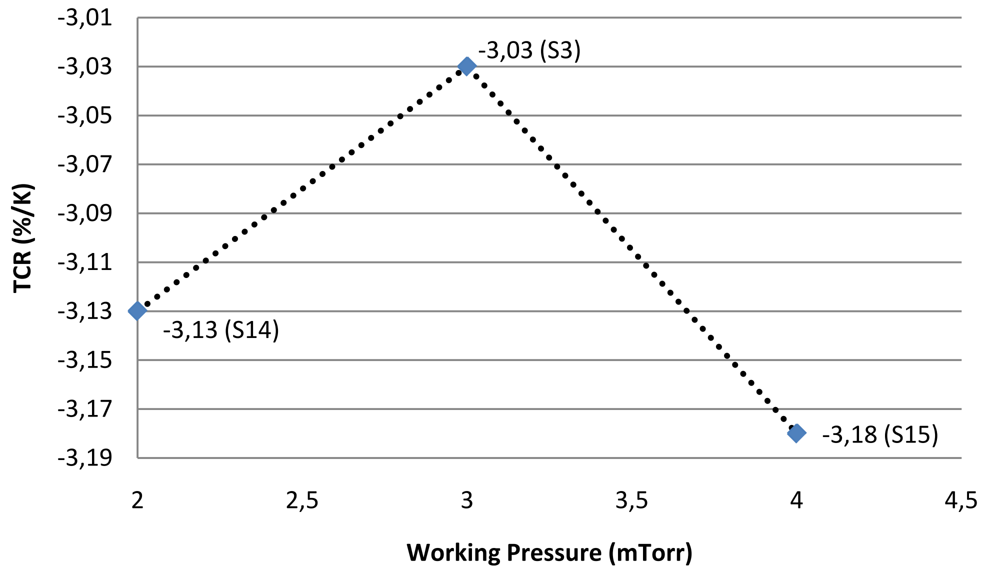

Figure 4.14: TCR measurement results of the samples deposited at different working pressures.

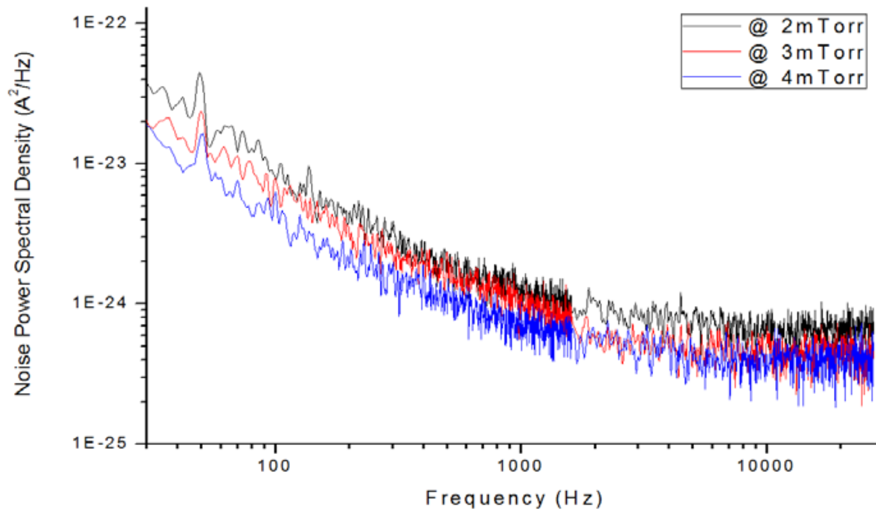

Figure 4.15: Noise behavior of the samples deposited at different working pressures.

Table 4.10: Summary of the measurements for the samples deposited at different working pressures.

	@ 2 mTorr	@ 3 mTorr	@ 4 mTorr
Resistance (kΩ)	56	82	94
Theoretical Noise Floor (Johnson noise)(A^2/Hz)	$5.91x10^{-25}$	$4.04x10^{-25}$	$3.52x10^{-25}$
Measured Noise / Theoretical noise @8.4 kHz	1.37	1.48	1.39
Flicker noise corner frequency (kHz)	1.1	1.4	1
TCR (%/K)	-3.13	-3.03	-3.18
NETD* (mK)	54	46	39

*Parameters for NETD calculations are given in Page 61 (Table 3.6).

4.1.6 Influence of Hot Deposition Condition

One of the controllable parameters of the AJA sputtering system is the deposition temperature of the substrate. Because the deposition temperatures for VO_x and VWO are generally above room temperature in literature, this issue also has to be examined. The VWO depositions during this study were performed at room temperature, 150 °C and 250 °C coded as S3, S17 and S18 respectively. The depositions are initialized 30 minutes after the substrate reaches to set temperature to acquire a uniform temperature distribution throughout the 6″ wafer. The recipes including the non-uniformity issues in Table 4.11 show that the resistivity non-uniformity of the deposition at 250 °C is abnormally high. The resistivity of VWO tends to decrease as the substrate temperature goes up as seen in Figure 4.16. Even so, TCR measurements does not display the same tendency and another desired case of low resistivity and higher TCR has been obtained at 150 °C substrate temperature. TCR measurement results concerning this study are shown in Figure 4.17. Noise measurement results show that hot deposition deteriorates the noise behavior. While the noise behavior of S17 is reasonable,

S18 suffers from its lower TCR and higher noise corner frequency (Figure 4.18). All measurement results are summarized in Table 4.12.

Table 4.11: Recipes of the samples used to investigate the influence of deposition at different substrate temperatures on bolometric properties.

	S3(ref)	S17	S18
V Power (W)	554	554	554
W Power (W)	35	35	35
Ar flow (sccm)	30	30	30
O_2 flow (sccm)	3	3	3
Pressure (mTorr)	3	3	3
Deposition Temperature (°C)	**RT**	**150**	**250**
Thickness Non-uniformity (%)	3.7	1.4	1.3
Resistivity Non-uniformity (%)	23	21	62

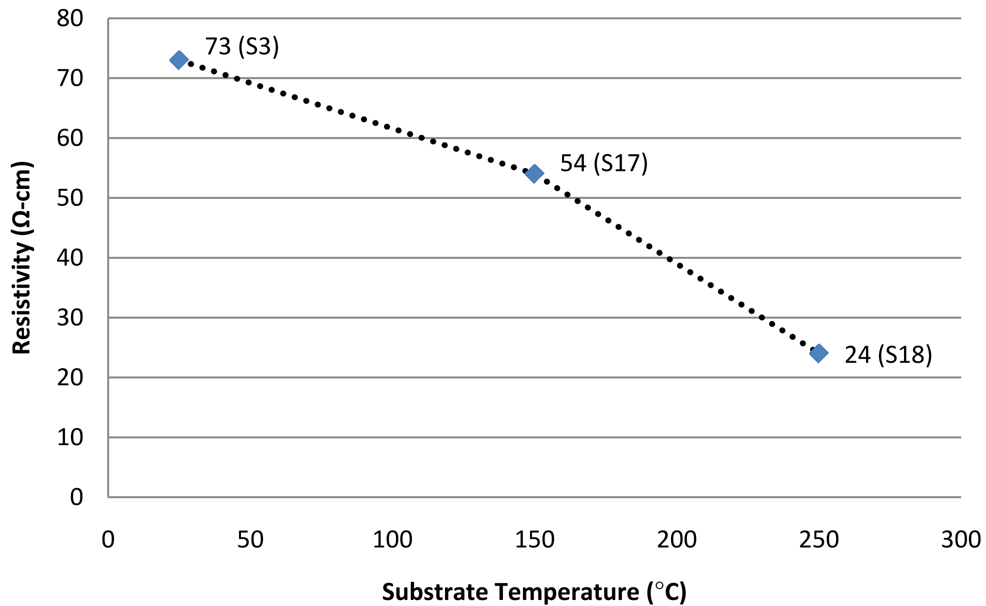

Figure 4.16: Resistivities of the samples deposited at different substrate temperatures.

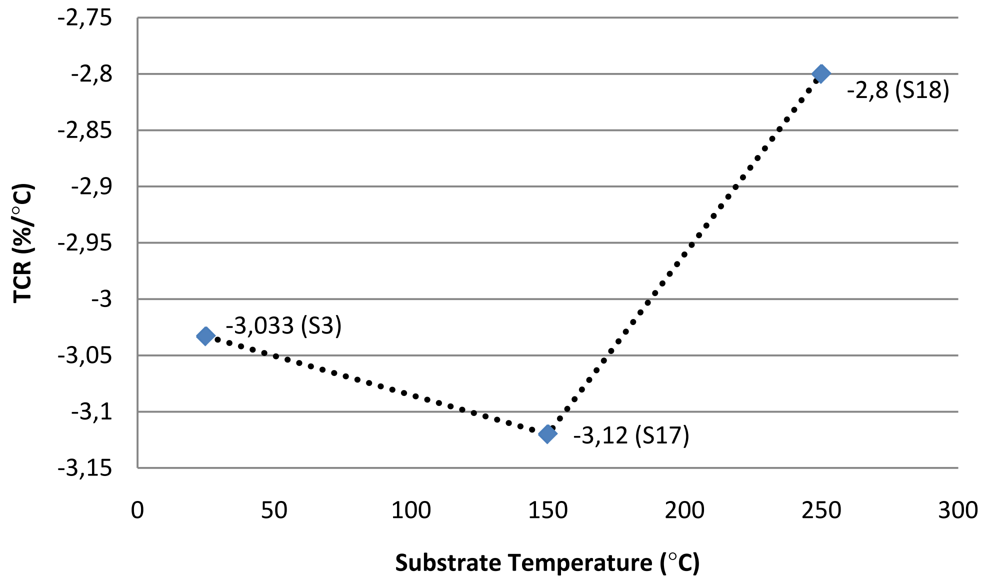

Figure 4.17: TCR measurements of the samples deposited at different substrate temperatures.

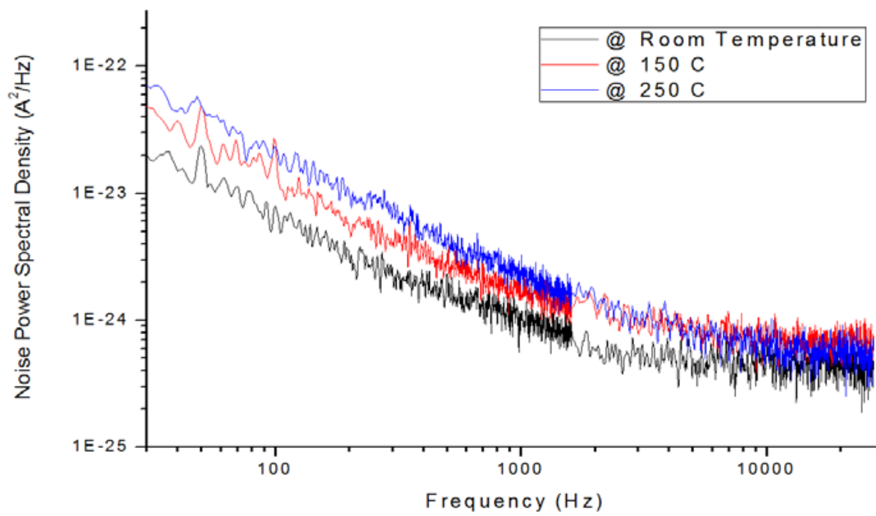

Figure 4.18: Noise behavior of the samples deposited at different substrate temperatures.

Table 4.12: Summary of the measurements for the samples deposited at different substrate temperatures.

	@ RT	@ 150 °C	@ 250 °C
Resistance (kΩ)	82	55	70
Theoretical Noise Floor (Johnson noise)(A^2/Hz)	$4.04x10^{-25}$	$6.02x10^{-25}$	$4.73x10^{-25}$
Measured Noise / Theoretical noise @8.4 kHz	1.48	1.66	2.1
Flicker noise corner frequency (kHz)	1.4	1.8	3
TCR (%/K)	-3.03	-3.12	-2.8
NETD* (mK)	46	61	77

*Parameters for NETD calculations are given in Page 61 (Table 3.6).

4.1.7 Influence of Post-Annealing

This method is a generally applied method as a post-deposition process in order to transform the deposited material into the desired compositional structure. Thus, post-annealing process is examined to understand the behavior of the deposited VWO structure.

Deposited VWO thin film with the reference recipe annealed at 300 °C in an atmospheric ambience for different time periods. The reason for choosing 300 °C as the annealing temperature is to keep the process compatible with the CMOS readout circuitry [50]. This study is not performed in wafer level. Identical dies of the wafer fabricated using reference recipe is used for this investigation. The resistivity measurements have proven that the resistivity decreases as a function of the annealing time as seen in Figure 4.19. TCR measurements also display the same tendency as expected (Figure 4.20). Nonetheless, the most valuable results of this study are observed in noise behavior. Even a 15-minute post-annealing enhances the noise frequency to 0.7 kHz while it is 1.4 kHz in as-deposited form. These results can be seen in Figure 4.21 and summary of all results can be found in Table 4.13.

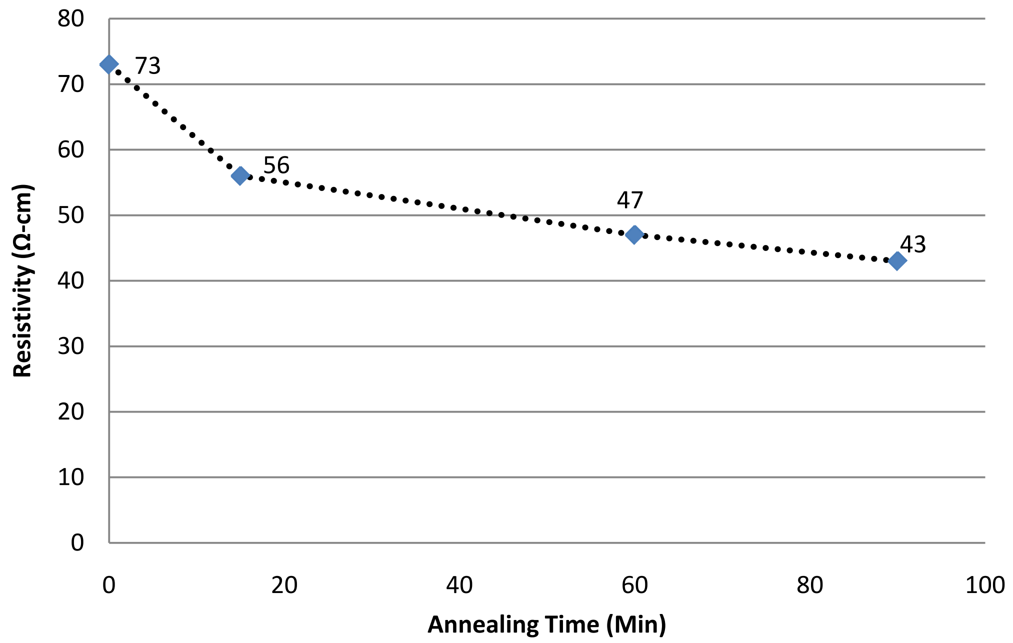

Figure 4.19: Resistivities of the sample annealed for different time periods.

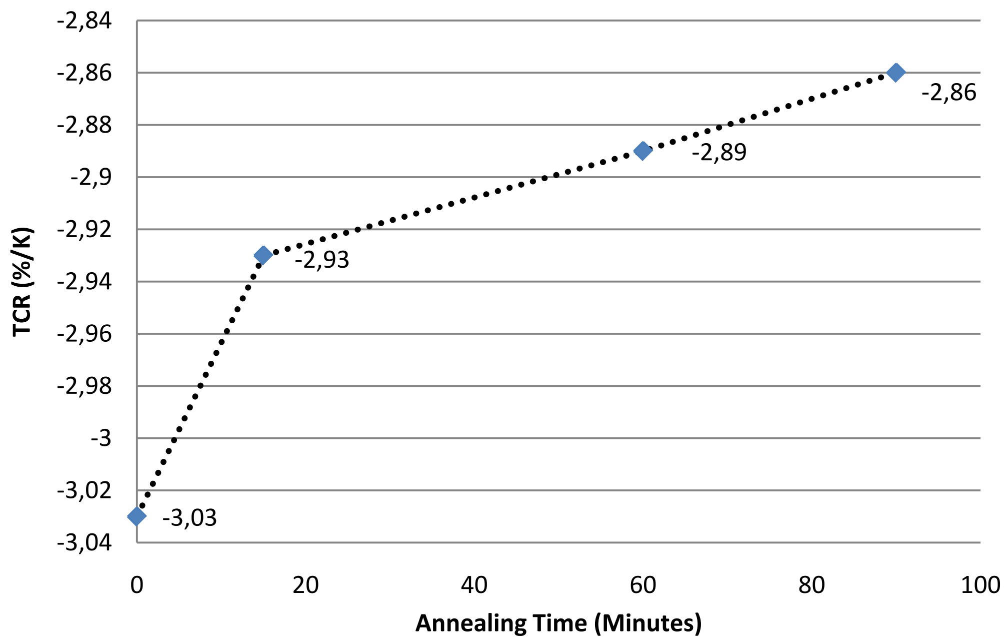

Figure 4.20: TCR measurements of the sample annealed at 300 °C for different time periods.

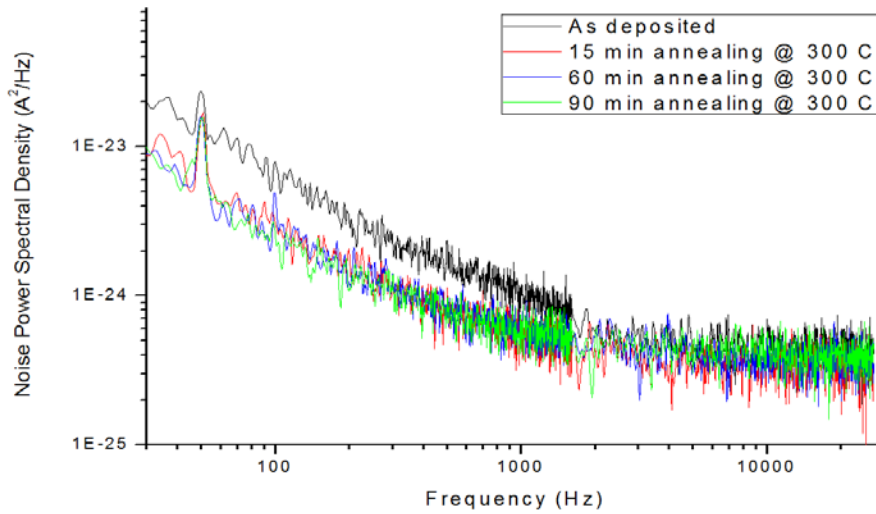

Figure 4.21: Noise behavior of the sample annealed at 300 °C for different time periods.

Table 4.13: Summary of the measurements for the samples annealed at 300 °C for different time periods.

	As deposited	15 min	60 min	90 min
Resistance (kΩ)	82	105	94	90
Theoretical Noise Floor (Johnson noise) (A^2/Hz)	4.04×10^{-25}	3.15×10^{-25}	3.52×10^{-25}	3.68×10^{-25}
Measured Noise / Theoretical noise @8.4 kHz	1.48	1.31	1.27	1.26
Flicker noise corner frequency (kHz)	1.4	0.7	0.6	0.6
TCR (%/K)	-3.03	-2.93	-2.89	-2.86
NETD* (mK)	46	37	39	40

*Parameters for NETD calculations are given in Page 61 (Table 3.6).

4.1.8 Influence of Oxygen Plasma

There is no literary information on the effects of oxygen plasma exposure to the deposited VWO film. Yet, Eren Çanga's studies [11] regarding oxygen plasma exposure of YBCO material have concluded that this process reduces the noise of the YBCO considerably as a function of application time. Hence, a similar observation is made for the VWO, and the deposited VWO has been exposed to oxygen plasma for 30 and 60 minutes. The resistivity measurements after both applications do not reflect observable changes in resistivity. This study is also not performed in wafer level. However, the dies used from the wafer fabricated with reference recipe belong to identical regions used for comparison.

With respect to TCR and noise, a remarkable enhancement is observed for 30-minute oxygen plasma exposure. As it keeps the TCR at as-deposited level, it reduces the noise corner frequency substantially. These results can be seen in Figure 4.22, Figure 4.23 and Table 4.14. Nonetheless, an application lasting for a longer period of time, just like in a 60-minute oxygen plasma exposure case, results in a failure with lower TCR and more noisy.

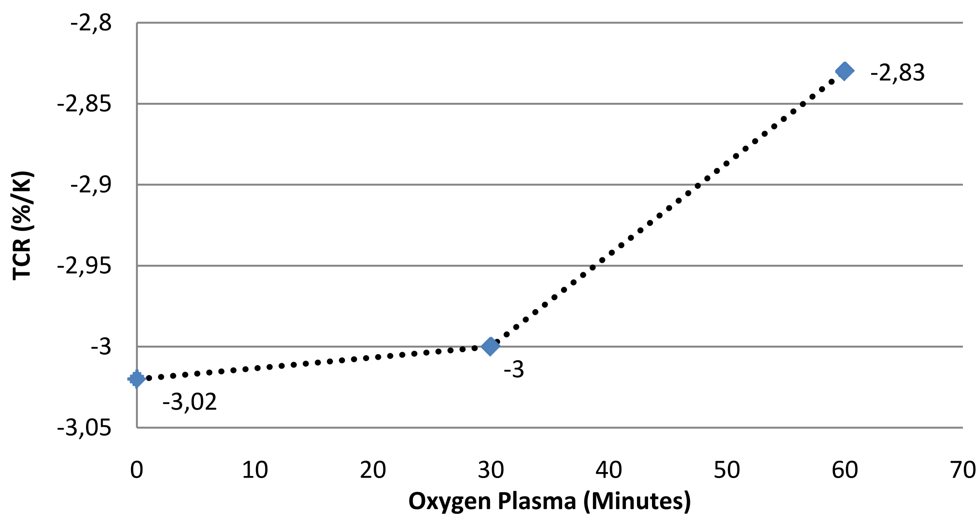

Figure 4.22: TCR measurements of the sample exposed to oxygen plasma for different time periods.

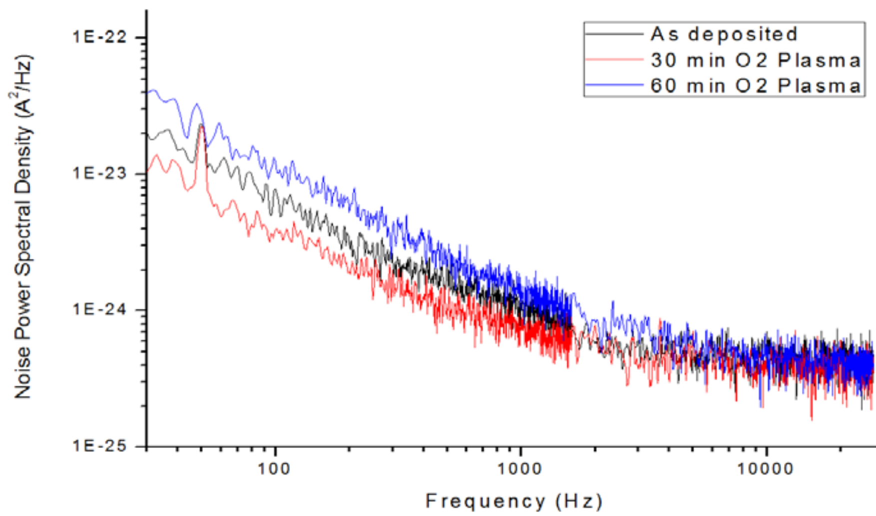

Figure 4.23: Noise behavior of the sample exposed to oxygen plasma for different time periods.

Table 4.14: Summary of the measurements for the samples exposed to oxygen plasma for different time periods.

	As deposited	30 min	60 min
Resistance (kΩ)	82	86	97
Theoretical Noise Floor (Johnson noise) (A^2/Hz)	4.04×10^{-25}	3.85×10^{-25}	3.41×10^{-25}
Measured Noise / Theoretical noise @8.4 kHz	1.48	1.32	1.92
Flicker noise corner frequency (kHz)	1.4	0.8	2.6
TCR (%/K)	-3.03	-3	-2.83
NETD* (mK)	46	38	49

*Parameters for NETD calculations are given in Page 61 (Table 3.6).

4.2 Studies on Optimized VWO Recipe

An optimized VWO recipe is attained in consideration of the studies explained in Section 4.1. Initial studies on an optimized recipe have been determined as the combination of sputtering parameters which give constructive results on bolometric properties. However, this recipe does not work and the resultant resistivity is found over 1500 Ω-cm with 79% non-uniformity. The attained optimized recipe for this thesis at the end of further studies shows outstanding results and reproducible. This recipe is given in Table 4.15.

Table 4.15: Optimized VWO recipe of this thesis study and its bolometric properties.

Optimized VWO Recipe		Properties	
V Power (W)	554	Resistivity (Ω-cm)	113
W Power (W)	45	TCR (%/K)	-3.31
Ar Flow (sccm)	30	Noise corner frequency (kHz)	0.9
O_2 Flow (sccm)	3	Thickness non-uniformity (%)	4
Base Pressure (mTorr)	$< 10^{-7}$	Resistance non-uniformity (%)	4
Pressure (mTorr)	2		
Substrate Temperature (°C)	RT		

This recipe is studied with both planar and enhanced-sandwich electrode structure. When the process flow of microbolometer fabrication is taken into account, the fabricated resistors with planar structures should also be deposited with 0.2 μm silicon nitride. This deposition is performed in PECVD on a 300 °C-hot plate for 18 minutes. Therefore, the effect of

PECVD atmosphere on resistor out of VWO should be examined. Table 4.16 shows the result of this study and no negative effect has been observed as in the YBCO case explained in Chapter 2.

Table 4.16: Comparison between bolometric properties of optimized recipe before and after PECVD conditions.

	As-deposited	After 18-minute PECVD condition
Resistance (kΩ)	85	73
Resistivity (Ω-cm)	113	99
Corner Frequency (kHz)	0.9	0.8
TCR (%/K)	-3.311	-3.244
NETD (mK)	44	34

*Parameters for NETD calculations are given in Page 61 (Table 3.6).

For the comparison of VWO and YBCO, a couple of resistors are fabricated using the enhanced-sandwich structure which is the currently used method in METU-MEMS Research and Applications Center for YBCO resistors. According to measured results shown in Figure 4.17, though the bolometric properties are close to each other, VWO exhibits a higher TCR and slightly lower noise behavior.

Table 4.17: Comparison of YBCO and VWO shows almost identical results.

Resistive Material	YBCO	VWO
Resistance (kΩ)	55	57
Resistivity (Ω-cm)	97	100
TCR (%/K)	-3.078	-3.241
Corner Frequency (Khz)	5.7	4.9
Resistivity Non-uniformity (%)	8	3.8
Thickness Non-uniformity (%)	-	1

4.3 Structural Characterization

Structural characterization of the deposited VWO is performed using AFM, XRD and XPS characterization techniques. The results of different deposition conditions are tried to be explained in light of the results taken from these characterization techniques.

4.3.1 AFM Results

AFM is a powerful characterization technique for the surface imaging of materials. In this study, AFM characterizations of the samples are performed by using Veeco Multimode V in METU Central Laboratory. The tapping mode has been used as the scan mode which enables the phase imaging. The phase imaging mode provides information concerning the compositional characterization of the sample.

AFM measurements with regard to VWO are conducted for the samples of S1, S3 (ref), S5, S10, S12, S13, S18, and the conditions of 90-minute post-annealing and 60-minute oxygen plasma exposure. The most remarkable results belong to samples of S3, S1, S5, S10, S18 and 90-minute post-annealed case. The results of these measurements are summarized in Table 4.15 and the 3D views are given in Figure 4.24. All AFM measurement results can be found in Appendix A.

Table 4.18: Summary of the AFM characterization

Sample	Changed Parameter	Average Diameter (nm)	Roughness (nm)
S3 (ref)	@ 554 W V power	47	0.90
S5	@ 0 W W power	29	0.82
S1	@ 500 W V power	29	0.78
S10	@ 5.5 sccm O_2 flow	25	0.9
S18	@250 °C	36	1.6
S3	90-min post-annealing	59	2.7

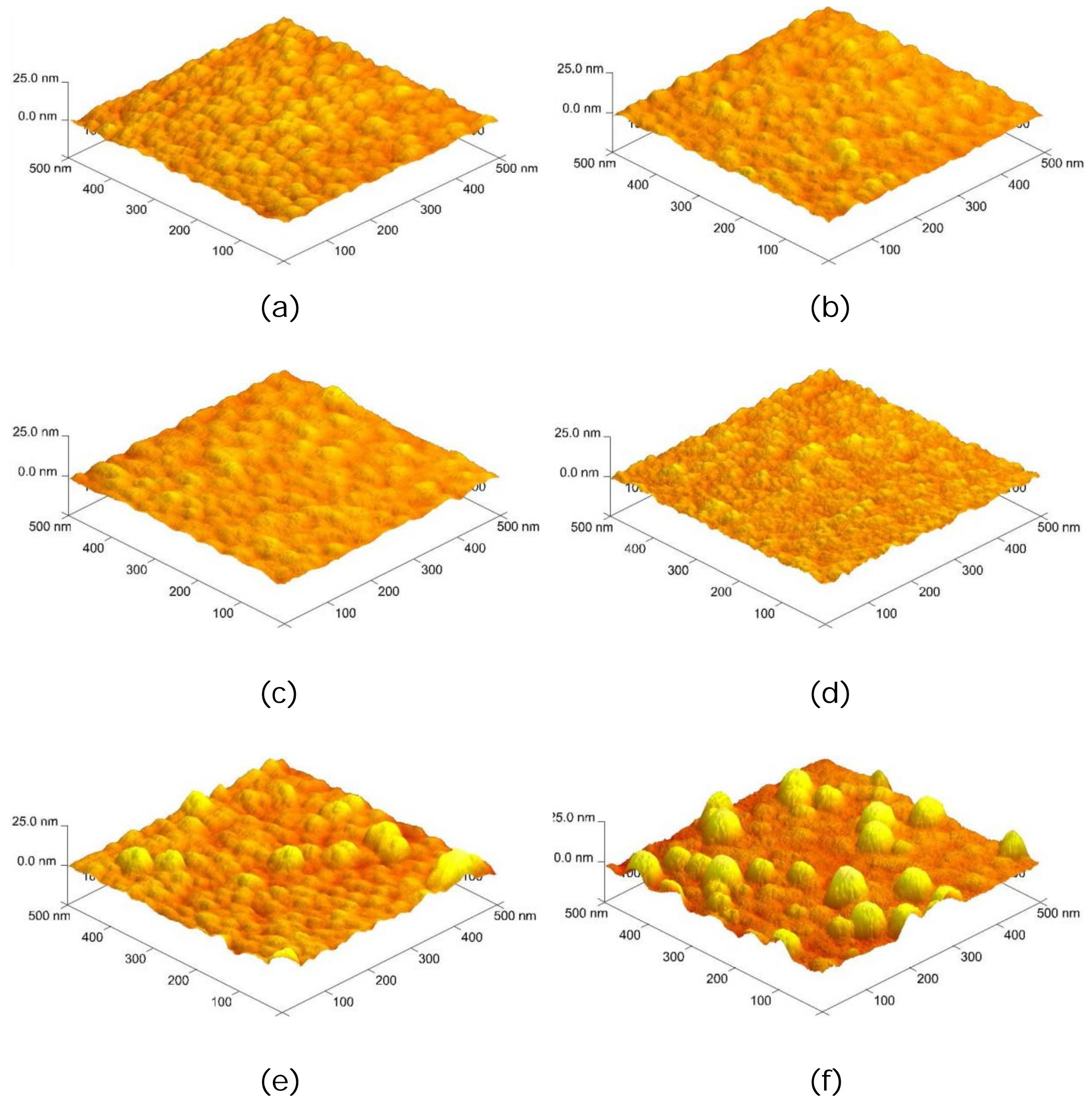

Figure 4.24: 3D AFM maps taken from samples S3 (a), S5 (b), S1 (c), S10 (d), S18 (e) and 90-minute post-annealed S3 (f).in 0.5 μm x0.5 μm area.

The comparison of (a) and (b) in Figure 4.24 points out that the addition of tungsten to the deposition system results in more apparent grains. Another result of this study is the more vanadium power is applied, the higher roughness is obtained ((a) and (c)). The size of the grains gets smaller when the oxygen flow rate increases from 3 to 5.5 sccm ((a) and (d)). A notable change in surface topography is observed in hot deposition condition and post-annealing process. High temperature

during deposition or after deposition causes agglomeration on the surface (Figure 4.24 (e) and (f)).

4.3.2. XRD Results

Crystallographic structure of the deposited VWO films is analyzed using Rigaku Ultima-IV X-Ray Diffractometer in METU Central Laboratory using continuous scan mode (Cu/40kW/30mA). The studies are performed using grazing incidence technique (fixed angle-2 degree) which is surface sensitive and gives stronger signals. VWO samples prepared for XRD measurements are grown on (100) Si test wafer. Initially, in order to discriminate the signal from the Si wafer and deposited VWO, a pure Si wafer is measured and the result is given in Figure 4.25. During the XRD studies this signal has not been obtained which means all diffraction taken is from the deposited VWO film.

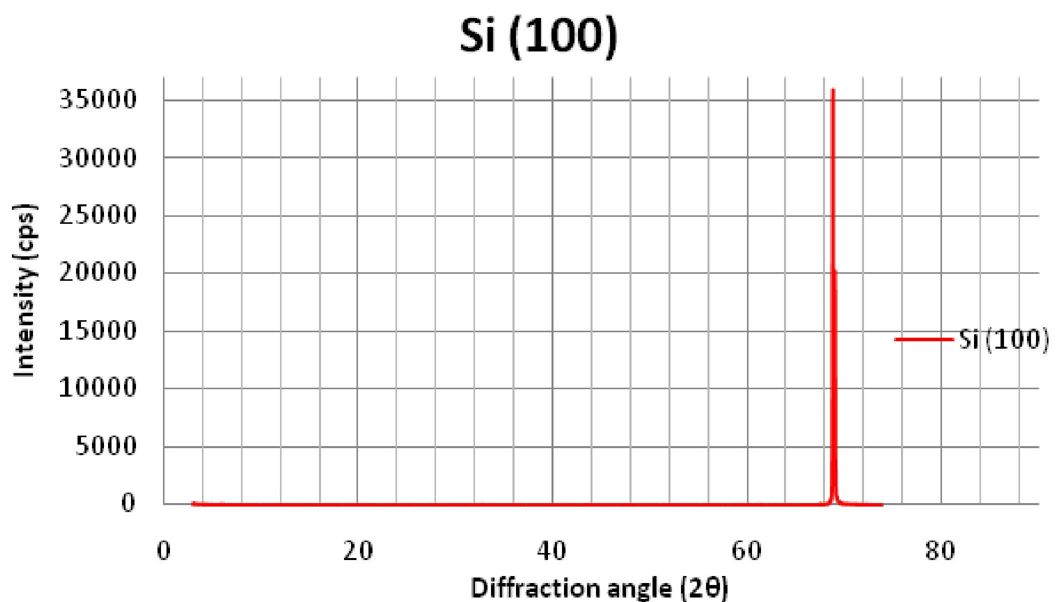

Figure 4.25: XRD pattern of (100) Si wafer.

Selected recipes for XRD measurements are S5 (no tungsten contribution-pure VO_x), S3 (reference VWO sample) and 90-minute post-annealed S3.

According to XRD results of these samples shown in Figure 4.26, pure mixed phase vanadium oxide (S5) reveals a poly-crystal structure oriented at (202) plane, and V_2O_5 is the dominant phase. This dominance is also observed during the analyses of the XPS studies. The XRD pattern of the VO_2 and V_2O_3 are not sharp and intense indicating that the grain sizes are very fine [20].

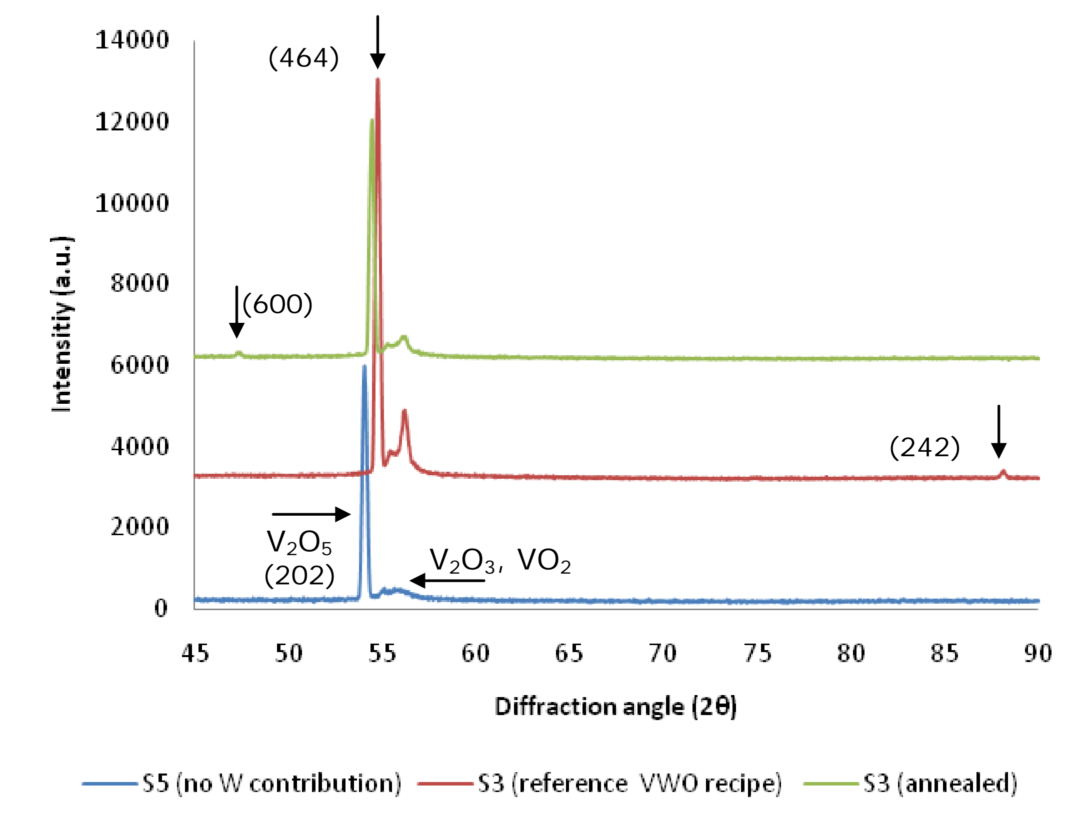

Figure 4.26: XRD results of S3, S5 and post-annealed S3. Measurements are performed using GIXD technique at 2° incidence angle.

Tungsten contribution to vanadium oxide (S3) solid solution does not alter the poly-crystal structure. However, the resultant structure is oriented in the (464) plane which means the (202) main orientation of pure VO_x is no longer stable owing to the excess of W species [34]. Tungsten contribution also increases the sharpness and intensity of the peaks which can be correlated with the AFM results showing increasing grain size. Additional evidence of another crystal orientation in the (242) plane is noticeable.

When the reference sample annealed at 300 °C for 90 minutes, XRD results show degradation in crystal structure with less sharper peaks and increasing FWHM (full width at half maximum) when compared to the as-deposited S3. By applying post-annealing process, another trace of crystal orientation in (600) plane begins to be observable throughout the XRD pattern.

4.3.3 XPS Results

XPS is a progressive characterization technique which gives information on the chemical environment of elements and their oxidation states. XPS measurements for the compositional analysis of VWO films are conducted using PHI 5000 XPS instrument (Al monochromatic anode) in METU Central Laboratory.

Atomic concentrations of the deposited VWO films are looked over for each sample and shown in Table 4.19. All of these samples except S3 and oxygen plasma exposed S3 are sputtered at 2000eV to clean the surface of the VWO film. S3, the reference recipe, is examined at no sputter and sputtered conditions for 6 and 12 minutes at 2000eV. The result of this study reveals that the atomic distribution in a depth view seems fairly uniform. To conclude, the oxygen in the atmosphere does not cause a further oxidation on the surface of the VWO film. However, when the oxygen plasma is applied, the increase in atomic ratio of oxygen is notable.

Other results confirm our deposition rate measurements which have been explained in Section 3.1.2. Another significant result is that the ratio of the W in deposited VWO films never decreases to the proposed W-doping ratio of lower than 10%.

Table 4.19: Atomic ratios of the studied samples.

Sample	Changed Parameter	Sputter (min)	O (%)	V (%)	W (%)	W/(W+V) (%)
S3	reference	-	50.8	37.6	11.6	23
	reference	6	50.5	38.1	11.4	23
	reference	12	50.9	37.4	11.7	24
S3 (O_2 plasma)	60-min O_2 plasma	-	79	12.6	8.4	40
S3 (annealed)	90-min annealing	6	56.1	32	11.9	27
S5	@ 0 W W power	6	81	19.2	-	-
S1	@ 500 W V power	6	52.6	34.8	12.6	27
S10	5.5 sccm O_2 flow	6	54.3	34.3	11.4	25
S18	@ 250 °C	6	48.5	40	11.5	22
S13	40 sccm Ar flow	6	53.8	34.5	11.7	25
S12	20 sccm Ar flow	6	49.6	39.1	11.3	22

Vanadium metal forms a great number of oxide phases. Just a few of these phases are stable enough for microbolometer applications, though. These phases are V_2O_3, VO_2 and V_2O_5 and these compounds have V^{3+}, V^{4+} and V^{5+} oxidation states respectively. These states are primarily studied with S5 which contains no W contribution. The results are referenced to carbon at 284.4 eV. Figure 4.27 illustrates that the obtained VO_x recipe generates a mixed phase of VO_x film.

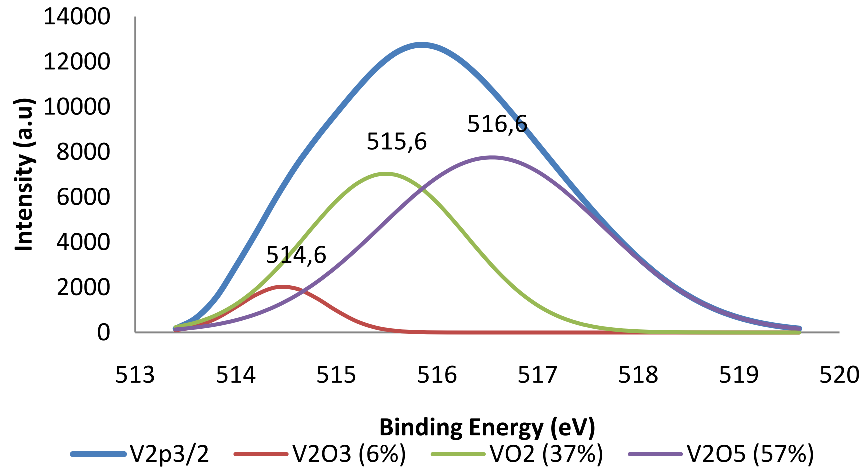

Figure 4.27: Peak fitting of $V2p_{3/2}$ core level for S5 (pure VO_x).

Peak positions of the VO_x compound are fitted by using PeakFit v4.12 software and detected peaks are found to be comparable with the literary sources [51].

V2p core level of sample S3 is also investigated and the result has been very interesting. The comparison between the results of S3 and S5 show an abnormal shift in the V2p core level while the O1s peak stays constant in both cases. The shift is clearly observable in Figure 4.28.

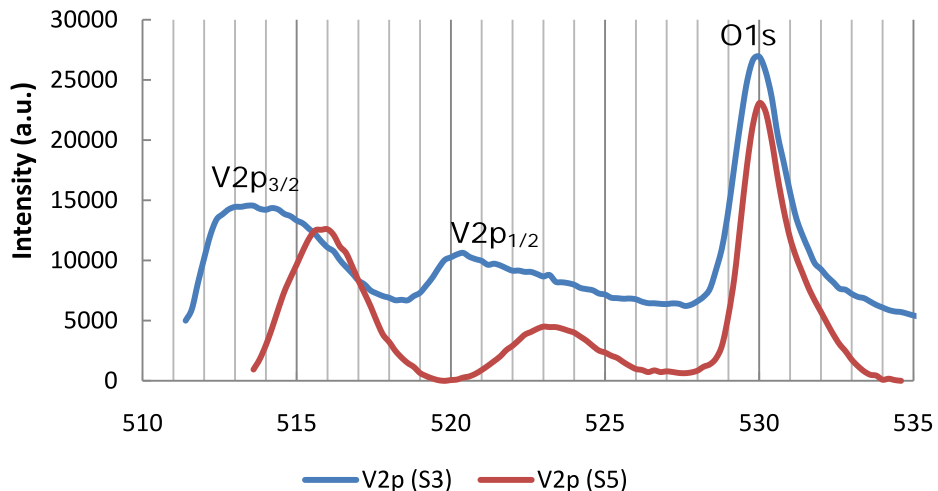

Figure 4.28: V2p core level binding energy comparison of un-doped (S5) and W-doped (S3) VO_x samples.

This shift is considered to stem from the W contribution, though this assumption is contrary to literary sources [52, 53]. However, these studies have been performed using very low W contribution below 10 %. Obtained W contribution during the studies of this thesis shows relatively higher ratios above 20%. This excess of W concentration may cause such a shift because of its substitutional doping behavior. Existence of W in substitutional sites induces extra electrons in the d band of V and this ends in less electron binding energy as a result of energy compensation [54].

CHAPTER 5

CONCLUSION AND FUTURE WORKS

This thesis study reports the development of VWO as a high performance active detector material. Although the studies on bolometric applications of this material is very limited, the results of these studies show fairly promising bolometric properties with high TCR and low noise. Deposition of VWO is performed using reactive DC magnetron co-sputtering technique in METU-MEMS Research and Applications Center. Initially, it is aimed to find a reference recipe which provides reasonable resistivity, TCR and noise behavior. Following on coming up with the reference recipe, the studies are centered on the effects of sputtering conditions. The effects of all controllable sputtering parameters are analyzed during the studies and post-deposition processes such as annealing and oxygen plasma exposure are also included.

The important achievements attained during this research study can be given as follows;

1. The studies are begun by optimizing the deposition uniformity of both vanadium and tungsten target. The thickness non-uniformity for both targets is enhanced to levels below 2%.

2. A literary study is carried out concerning the active detector materials currently used in microbolometer industry. The idea behind W-doping of VO_x is revealed. According to the application

results of VWO in microbolometers, its favorable bolometric properties are compared with the other bolometric materials.

3. The behavior of the sputtering system is investigated before the determination of the first deposition parameters. During the studies, it is aimed to acquire the highest vanadium deposition rate with respect to tungsten. These studies inform that a higher vanadium deposition rate can be acquired only by applying the highest possible power to vanadium target, by keeping the O_2/Ar flow ratio below or equal to 10%, and making the deposition at low working pressures.

4. The electrode structures that can be used for the resistor fabrication are discussed with their pros and cons. Using the planar type structures has been decided on during the studies due to its capability of straightforward fabrication and sufficiency for bolometric characterization.

5. Etching process for both electrode structure and VWO film is optimized. Finger structures with the critical dimensions below 1 μm are achieved using MRIE. Etching of the VWO layer is performed successfully using diluted hydrogen peroxide with reasonable undercut and excellent selectivity for both planar and enhanced sandwich type resistor structures.

6. A quite promising VO_x recipe is attained during the studies with notable bolometric properties.

7. Resistivity measurements are carried out by hand-calculation. The obtained resistivity values are found to be low enough for fabrication of reasonable resistors between 60-100 kΩ.

8. TCR measurements are performed between 15 °C and 37 °C which is large enough considering the working temperature of microbolometers. The lowest TCR measured at -2.48 %/K belongs to pure VO_x and it is a very good value for VO_x material when compared to the ones in literature. The highest TCR is measured at -3.31 %/K by increasing the DC power applied to the tungsten target.

9. Noise measurements are carried out using a similar circuitry to the detector read-out circuitry. The corner frequencies of the noise measurements are found between 0.6 kHz and 8 kHz. It is observed that a short-period oxygen plasma exposure and post-annealing decrease the noise of the material without any drawback.

10. How the change in the sputtering parameters affects the bolometric properties are analyzed by comparing the results with the pre-determined reference recipe. An optimized recipe showing fairly good bolometric properties in all aspects is defined according to results of this study. These results are also compared with the ones belonging to YBCO and give similar but better results.

11. The effect of PECVD atmosphere is explored and it is seen that the PECVD does not cause degradation in the bolometric properties as in the YBCO case.

12. The resistivity non-uniformity is decreased to %1 percent by decreasing the working pressure from 3 mTorr to 2. It is observed that the non-uniformity increases as a function of working pressure. Increase in O_2 flow and hot deposition conditions play the most critical roles for the deterioration in resistivity non-uniformity.

13. Structural characterization of deposited VWO film is performed using AFM, XRD and XPS characterization techniques. AFM results

introduce that the grains of the VO_x get much more observable as it is doped by tungsten. This enhancement in crystal structure is also observed in XRD results. XRD results also exhibit that the deposited films are in a poly-crystal structure. Doping of VO_x with tungsten shows a 2 eV-shift to lower binding energy in the XPS pattern of the V2p core level which is contrary to the literature. However, this is considered to result from the excess of tungsten and proves the substitutional existence of tungsten in VWO.

The studies which can be done to improve these obtained results are summarized as follows;

1. During these studies the proposed tungsten doping ratio which is below 10 % has never been reached. Sputtering of the tungsten metal can be studied using an RF source instead of the DC one because of its lower deposition rate property.

2. Instead of a co-sputtering method using separate tungsten and vanadium targets, a newly fabricated V-W alloy target with desired concentrations can be used to achieve better bolometric results.

3. Sandwich type deposition methods, such as VO_x-W-$VO_{x,}$ can be studied with a post-annealing process to form VWO films.

4. Obtained VO_x recipe has not been studied in detail because it is out of the scope of this thesis study. However, this state of material is highly likely to develop.

5. Further XPS studies can be performed to analyze the chemical structure of the VWO in detail.

6. Developed deposition conditions for VWO should be applied to single-pixel fabrication before CMOS wafer.

REFERENCES

[1] *http://en.wikipedia.org/wiki/William_Herschel#Discovery_of_ infrared _ radiation_in_sunlight*, last accessed on 07.07.2011.

[2] P. W. Kruse and D. D. Skatrud *"Uncooled Infrared Imaging Arrays and Systems,"* Academic Press, 1997.

[3] *http://cosmictimes.gsfc.nasa.gov/teachers/guide/1965/guide /murmur.html,* last accessed on 10.07.2011.

[4] *http://archimede.bibl.ulaval.ca/archimede/fichiers/23016 /apb.html,* last accessed on 10.07.2011.

[5] *http://upload.wikimedia.org/wikipedia/commons/6/6a/ Atmosfaerisk_spredning.gif*, last accessed on 10.07.2011.

[6] M. Y. Tanrıkulu, *"An Uncooled Infrared Microbolometer Array Using Surface Micromachined MEMS Technology,"* Dissertation for the Degree of Doctor of Philosophy, METU, in Department of Electrical and Electronics Engineering, 2007.

[7] P. W. Kruse, *"Uncooled Thermal Imaging Arrays, Systems and Applications,"* Tutorial texts in optical engineering, Vol. TT51, SPIE Press, 2011.

[8] A. Rogalski, "Infrared Detectors: An Overview," *Infrared Physics & Technology*, Vol. 43, pp. 187-210, 2002.

[9] U. Şenveli, *"Development of High Thermal Performance Uncooled Infrared Detector Pixels with Enhanced Resistor Structures,"* Dissertation for the Degree of Master of Science, METU, 2010.

[10] *http://upload.wikimedia.org/wikipedia/commons/9/93/ Wheatstonebridge.svg,* last accessed on 11.07.2011.

[11] E. Çanga, *"Development and Characterization of High TCR Material for Surface Micromachined Microbolometers,"* Dissertation of the Degree of Master of Science, METU, 2010.

[12] F. Çivitçi, *"Development of High Fill Factor Uncooled Infrared Detector Pixels,"* Dissertation for the Degree of Master of Science, METU, 2008.

[13] C. N. Anh and S. Moon, "Excess Noise in Vanadium Tungsten Oxide Bolometric Material," *Infrared Physics & Technology*, Vol. 50, pp. 38-41, 2007.

[14] Moon Sung, "Novel Infrared Absorbing Material Coupled Uncooled Microbolometer," *Proceedings of IEEE Sensors*, art. no. T2L-E.4, pp. 658-660, 2004.

[15] M. Kohin and N. Buttler, "Performance Limits of Uncooled VO_x Microbolometer Focal Plane Arrays," *Proceedings of SPIE*, Orlando, USA, Vol. 5406, pp. 447–453, 2004.

[16] F. Niklaus, C. Vieider, and H. Jakobsen, "MEMS-Based Uncooled Infrared Bolometer Arrays-A review," *Proceedings of SPIE*, Vol. 6836 (68360D), 2007.

[17] F. Niklaus, A. Decharat, C. Hansson, and G. Stemme, "Performance Model for Uncooled Infrared Bolometer Arrays and Performance Predictions of Bolometers Operating at Atmospheric Pressure," *Infrared Physics & Technology*, Vol. 51, pp. 168-177, 2008.

[18] R. R. T. Kumar, B. Karunagaran, D. Mangalaraj, S. K. Narayandass, P. Manoravi, M. Joseph, V. Gopal, R. K. Madaria, and J. P. Singh, "Room-Temperature Deposited Vanadium Oxide Thin Films for Uncooled Infrared Detectors," *Materials Research Bulletin*, Vol. 38, pp. 1235-1240, 2003.

[19] M. A. Todd, P. P. Donohue, R. Watton, D. J. Williams, C. J. Anthony, and M. G. Blamire, "High Performance Ferroelectric and Magnetoresistive Materials for Next-Generation Thermal Detector Arrays," *Proceedings of SPIE*, Vol. 4795, 2002.

[20] J. Dai, X. Wang, S. He, Y. Huang, and X. Yi, "Low Temperature Fabrication of VO_x Thin Films for Uncooled IR Detectors by Direct Current Reactive Magnetron Sputtering Method," *Infrared Physics & Technology*, Vol. 51, pp. 287-291, 2008.

[21] T. Akın, *"Chapter 10: CMOS-Based Thermal Sensors"* in Advanced Micro & Nanosystems vol.2 CMOS-MEMS edited by H. Baltes, O. Brand, G. K. Fedder, C. Hierold, J. Korvink, and O. Tabata, Wiley-VCH, 2005.

[22] M. M. Rana and D. P. Butler, "Amorphous $Ge_xSi_{1-x}O_y$:H Microbolometers with High Responsivity," *IEEE Sensors Conference*, 2007.

[23] A. Rogalski, "Infrared Detectors for the Future," *Acta Physica Polonica A: Optical and Acoustical Methods in Science and Technology*, Vol. 116, 2009.

[24] A. Ahmed and R. N. Tait, "Noise Behavior of Amorphous $Ge_xSi_{1-x}O_y$ for Microbolometer Applications," *Infrared Physics & Technology*, Vol. 46, pp. 468-472, 2005.

[25] S. Chen, H. Ma Hong, S. Xiang, and X. Yi, "Fabrication and Performance of Microbolometer Arrays Based on Nanostructured Vanadium Oxide Thin Films," *Smart Materials and Structures*, Vol. 16, pp. 696-700, 2007.

[26] L. Dong, R. Yue, and L. Liu, "An Uncooled Microbolometer Infrared Detector Based on Poly-SiGe Thermistor," *Sensors and Actuators A: Physical*, Vol. 105, Issue 3, pp. 286-292, 2003.

[27] V. Y. Zerov, Y. V. Kulikov, V. G. Malyarov, I. A. Khrevtov, I. I. Shaganov, and E. B. Shadrin, "Vanadium Oxide Films with Improved Characteristics for IR Microbolometric Matrices," *Technical Physics Letters*, Vol. 27, No. 5, pp. 378-380, 2001.

[28] R. B. Darling and S. Iwanaga, "Structure, Properties, and MEMS and Microelectronic Applications of Vanadium Oxides," *Sadhana-Academy Proceedings in Engineering Sciences*, Vol. 34, Part 4, pp. 531-542, 2009.

[29] Y. H. Han, I. H. Choi, H. K. Kang, J. Y. Park, K. T. Kim, H. J. Shin, and S. Moon, "Fabrication of Vanadium Oxide Thin Film with High-Temperature Coefficient of Resistance Using V_2O_5/V/V_2O_5 Multi-Layers for Uncooled Microbolometers," *Thin Solid Films*, Vol. 425, pp. 260-264, 2003.

[30] J. Nag and Jr. R. F. Haglund, "Synthesis of Vanadium Dioxide Thin Films and Nanoparticles," *Journal of Physics: Condensed Matter*, Vol. 20, 2008.

[31] A. Subrahmanyam, Y. B. K. Reddy, and C. L. Nagendra, "Nano-Vanadium Oxide Thin Films in Mixed Phase for Microbolometer Applications," *Journal of Physics D: Applied Physics*, Vol. 41, 2008.

[32] C. G. Granqvist, *"Handbook of Inorganic Electrochromic Materials,"* Elsevier, 1995.

[33] K. H. Eastwood, *"Method of Producing Thin Film Devices of Doped Vanadium Oxide Material,"* US Patent No: 3,899,407, 1975.

[34] C. Batista, R. Ribeiro, J. Carneiro, and V. Teixeira, "DC Sputtered W-Doped VO_2 Thermochromic Thin Films for Smart Windows with Active Solar Control," *Journal of Nanoscience and Nanotechnology*, Vol. 9, pp. 4220-4226, 2009.

[35] Jr. D. A. Jackson and S. M. Tomarchio, *"Method for Fabrication of Thin-Film Bolometric Material,"* US Patent No: 5,288,380, 1994.

[36] S. Moon, H. Y. Shin, Y.H. Han, *"A Method for Fabricating An Amorphous Vanadium Tungsten Oxide Thin Film,"* European Patent No: EP 1 560 008 B1, 2008.

[37] Y. H. Han, I. H. Choi, S. Moon, and C. S. Son, "Characteristics of Vanadium-Tungsten-Oxide Bolometric Thin Films for Uncooled IR

Detectors," *Journal of the Korean Physical Society*, Vol. 45, pp. S902-S905, 2004.

[38] Y. H. Han, K. T. Kim, C. A. Nguyen, H. J. Shin, I. H. Choi, and S. Moon, "Fabrication and Characterization of Bolometric Oxide Thin Film Based on Vanadium-Tungsten Alloy," *Sensors and Actuators A 123-124*, pp. 660-664, 2005.

[39] C. A. Nguyen, H. J. Shin, K. T. Kim, Y. H. Han, and S. Moon, "Characterization of Uncooled Bolometer with Vanadium Tungsten Oxide Infrared Active Layer", *Sensors and Actuators A 123-124*, pp. 87-91, 2005.

[40] S. Moon, Y. H. Han, K. T. Kim, S. H. Lee, and H. J. Shin, "Enhanced Characteristics of $V_{0.95}W_{0.05}O_x$-based Uncooled Microbolometer," *Proceedings of IEEE Sensors*, art. no. 1597905, pp. 1137-1140, 2005.

[41] Y. H. Han, K. T. Kim, H. J. Shin, and S. Moon, "Enhanced Characteristics of an Uncooled Microbolometer Using Vanadium-Tungsten Oxide as A Thermometric Material," *Applied Physics Letters*, Vol. 86, 2005.

[42] *http://www.ajaint.com/whatis.htm*, last accessed on 24.07.2011.

[43] *http://www.umms.sav.sk/index.php?ID=415*, last accessed on 24.07.2011.

[44] B. Kebapçı, *"Development of High Performance Uncooled Infrared Detector Materials,"* Dissertation for the Degree of Master of Science, METU, 2011.

[45] *http://www.ajaint.com/PDF/SYSTEMS_ATC.pdf,* last accessed on 27.07.2011.

[46] A. Aydemir and T. Akın, "Prevention of Sidewall Redeposition of Etched Byproducts in Dry Au Etch Process," *The 22nd Micromechanics and Micro Systems Europe Workshop, (MME'11)*, Toensberk, Norway, June 19-22, 2011.

[47] S. P. Nam, H. J. Noh, S. G. Lee, and Y. H. Lee, "Electrical Properties of Vanadium Tungsten Oxide Thin Films", *Materials Research Bulletin*, Vol. 45, pp. 291-294, 2010.

[48] Y. H. Han, S. H. Lee, K. T. Kim, I. H. Chai, and S. Moon, "Properties of Electrical Conductivity of Amorphous Tungsten-Doped Vanadium Oxide for Uncooled Microbolometers," *Solid State Phenomena*, Vols. 124-126, pp. 343-346, 2007.

[49] M. Ahn, Y. H. Han, and S. Moon, "A Novel Infrared Absorbing Structure for Uncooled Infrared Detector," *Current Applied Physics*, Vol. 7, pp. 617-621, 2007.

[50] C. Venkatasubramanian, M. W. Horn, and S. Ashok, "Ion Implantation Studies on VO_x Films Prepared by Pulsed DC Reactive Sputtering," *Nuclear Instruments and Methods in Physics Research B*, Vol. 267, pp.1476-1479, 2009.

[51] G. Silversmit, D. Depla, H. Poelman, G.B. Marin, and R.D. Gryse, "Determination of the V2p XPS Binding Energies for Different Vanadium Oxidation States (V^{5+} to V^{0+})," *Journal of Electron Spectroscopy and Related Phenomena*, Vol. 135, pp. 167-175, 2004.

[52] J. Ye, L. Zhou, F. Liu, J. Qi, W. Gong, Y. Lin, and G. Ning, "Preparation, Characterization and Properties of Thermochromic Tungsten-Doped Vanadium Dioxide by Thermal Reduction and Annealing", *Journal of Alloys and Compounds*, Vol. 504, pp. 503-507, 2010.

[53] J. Shi, S. Zhou, B. You, and L. Wu, "Preparation and Thermochromic Property of Tungsten-Doped Vanadium Dioxide Particles", *Solar Energy Materials & Solar Cells*, Vol. 91, pp. 1856-1862, 2007.

[54] C. Batista, R.M. Riberio, and V. Teixeira, "Synthesis and Characterization of VO_2-Based Thermochromic Thin Films for Energy-Efficient Windows", *Nanoscale Research Letters*, Vol. 6, 2011.

APPENDIX A

AFM MEASUREMENT RESULTS

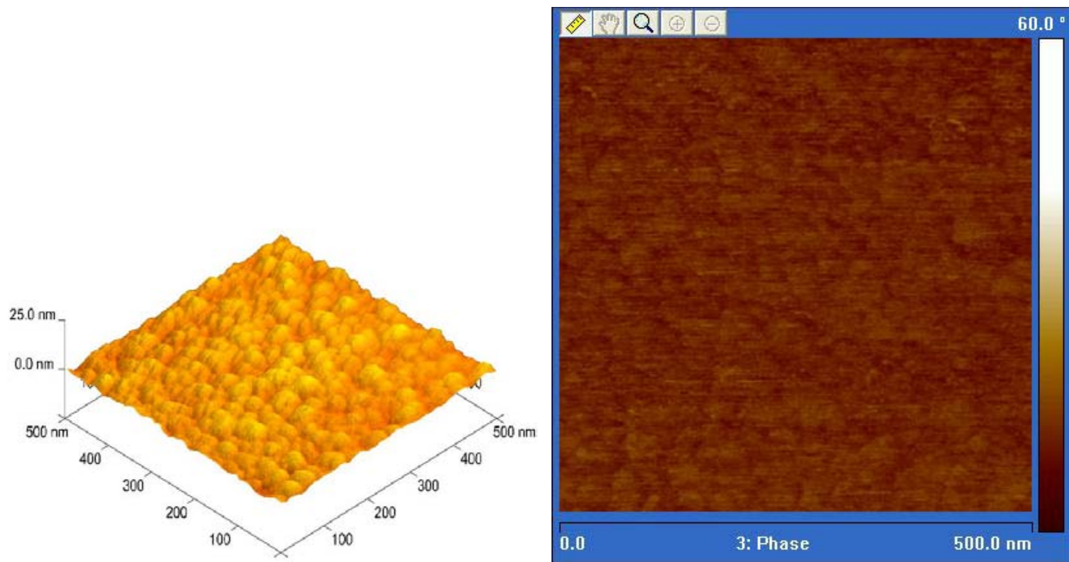

(a) (b)

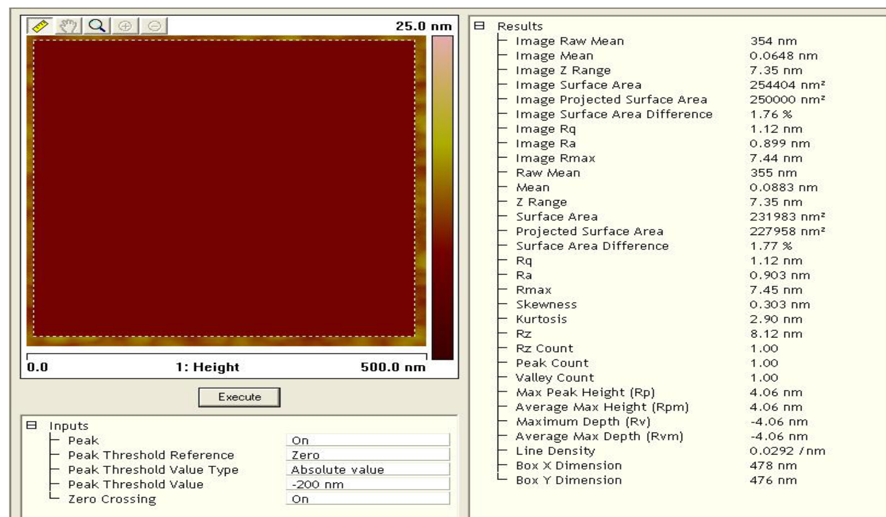

(c)

Figure A.1: AFM results of the film fabricated using the recipe of S3 (3D view (a), Phase Imaging Mode (b), and Roughness (c)).

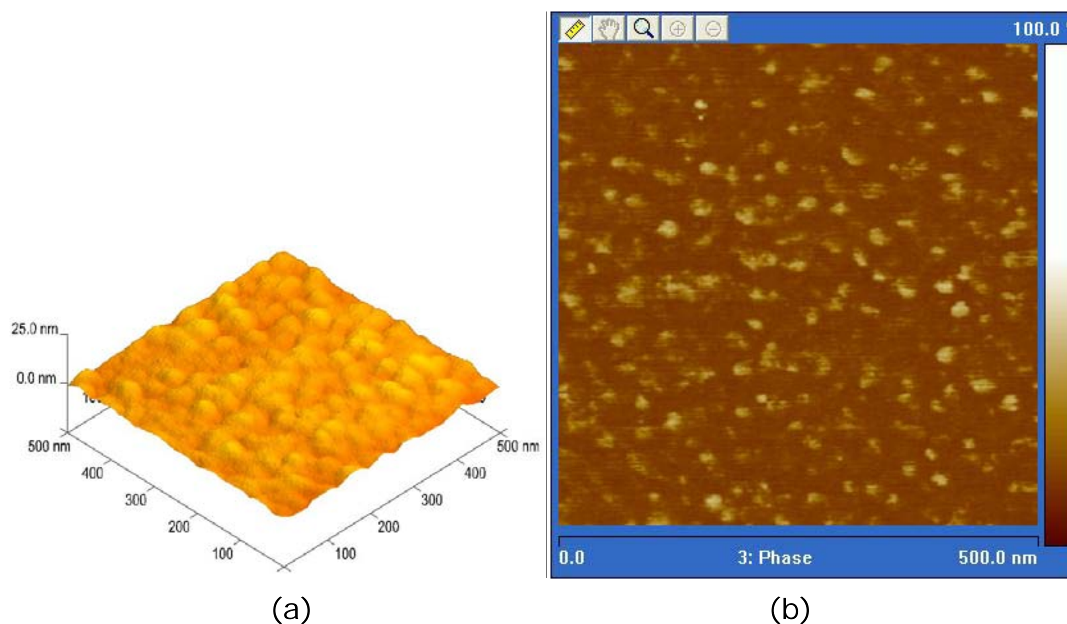

(a) (b)

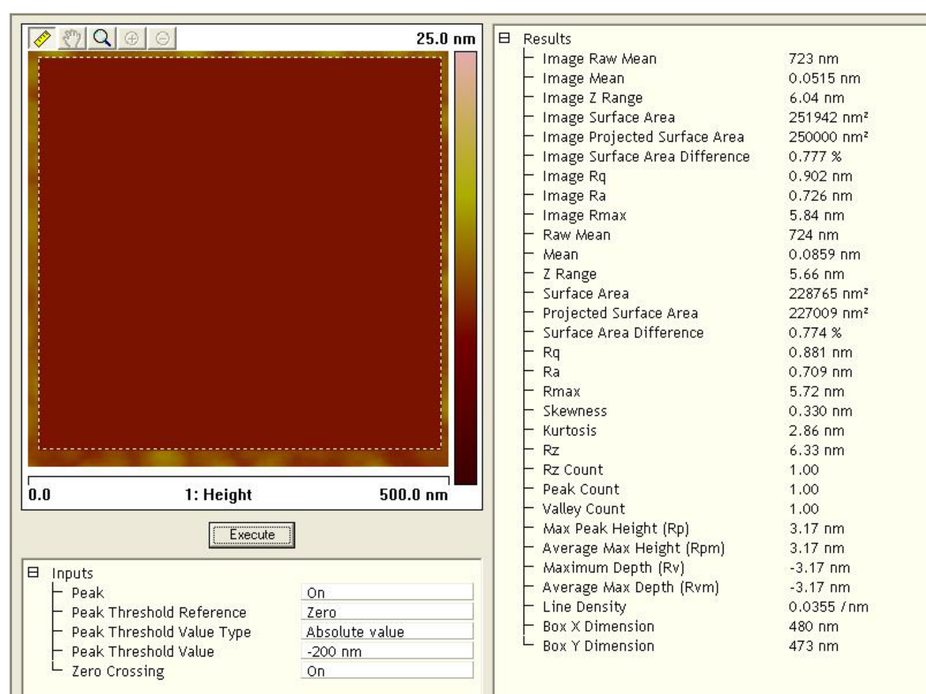

(c)

Figure A.2: AFM results of the film fabricated using the recipe of S3 and exposed to oxygen plasma for 60 minutes (3D view (a), Phase Imaging Mode (b), and Roughness (c)).

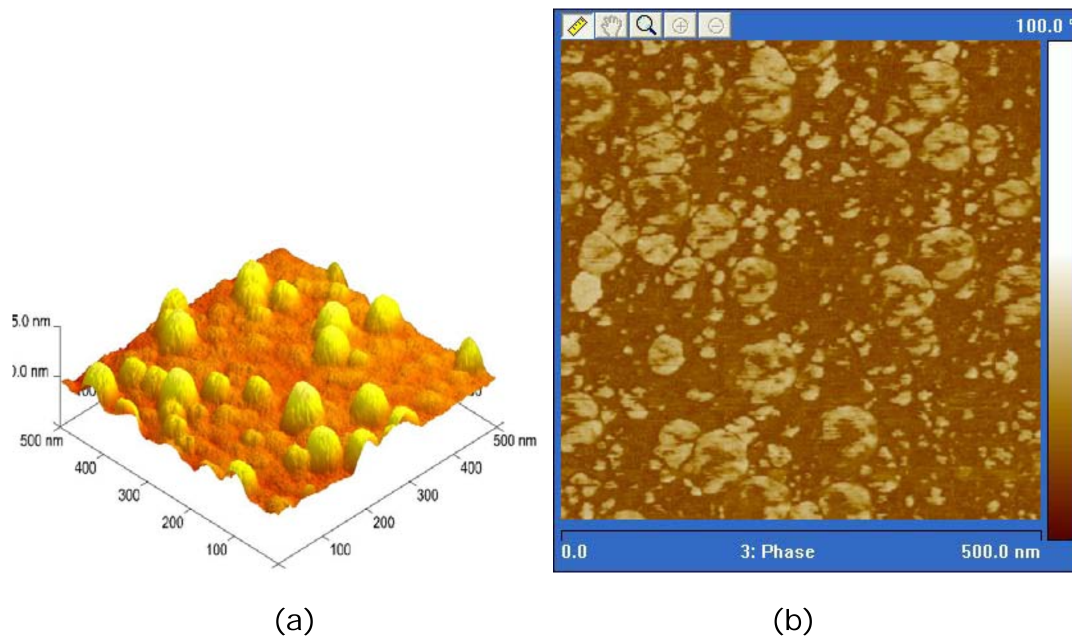

(a) (b)

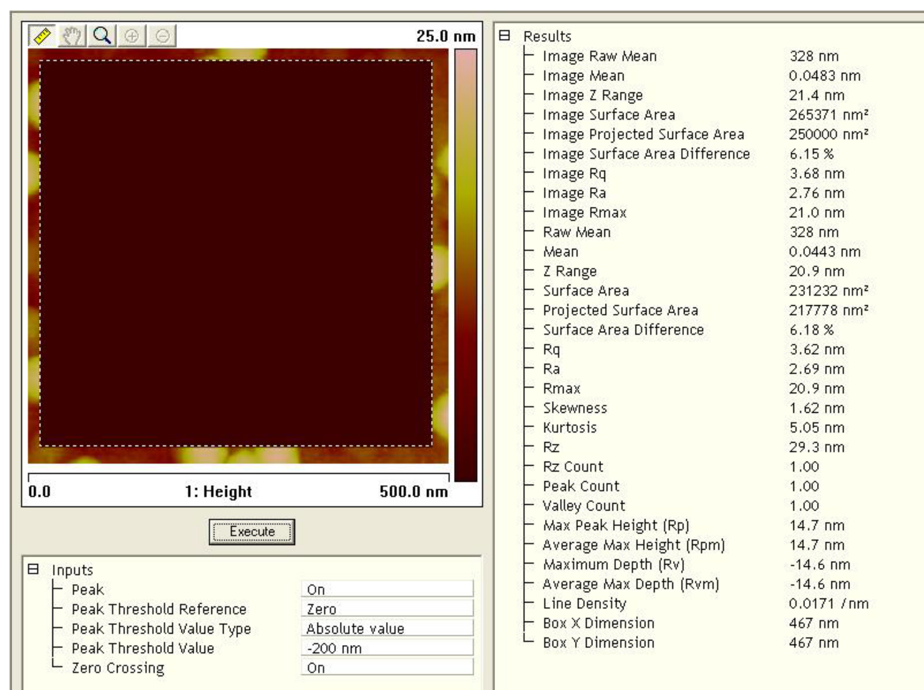

(c)

Figure A.3: AFM results of the film fabricated using the recipe of S3 and post-annealed at 300 °C for 90 minutes (3D view (a), Phase Imaging Mode (b), and Roughness (c)).

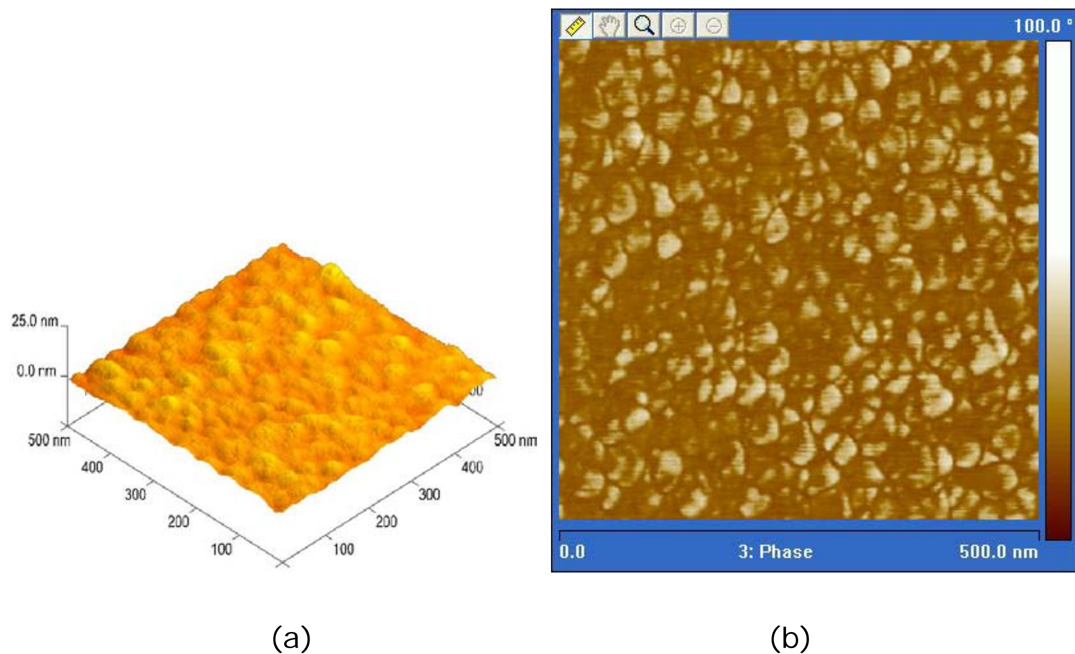

(a) (b)

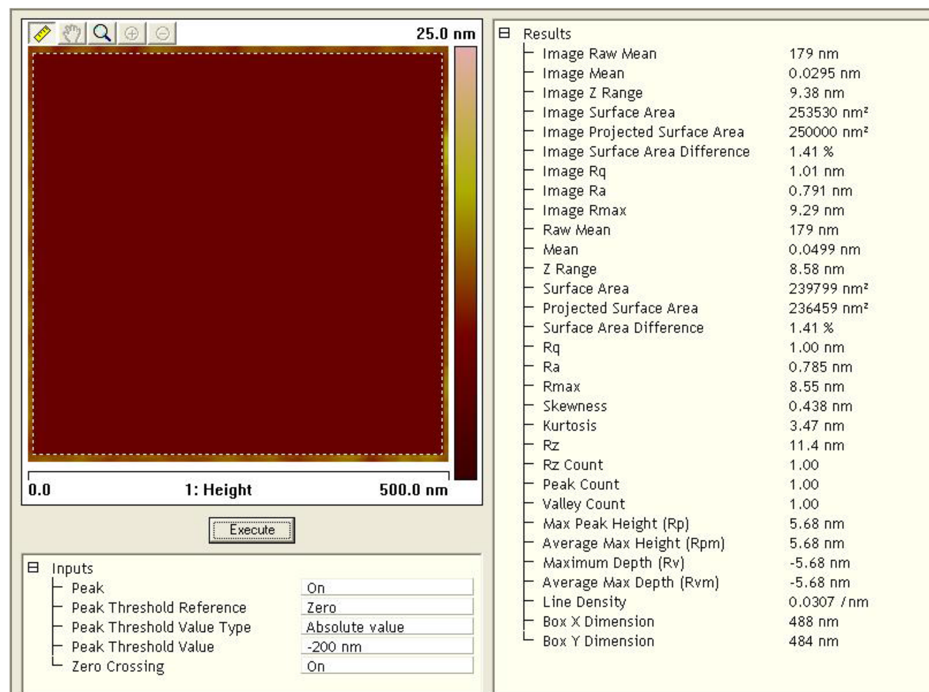

(c)

Figure A.4: AFM results of the film fabricated using the recipe of S1 (3D view (a), Phase Imaging Mode (b), and Roughness (c)).

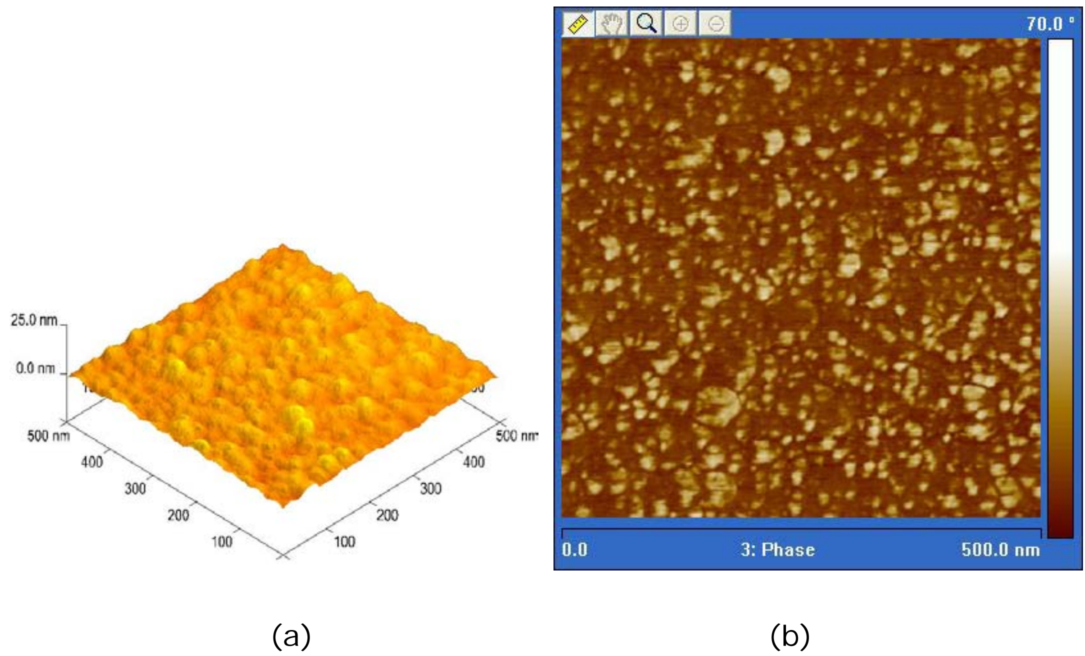

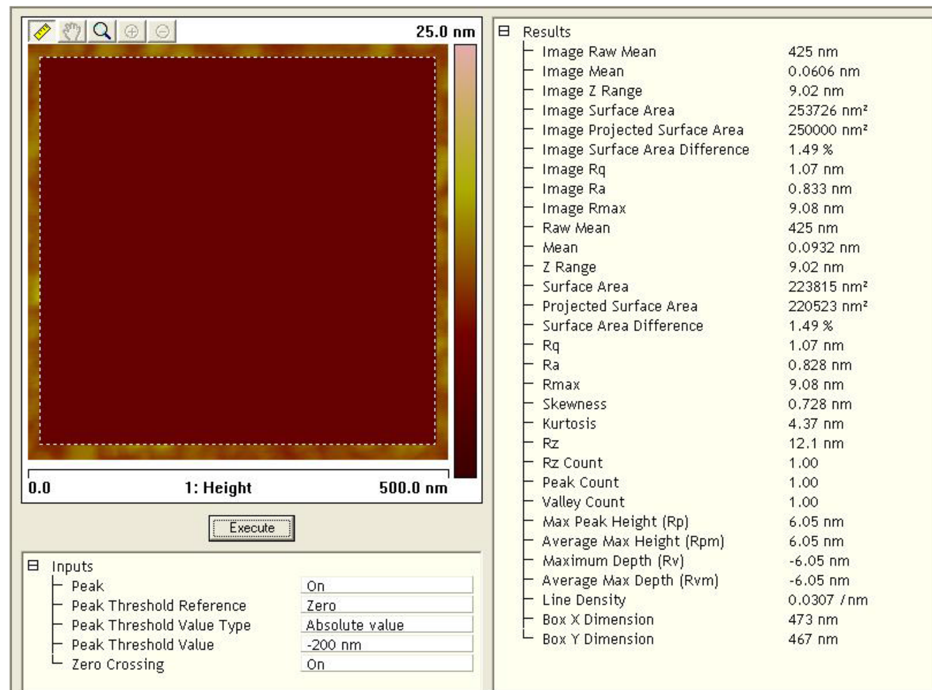

Figure A.5: AFM results of the film fabricated using the recipe of S5 (3D view (a), Phase Imaging Mode (b), and Roughness (c)).

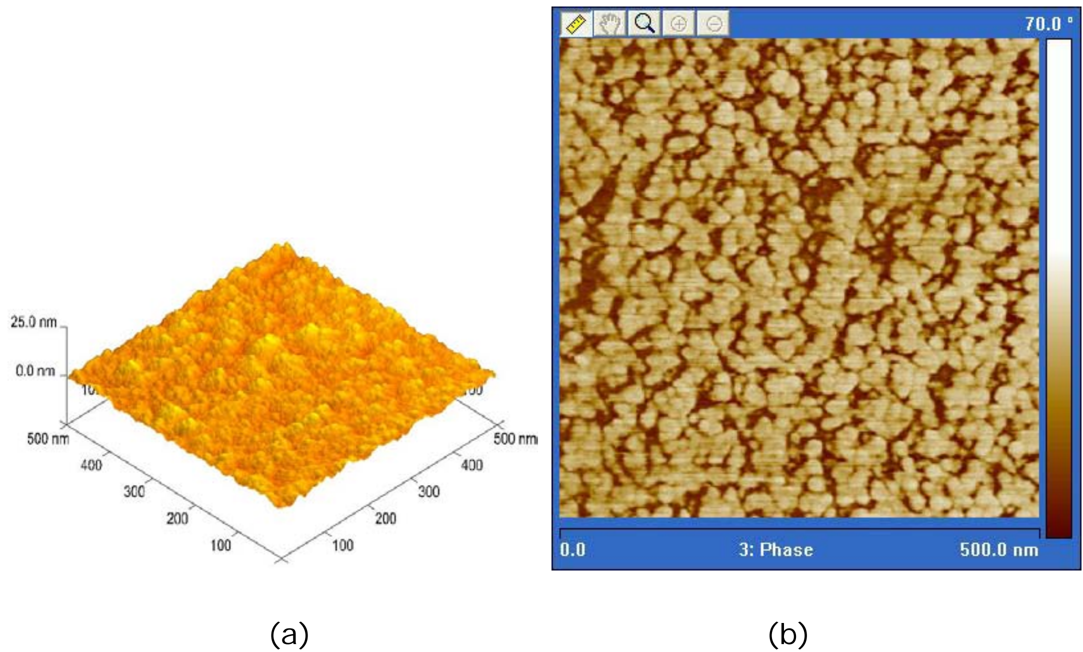

(a) (b)

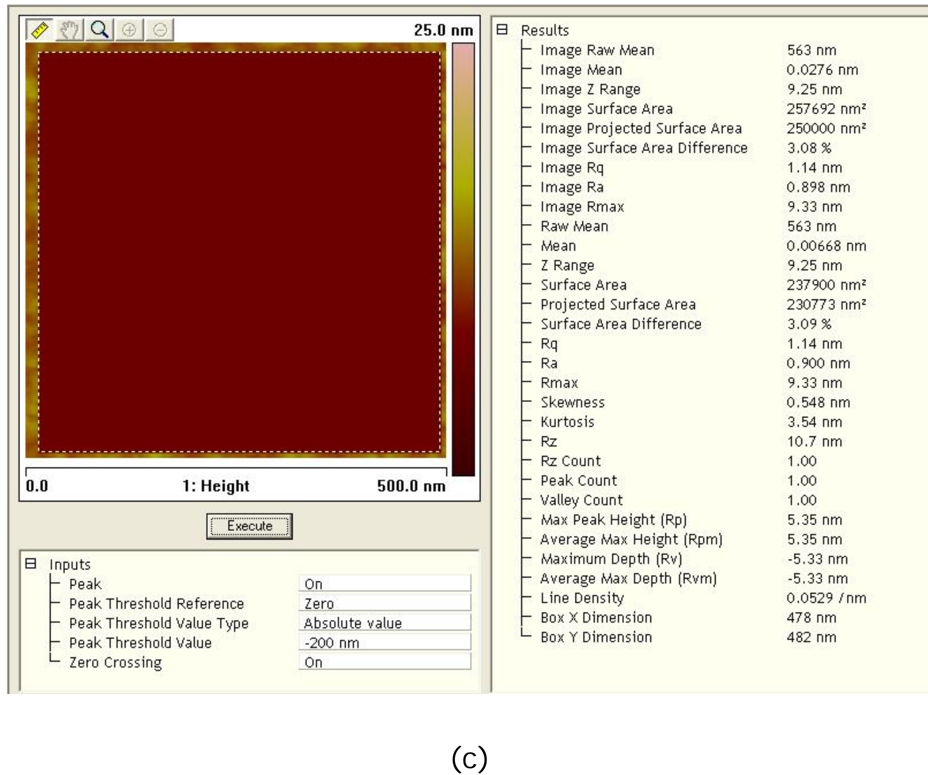

(c)

Figure A.6: AFM results of the film fabricated using the recipe of S10 (3D view (a), Phase Imaging Mode (b), and Roughness (c)).

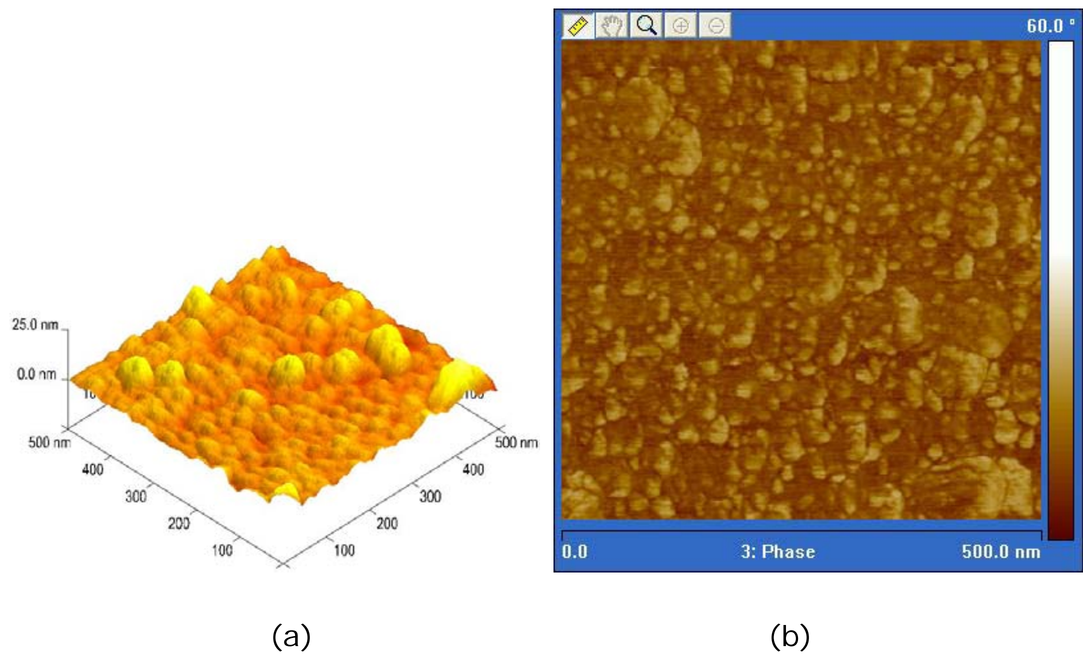

(a) (b)

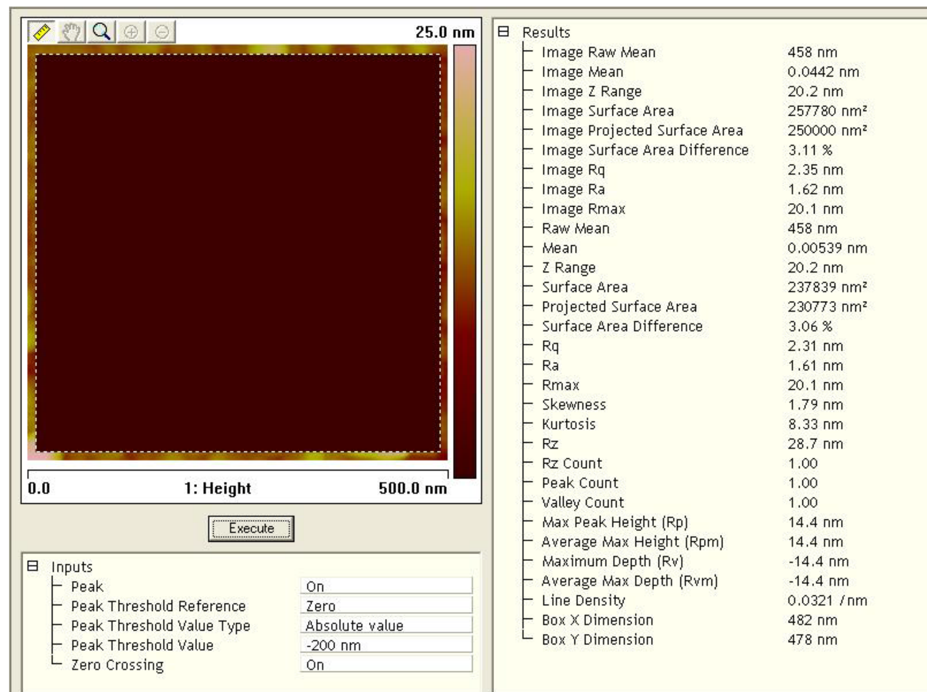

(c)

Figure A.7: AFM results of the film fabricated using the recipe of S18 (3D view (a), Phase Imaging Mode (b), and Roughness (c)).

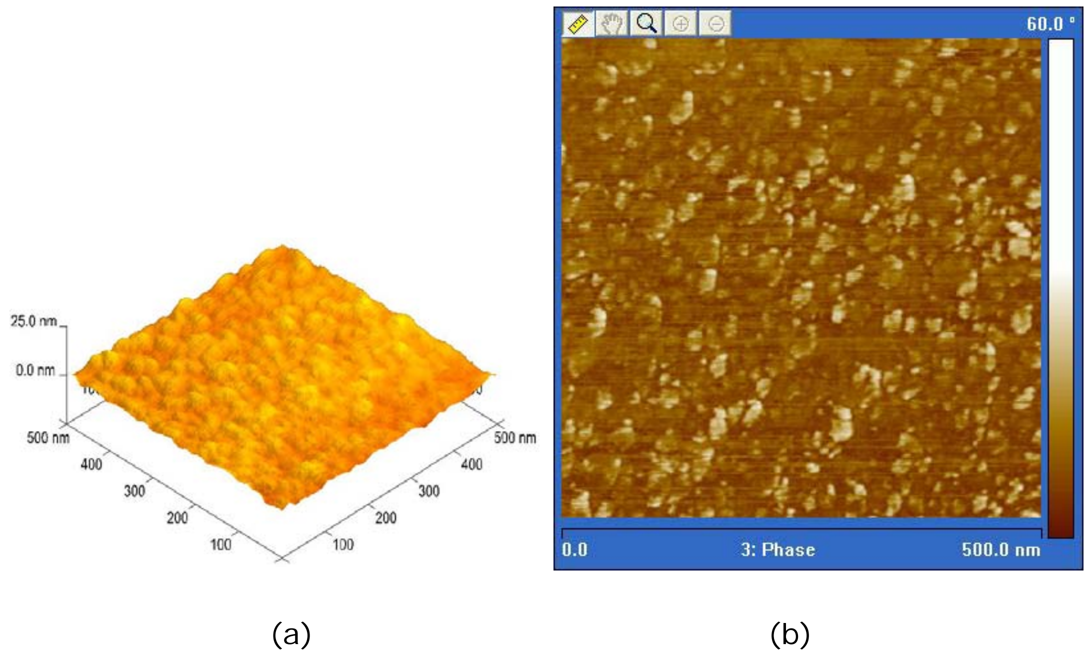

(a) (b)

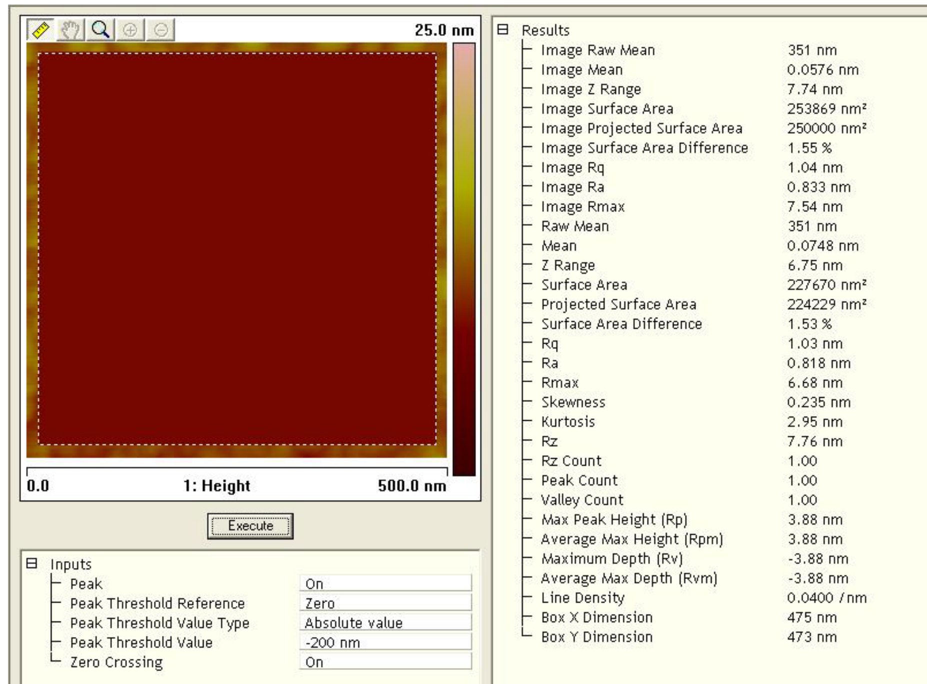

(c)

Figure A.8: AFM results of the film fabricated using the recipe of S13 (3D view (a), Phase Imaging Mode (b), and Roughness (c)).

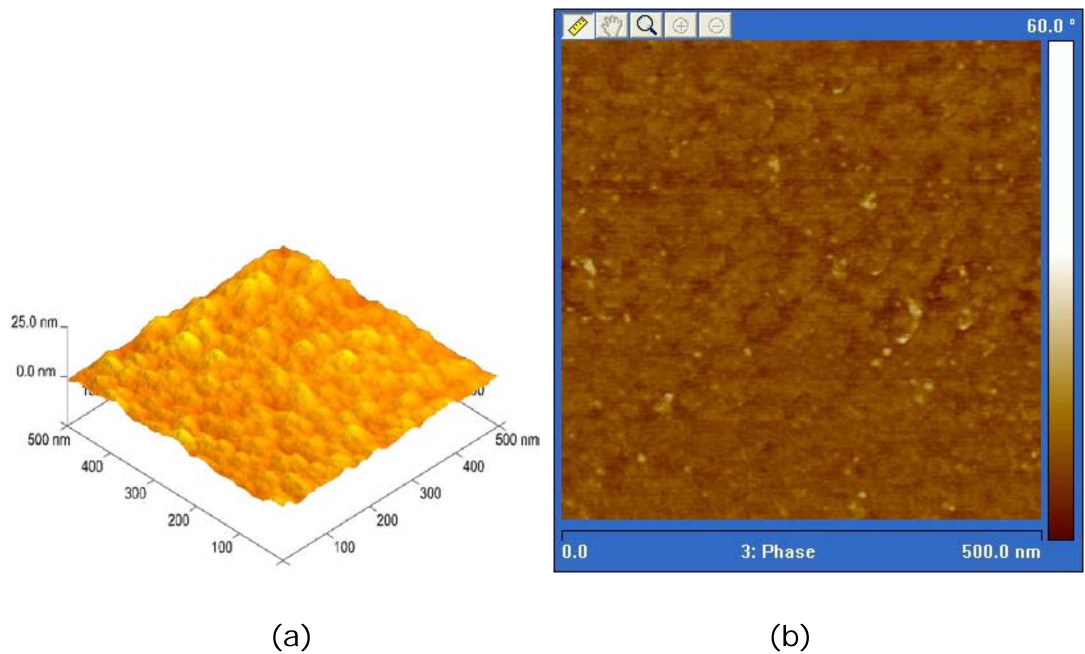

(a) (b)

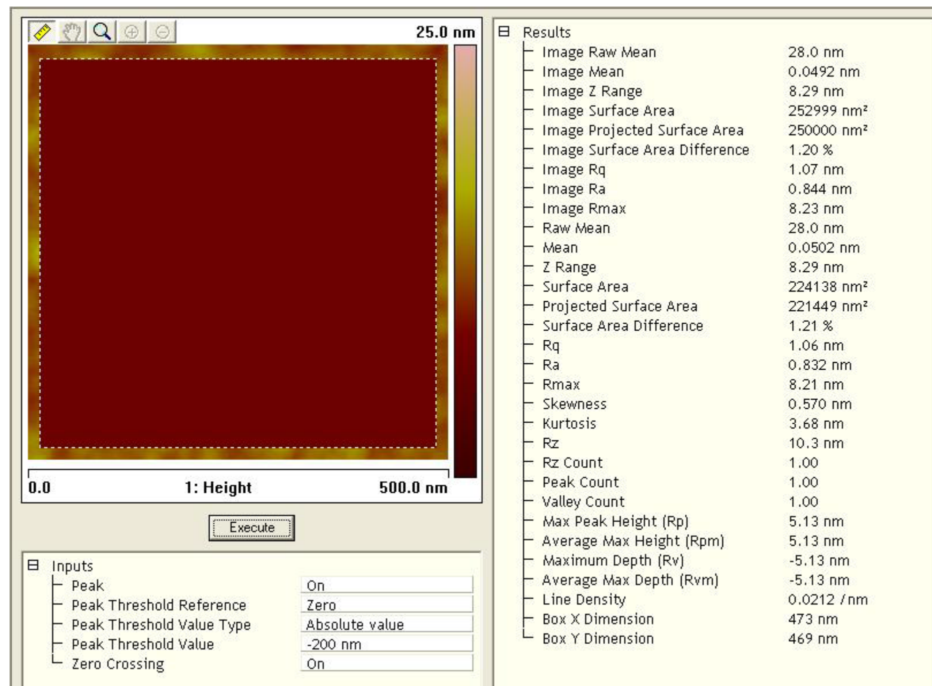

(c)

Figure A.9: AFM results of the film fabricated using the recipe of S12 (3D view (a), Phase Imaging Mode (b), and Roughness (c)).